

August 2020

Computational Materials Science and Engineering: Model Development and Case Study

Yihan Xu
University of Wisconsin-Milwaukee

Follow this and additional works at: <https://dc.uwm.edu/etd>



Part of the [Chemistry Commons](#), and the [Materials Science and Engineering Commons](#)

Recommended Citation

Xu, Yihan, "Computational Materials Science and Engineering: Model Development and Case Study" (2020). *Theses and Dissertations*. 2630.
<https://dc.uwm.edu/etd/2630>

This Dissertation is brought to you for free and open access by UWM Digital Commons. It has been accepted for inclusion in Theses and Dissertations by an authorized administrator of UWM Digital Commons. For more information, please contact open-access@uwm.edu.

COMPUTATIONAL MATERIALS SCIENCE AND ENGINEERING: MODEL DEVELOPMENT AND CASE STUDY

by
Yihan Xu

A Dissertation Submitted in
Partial Fulfillment of the
Requirements for the Degree of

Doctor of Philosophy
in Engineering

at
The University of Wisconsin–Milwaukee
August 2020

ABSTRACT

COMPUTATIONAL MATERIALS SCIENCE AND ENGINEERING: MODEL DEVELOPMENT AND CASE STUDY

by
Yihan Xu

The University of Wisconsin–Milwaukee, 2020
Under the Supervision of Prof. Nidal Abu-Zahra and Prof. Deyang Qu

This study presents three tailored models for popular problems in energy storage and biological materials which demonstrate the application of computational materials science in material system development in these fields. The modeling methods can be extended for solving similar practical problems and applications.

In the first application, the thermo-mechanical stress concentrated region in planar sodium sulfur (NaS) cells with large diameter and different container materials has been estimated as well as the shear and normal stresses in these regions have been quantified using finite-element analysis (FEA) computation technique. It is demonstrated that the primary failure mechanism in the planar NaS system design considered in the current work would be the interfacial fracture between the insulating header (IH) and the upper insert metal (IM1) due to the normal stress in cell height direction, and the necessary treatments, including better material selection or improved bonding technology between IH and IM1, must be involved to avoid the fractures of constituent components in the joint area.

In the second application, a full atomistic molecular dynamics (MD) computation approach has been employed to quantify the Flory-Huggins parameters between poly(lactic acid) (PLA), poly(glycolic acid) (PGA), and tetracycline-HCl (TC-HCl) drugs, which can elucidate the thermodynamic stability and the interaction between drugs and poly(lactic/glycolic acid) (PLGA) carriers polymers. Thermodynamic analysis regarding

the miscibility and the stability of PLA, PGA, TC-HCl phases are then conducted in line with the experimental fabrication of polymer-drug films of two different copolymer ratio products, *i.e.*, 50/50 (PLA/PGA ratio) and 75/25 PLGA samples. Meso-scale computations using phase-field method (PFM) are also conducted to predict the structural evolution of PLGA/TC-HCl systems using the calculated Flory-Huggins parameters. The results show that the surface morphology of PLGA/TC-HCl film can be highly dependent upon the thermodynamic interaction between the polymer and drug phases.

In the third application, full atomistic MD simulations have been performed on tetra-sulfides and undoped conjugated polymers pernigraniline base polyaniline (PNB), leucoemeraldine base polyaniline (LEB), poly(3,4-ethylenedioxythiophene) (PEDOT) and polypyrrole (PPY) to investigate the binding effectiveness between polysulfides and polymer binders. The weight ratio between sulfur and binder in lithium-sulfur cells is considered in 1:1 v/v mixture of dioxolane/dimethoxyethane. The simulations reveal that the end group 2 of PNB can effectively bind a lithium tetra-sulfide (*i.e.* Li_2S_4) cluster or 2 out of 43 Li_2S_4 molecules with the effect of solvent. However, repeat units of PNB, LEB, PEDOT and PPY seem ineffective in binding solvated Li_2S_4 through non-bonded interaction, especially when the concentration of tetra-sulfide/binder in a local domain of the cathode is low. Therefore, polymers with this specific functional group (*i.e.* the end group 2 of PNB) are suggested to be further studied as potential effective binders to inhibit the shuttle effect of solvated lithium polysulfides. Also, since the solvent has considerable impact on the binding effectiveness between tetra-sulfides and binder, it is suggested to take advantage of the explicit solvation models, such as those built in this work, to predict how other influencing factors affect binding between polysulfides and polymers.

© Copyright by Yihan Xu, 2020
All Rights Reserved

To my parents, my husband, my parents-in-law and my friends from UWM

TABLE OF CONTENTS

List of Figures	viii
List of Tables	xiv
1 Introduction	1
1.1 Computational materials science	1
1.2 Scope of the present study	3
2 Container materials of modern planar sodium sulfur (NaS) cells	4
2.1 Introduction	4
2.2 Computational method	7
2.2.1 Digital construction of prototype planar NaS cells	7
2.2.2 Cell container material types	8
2.2.3 Computational conditions	11
2.3 Results and discussion	11
2.3.1 Insulating header (IH) outer surface	15
2.3.2 Interface between insulating header (IH) and insert metals (IMs)	18
2.3.3 alumina solid electrolyte (BASE) surfaces	22
2.4 Conclusions	27
3 PLGA-based drug carriers	29
3.1 Introduction	29
3.2 Methodology	31
3.2.1 Computational section	31
3.2.2 Experimental section	36
3.3 Results and discussion	37
3.3.1 MD computation	37
3.3.2 Experimental film surface characterization	45
3.3.3 Free energy density calculation and meso-scale simulation	47
3.4 Conclusions	52

4	Polymeric binders: a case for Li–S batteries	53
4.1	Introduction	53
4.1.1	General introduction to Li–S batteries	53
4.1.2	Working mechanism and cathode issues of Li–S batteries	55
4.1.3	Polymeric binders: properties, structures and influence on the battery performance	58
4.1.4	Binding energy between binder and dissolved polysulfides	60
4.2	Full-atomistic MD simulation	65
4.2.1	Model species and the relevant partial atomic charges	65
4.2.2	Establishing MD box	66
4.2.3	MD simulation	67
4.2.4	Calculation of interaction energy	70
4.3	Results and discussion	71
4.3.1	Single polymer chain and single lithium tetra-sulfide in vacuum	71
4.3.2	Single polymer chain and single lithium tetra-sulfide in solvent	73
4.3.3	Polymer binders and lithium tetra-sulfides (1:5 w/w poly-mer/tetra-sulfide) in vacuum	73
4.3.4	Polymer binders and lithium tetra-sulfides (1:5 w/w poly-mer/tetra-sulfide) in solvent	74
4.4	Conclusions	76
5	Conclusion	94
	Bibliography	97
	Curriculum Vitae	122

LIST OF FIGURES

2.1	Representative NaS cell shapes of (a) tubular and (b) planar designs.	6
2.2	(a) Cross-sectional structure of a prototype planar NaS cell, and (b) CTE and (c) elastic modulus variations with temperatures for cell container and α -, β/β' -alumina materials.	9
2.3	(a) Deformation behaviors (shapes) and von-Mises stress distributions (color contour) of cells with various cell container materials after freeze (520 \rightarrow 20 $^{\circ}$ C) and thaw (20 \rightarrow 350 $^{\circ}$ C), and (b) schematic to show the cell contraction aspect upon cooling. In Figure 2.3(a), the deformation amounts are magnified by 10 times for visual clarification.	13
2.4	Stress-strain curves at various temperatures for (a) Al3003, (b) STS304, (c) STS430, and (d) KOVAR materials.	14
2.5	Cropped images from Figure 2.3(a) to show the deformation behaviors (shapes) and the von-Mises stress distributions (in [MPa], color contour) of cells with various cell container materials after freeze (520 \rightarrow 20 $^{\circ}$ C) and thaw (20 \rightarrow 350 $^{\circ}$ C) in the cell joint areas. The deformation amounts are magnified by 10 times for visual clarification.	15
2.6	Height normal stress (σ_{33}) distributions on the outer surface of IH with cell temperature changes for four prototype planar NaS cells.	17

2.7	(a) Radial shear stress (σ_{13}) and (b) height normal stress (σ_{33}) distributions on the top surface of IH with cell temperature changes for four prototype planar NaS cells.	20
2.8	Contour maps of (a) radial shear σ_{13} and (b) height normal σ_{33} distributions on IH surfaces with changing temperatures along the interfaces of IH/IM2 for the STS304 cell. The black dotted lines in each map indicate the edge positions of IM2 in direct contact with IH bottom surface.	21
2.9	(a) Radial shear stress (σ_{13}) and (b) height normal stress (σ_{33}) distributions on the bottom surface of IM1 with cell temperature changes for four prototype planar NaS cells.	23
2.10	Radial normal stress (σ_{11}) distributions on the top surface of BASE with cell temperature changes for four prototype planar NaS cells.	24
2.11	Radial normal stress (σ_{11}) distributions on the bottom surface of BASE with cell temperature changes for the prototype planar NaS cells with various cell container materials. The black dotted line in each map indicates the edge position of GS in direct contact with BASE bottom surface.	25
2.12	Summary of predicted maximum local stress concentrations at various cell components for the four prototype planar NaS cells.	26
3.1	(a) Structures of PLA and PGA chains and TC molecules, and (b) examples of MD boxes to contain PLA/PGA, PLA/TC, and PGA/TC blends.	34
3.2	Plots to show the calculated χ values in the blend systems of (a) PLA/PGA and (b) PLA/TC and PGA/TC. In Figure 3.2(b), numerical suffixes indicate the weight % of TC in the blend.	41
3.3	Plots to show the calculated RDF values of (a) intramolecular carbon atoms, (b) first peaks of intramolecular carbon atoms, and (c) intermolecular carbon atoms of PLA in pure PLA and PLA/PGA blend systems.	42

3.4	Plots to show the calculated RDF values of (a) intramolecular carbon atoms, (b) first peaks of intramolecular carbon atoms, and (c) intermolecular carbon atoms of PGA in pure PGA and PLA/PGA blend systems.	43
3.5	Plots to show the calculated RDF values of (a) intramolecular carbon atoms and (b) intermolecular carbon atoms of polymers in the TC/polymer blend systems.	45
3.6	Plot of self-diffusivities (D_{self}) of TC in PLA/TC and PGA/TC systems. . .	46
3.7	Examples of AFM scans from (a) PLGA50/50-TC and (b) PLGA75/25-TC films, and drug size distributions from (c) PLGA50/50-TC and (d) PLGA75/25-TC films.	47
3.8	Plot of free energy densities using the Flory-Huggins solution model for PLA/TC and PGA/TC systems.	49
3.9	Microstructural evolution predicted using phase-field method for (a) PLGA50/50-TC and (b) PLGA75/25-TC systems. φ_s represents the solvent volume fraction. 51	51
4.1	Schematic of a conventional Li-S battery and its cathode composition. . . .	56
4.2	Products and intermediates of electrochemical reactions of sulfur species in cathode.	57
4.3	RESP charges of species.	78
4.3	RESP charges of species (cont.).	79
4.3	RESP charges of species (cont.).	80
4.3	RESP charges of species (cont.).	81

4.4	Flow diagram of MD simulations and examples of structures of (a) randomly packed PPY, Li^+ and S_4^{2-} , (b) assembled PPY, Li^+ and S_4^{2-} , (c) assembly of PPY, Li^+ and S_4^{2-} surrounded by the DOL/DME solvent mixture, (d) detached Li_2S_4 and PPY in the DOL/DME solvent mixture after running MD simulations. For clarity, the structures of PPY, Li^+ and S_4^{2-} are drawn by ball and stick, while the structures of solvent molecules are represented by fine lines and only some of them are shown. The H, Li, C, N, O and S atoms are colored by white, pink, cyan, blue, red and yellow, respectively.	82
4.5	Flow diagram of MD simulations and examples of structures of (a) randomly packed PPY, Li^+ and S_4^{2-} , (b) assembled PPY, Li^+ and S_4^{2-} , (c) assembly of PPY, Li^+ and S_4^{2-} surrounded by the DOL/DME solvent mixture, (d) assembly of Li_2S_4 cluster and slightly bended PPY chain in the DOL/DME solvent mixture after running MD simulations. The color scheme of atoms and the drawing method of molecular structures are the same as that in Figure 4.4.	83
4.6	(a)-(h) Structure, (i) polymer- S_4^{2-} interaction energy, and (j) polymer- Li_2S_4 interaction energy of the self-assembled single S_4^{2-} dianion, Li^+ ions and single polymer chain. The color scheme of atoms is the same as that in Figure 4.4. Columns with heights equal to the value of the interaction energy components are stacked up, where the summation is the total interaction energy corresponding to each polymer system.	84
4.7	Structure of LEB and Li_2S_4 with the strongest Li_2S_4 -LEB interaction. The color scheme of atoms is the same as that in Figure 4.4.	85

4.8	Energy decomposition for systems of self-assembled single S_4^{2-} dianion, Li^+ ions and single polymer chain. The atoms are colored by BWR method according to their contributions to each component of Li_2S_4 -polymer interaction energy, where bluer atoms have more negative contribution (<i>i.e.</i> more contribution to attraction), redder atoms have more positive contribution (<i>i.e.</i> more contribution to repulsion), and whiter atoms have less contribution. The color scales of electrostatic, exchange repulsion and dispersion interactions are noted in each subfigure and the unit is $kJ\ mol^{-1}$. The exchange repulsion is noted as “Repulsion” in subfigures (e)-(h).	86
4.9	Total interaction energy and distance of (a) Li_2S_4 -PNB, (b) Li_2S_4 -LEB, (c) Li_2S_4 -PEDOT, and (d) Li_2S_4 -PPY with the effect of the solvent mixture over time.	87
4.10	Detached polymer binder and Li_2S_4 with the effect of the solvent mixture. For clarity, the solvent mixture is drawn as the blue background using QuickSurf method provided in VMD.	88
4.10	Detached polymer binder and Li_2S_4 with the effect of the solvent (cont.). For clarity, the solvent mixture is drawn as the blue background using QuickSurf method provided in VMD.	89
4.11	(a)-(h) Structure, (i) polymer- S_4^{2-} interaction energy, and (j) polymer- Li_2S_4 interaction energy of the self-assembled multiple S_4^{2-} , Li^+ and single polymer chain. The color scheme of atoms is the same as that in Figure 4.4. Columns with heights equal to the value of the interaction energy components are stacked up, where the summation is the total interaction energy corresponding to each polymer.	90

4.12	Structure of (a) PNB, (b) LEB, (c) PEDOT, and (d) PPY and cluster of Li_2S_4 with the effect of the solvent mixture after running the MD of 50 ns. For clarity, the solvent mixture is drawn as the blue background using QuickSurf method provided in VMD. (e)-(h) Interaction energies of polymer- Li_2S_4 over the last 30 ns of the MD simulations.	91
4.13	Representative simulation snapshot of PPY and randomly distributed Li_2S_4 clusters in the DOL/DME solvent mixture. Solvents are not shown. The color scheme of atoms is the same as that in Figure 4.4.	92
4.14	Numbers of Li_2S_4 within 5 Å of binders at different time points during the last 20 ns of the MD simulations.	93

LIST OF TABLES

2.1	Constituent material types of planar NaS cells used in this work.	10
2.2	Thermo-mechanical properties of the cell materials in the temperature range of 20~520 °C.	10
2.3	Critical crack lengths (a_c) on the outer surface of IH in the prototype planar cells with different container materials.	18
3.1	PLA/PGA blend systems with various composition ratios considered in the present MD simulations.	33
3.2	PLA/PGA blend systems with various composition ratios considered in the present MD simulations.	33
3.3	Solubility parameter (δ) values of PLA, PGA, and TC predicted by simulation at 298.15 K.	38
3.4	Solubility parameter (δ) values of PLA and PGA estimated using different experimental and theoretical approaches at 298.15 K.	38
3.5	χ values of PLA/PGA blend systems with various composition ratios considered in the present MD simulations.	40
3.6	χ values of PLA/TC and PGA/TC blend systems considered in the present MD simulations. The unit of CED is J cm ⁻³	44
4.1	Comparison of specific energy and energy density between Li-S and Li-ion batteries.	54

ACKNOWLEDGEMENTS

In a first place I would like to express my deep appreciation and gratitude to my advisor, Professor Nidal Abu-Zahra and co-advisor, Professor Deyang Qu for their brilliant advice and millions of hours spent on discussing and correcting my research, dissertation and oral defense, which makes me feel reassured every time as well as drives my passion for scientific research.

Also, I would like to express my sincere thanks to Professor Junjie Niu, Professor Benjamin Church and Professor Jorg Woehl for serving on my doctoral committee with their kind guidance, thought-provoking suggestions, as well as valuable feedback and advice.

I would like to give special thanks to Dr. Dong Zheng, research associate working in Dr. Deyang Qu's group for always being next to me, transferring his electrochemical knowledge to me and sharing brilliant ideas with me for my research and dissertation.

And I definitely appreciate my fellow colleagues in Dr. Qu's research group for their kind, warm and helpful concern, which gives me a feeling like we are part of a family and has been encouraging me a lot. I would like to thank Phani Ravi Teja Nunna, my fellow colleague in Dr. Abu-Zahra's group, for lending me a hand with editing my research publication. It was also a great pleasure to work with Dr. Chang-Soo Kim. Dr. Kim has cultivated my perseverance in scientific research. I would also like to thank Betty Warras - Sr. Admin. Specialist at UWM for her assistance regarding my PhD program of study.

Thanks to the powerful computational resources providing by UWM High Performance Computing (HPC) Service, I could implement computations for my research smoothly. I am also very grateful to Jason Bacon and Shawn A Kwang for HPC cluster related support, as well as James F Wagner for providing ABAQUS related support.

Supports through the UWM Chancellor's award, the College of Engineering and Applied Science (CEAS) Dean's Fellowship, Distinguished Graduate Student Fellowship as

well as Distinguished Dissertation Fellowship are also acknowledged.

Chapter 1

Introduction

1.1 Computational materials science

Motivated by demands in engineering or interest in science, we've always been looking for new and better materials: easier to process, more durable, lower-cost, stronger and lighter-weight, and with less impact on the environment. Material design has been guided by experiments and experience for centuries until the finite element method (FEM) was combined with computer. After that, descriptions of material properties became possible by computational methods and this has generated great impact on research and development in academia and industry. Especially, the simulations of mechanical properties such as load-stress relation, stability of the composite material belonged to the most advanced technologies in design of tools, buildings and vehicles.

With the continuous development of new functional materials, such as semiconductor, energy storage materials, biological materials, advanced membrane materials, conductive polymers, etc., these materials no longer just take advantage of mechanical properties. Moreover, in the past few decades, the development of nanotechnology has been propelling the research and development of nanomaterials, such as the widely known graphene. Controlling structures and properties of materials at the atomic scale has been the frontier of materi-

als science and engineering. Following this trend, modern computational materials science gradually focuses on atomic scale modeling over the past decades.

Modern computational materials science is interdisciplinary. It is fueled by chemistry, mathematics, biology and physics. In return, it can help with the development of functional materials to meet requirements of all kinds of areas. In computational biology, massive atomistic computer simulations are now possible to compute a system with millions of atoms on the nanosecond time scale [1]. Statistical physical methods [2], such as molecular dynamics (MD) provide the basis for computation of processes, such as diffusion, adsorption and crystal growth. Theoretical chemistry uses various theoretical physics methods, especially quantum mechanics, to explain and predict the nature of chemical phenomena. It contributes greatly to modern computational materials science by its highly accurate computations of molecule geometries, energy, electronic band structure, gap, transition state of chemical reactions and spectral data (Infrared, Raman, VCD and ROA for examples). If the property of interest is an atomic one, then theoretical chemistry is just the method to study it.

Developments of density functional theory (DFT) [3, 4] and multiscale models [5] have been seen as the most influential to computational materials science [6]. Both methods have been awarded the Nobel Prize in chemistry, but their impact extends beyond and affects all disciplines of basic natural science. Among quantum chemistry methods, DFT calculation method doesn't provide the highest accuracy but it is highly practical: balanced between accuracy and computation speed. The multiscale model figured out another way to achieve the balance. In multiscale simulations, a local area of interest is processed by a method of high-level precision. This area is embedded into a larger one, which is processed at a lower level, and more shells can be added if needed. Therefore, the results stay meaningful while the precision is still sufficient. But how to deal with the interfaces between shells is a challenge.

With the computational resources getting more economical and powerful as well as computational approaches getting more accurate, computational materials science will be more

practical in prediction of advanced functional materials before attempting synthesis and assembly.

1.2 Scope of the present study

With the improving computational resources and computational approaches, computational materials science will be increasingly applied to predict material structures, properties and performance. One of the challenges is how to properly build models using the available resources and approaches. In the present study, we tailored models for three popular issues:

- We have built a FEM model to study impacts of container materials on the thermo-mechanical residual stress accumulation of modern planar sodium sulfur (NaS) cells (see Chapter 2).
- Also, we have built a MD model to investigate the polymer-drug interactions and their impact on the structural evolutions in PLGA-tetracycline films (see Chapter 3).
- And MD method has been applied to study the binding effect between binders and polysulfide species in Li-S batteries (see Chapter 4).

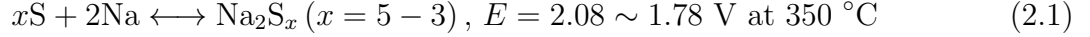
Details are provided in Chapters 2, 3 and 4, respectively.

Chapter 2

Container materials of modern planar sodium sulfur (NaS) cells

2.1 Introduction

Sodium (Na) β/β'' -alumina batteries (NBBs) have become increasingly recognized as one of the most promising contenders for large-scale energy storage systems (ESSs) due to their high theoretical specific energy, high energy efficiency, low cost of raw materials, and long lifespan [7, 8, 9, 10, 11, 12, 13, 14, 15, 16, 17]. The NBB system consists of a molten sodium anode, a β/β'' -alumina solid electrolyte (BASE), and a cathode compartment. Depending on cathode chemistries, NBBs can be typically classified into two types, *i.e.*, NaS and Na metal halide (Na/NiCl₂ or Na/FeCl₂) cells. Because the active anode Na materials must be maintained in their molten state, the operating temperatures of these NBBs are relatively high (e.g., 300-350 °C for NaS and 270-300 °C for Na metal halide chemistries, respectively). Out of these two types of NBBs, the NaS cells utilize molten S as the cathode materials that endow high theoretical specific energy (760 Wh kg⁻¹), high theoretical energy density (2584 Wh l⁻¹), and very high theoretical specific capacity (1675 Ah kg⁻¹) [11]. The cell reaction occurs in an NaS system is given by [18],



Contemporarily, this NaS cell technology is available for grid-scale applications. NGK (NGK Insulators, Ltd.) has delivered NaS battery systems at approximately 200 sites worldwide, accounting for a total output of 530 MW and a storage capacity of 3700 MWh since its commercialization in 2003 [19]. In addition to the successful product-realization of NGK, other efforts to develop advanced NaS cell systems have been continuously made in recent years [20, 21, 22, 23, 24, 25, 26, 27].

For commercial deployment of practical NBBs, two cell shapes (*i.e.*, tubular and planar cells) have been commonly applied. Representative NaS cell geometries of the two shapes are provided in Figure 2.1 (fabricated by RIST, South Korea). The distinct advantages of the planar cell design over the tubular one may include the easiness for stacking, direct inter-cell connection without any external connectors, lower manufacturing cost, elimination of the orientation and gravity effects, larger active area of BASE per unit weight of the cell, possibility of applying a thinner solid electrolyte with higher ionic conductivity, easiness for post-analysis for cell components, and so forth [11, 28]. Moreover, it was found that the electrochemical performance from a planar NaS cell is more stable than that from a tubular cell [29]. With this, relatively small planar NBBs with a typical BASE disk diameter in the range of 10-50 mm have been widely studied for various research purposes, from developing electrode materials/structures to testing new cell chemistries [12, 13, 14, 15, 16, 17]. However, to provide a competitive specific energy, it was suggested that the diameter of the useful BASE in a planar NBB cell should be at least 80 mm [30]. Even though several groups of pioneers [30, 31, 32] and the posterior industries and research institutions have delivered insights regarding planar NBB cells for high-power energy storage, no NBB cells with a planar design have been successfully reported for practical applications.

One of the critical issues in developing practical planar NaS cells is the thermo-mechanical fracture in the BASE or cell joint area, which can consequently lead to a catastrophic cell

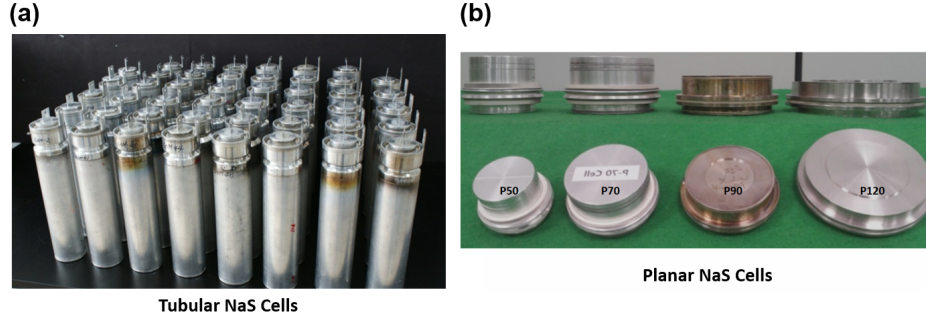


Figure 2.1: Representative NaS cell shapes of (a) tubular and (b) planar designs.

failure upon assembly, operation or maintenance of cells. The BASE in NBBs must be manufactured into a very thin membrane (as thin as 0.6 mm) targeting to a higher ionic conductivity. If the embedded BASE membrane is fractured during the operation cycles, a violent reaction will happen by directly connecting the reactive anode and cathode materials. Adding ZrO_2 or Ytria-stabilized zirconia (YSZ) into the β/β'' -alumina matrix is a typical approach to improve the strength and fracture toughness of the solid electrolyte for NBBs [33]. The sealing performance of the cell joints is also vitally important in securing the cell safety. When the molten active materials leak from the broken area of cell joints, a fire incident might be caused by the short circuit between adjoining cell parts in a NBB system [34]. To build robust cell joints and to avoid undesired cell failure, advanced modern joining techniques are generally applied, such as thermal compression bonding (TCB) for metal-to-ceramic seals, glass sealing (GS) for ceramic-to-ceramic seals, and electron beam welding (EBW) for metal-to-metal seals [35, 36, 37]. The fracture in the BASE or cell joint areas is typically induced by the accumulation of thermo-mechanical residual stress during the cell assembly, operation, and/or maintenance processes [24, 25, 34]. This residual stress accumulation essentially originates from dissimilar coefficients of thermal expansion (CTEs) of cell constituent materials including metals, ceramics, and glasses. Especially with increasing the cell sizes, the issue of thermo-mechanical stress accumulation in the joint parts and BASE becomes more serious in a planar NBB system because the dimensions of the cell joints and BASE will directly increase with enlarging the cell size. Such thermo-mechanical

failure in the cell joints and BASE areas is currently identified as the major roadblock to develop large planar NaS cells for advanced ESSs even with the application of aforementioned TCB, GS, EBW sealing techniques and β/β'' -alumina composites reinforced with YSZ. With the limitation of bonding strength in the cell joints and the fracture strength of BASE, in this work, we tested the impacts of cell container materials on the thermo-mechanical residual stress accumulation of a planar NaS cell using a finite-element analysis (FEA) computational approach. Although the cell container material types would greatly affect the degree of thermo-mechanical stress concentration during the cell assembly, operation, and maintenance, a quantitative assessment of such cell container material impacts has not been reported for modern planar NaS systems. In an effort to comprehensively monitor the variations of the thermo-mechanical residual stress concentrations in various cell parts, analyses using position-temperature-stress contour maps have been performed.

2.2 Computational method

2.2.1 Digital construction of prototype planar NaS cells

The cross-sectional structure of a prototype planar NaS cell design used in this work is provided in Figure 2.2(a) along with the enlarged images of selected individual cell compartments. The prototype planar NaS cell had a height of 34 mm and the BASE disk diameter of 90 mm. The disc size of BASE was set to 90 mm, as it was claimed that the minimum useful BASE diameter is 80 mm and the optimum disc size is 250 mm [30, 34]. As illustrated in the figure, a 30 °C slice of the circular planar cell has been used by imposing the axisymmetric boundary condition (BC). The figure also shows the heterogeneous joints comprised of insert metals (IMs, Al3003) to seal metallic cell container and ceramic insulating header (IH, α -alumina), and GS to seal BASE and IH. For convenience, the upper and lower IMs are referred to as IM1 and IM2. The commercial hyperMesh (version 14.0, Altair Engineering Inc.) software has been used to generate the FEA meshes of fine quality as shown in

Figure 2.2(a). The element type used for all the cell components was an 8-node linear brick, reduced integration, hourglass control hexahedral element (C3D8R) with varying sizes that were optimized depending on the dimensions of the related cell components. The total number of FEA elements of the 30 °C slice model was 206,238. After building the mesh for each component, the digital structures were exported to ABAQUS/CAE (version 6.11-2, Simulia Inc.) FEA software package. Due to the circular geometry of the prototype planar NaS cell design used in the present study, a cylindrical coordinate system was adopted with an axisymmetric BC for the computation and post-analysis. As indicated in Figure 2.2(a), the three directions (radial: r , circumferential: θ , and height: z) in the cylindrical coordinate system are defined as 1, 2, and 3, respectively.

2.2.2 Cell container material types

Four different material types including an aluminum alloy (Al3003), stainless steels (STS304 and STS430), and an iron-nickel-cobalt superalloy (KOVAR) were set as the candidate cell container materials. The planar NaS cells made up of these container materials are referred to as Al3003, STS304, STS430, and KOVAR cells, respectively. These materials have been particularly selected as the cell container parts (*i.e.*, collars, caps, and sodium cartridge) taking into consideration of their good corrosion resistance, weldability, and machinability [24, 25, 34]. In Figures 2.2(b) and (c), we show the CTE and elastic modulus variations as functions of temperature for these four different materials. Stainless steels generally are more expensive and has lower machinability compared with Al3003, but their CTE values are closer to those of α - and β/β'' -alumina. KOVAR is the most expensive among the four candidates, however, it possesses a much lower CTE comparable to those of glass or ceramics. Accordingly, KOVAR has been widely used in metal-to-ceramic or metal-to-glass bonding in minimizing the interfacial strain/stress resulted from temperature changes [38, 39, 40, 41, 42, 43]. The stress-strain curves at various temperatures for these four potential cell container materials are provided in Figure 2.4, which clearly shows the large

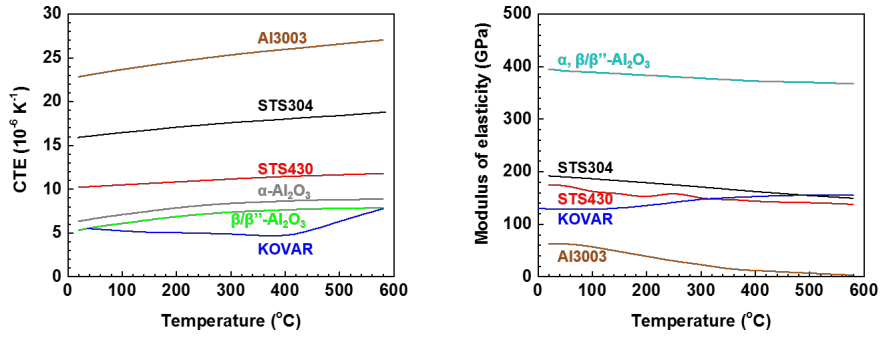
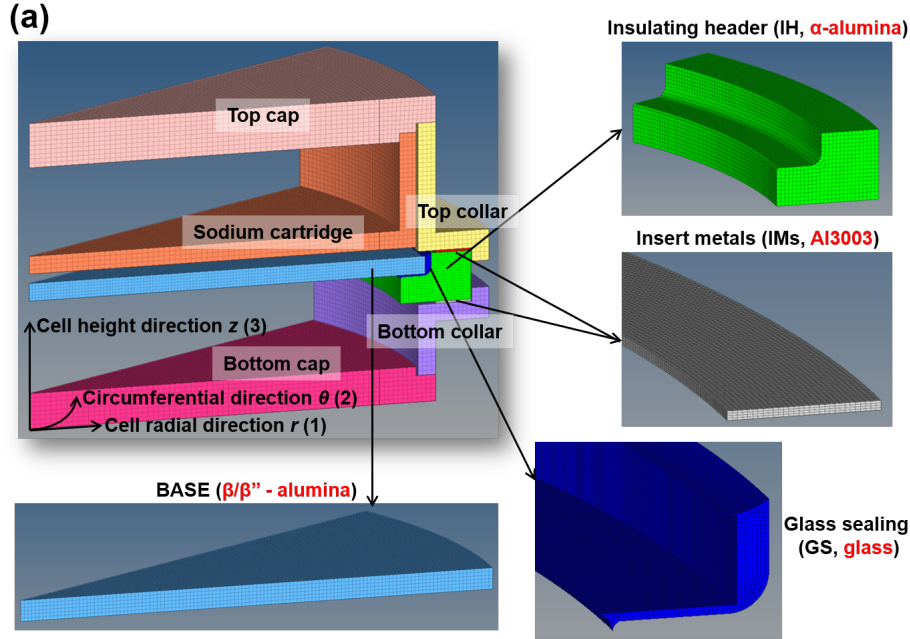


Figure 2.2: (a) Cross-sectional structure of a prototype planar NaS cell, and (b) CTE and (c) elastic modulus variations with temperatures for cell container and α -, β/β'' -alumina materials.

differences in their magnitudes and temperature-dependencies.

In Tables 2.1 and 2.2, we summarized the cell constituent material types and their thermo-mechanical material properties, respectively, used in the current work. As shown in Table 2.1, Al3003 alloy is applied for IMs because of its good stress absorption capability [24, 25]. The material properties in Table 2.2 were obtained based on the previously reported values [24, 25, 34, 44, 45, 46, 47, 48, 49, 50, 51, 52, 53] or measured at RIST (Research Institute of Industrial Science and Technology, South Korea). In constructing the digital structure of planar NaS cells, each component was assumed as homogeneous and isotropic solid materials.

Table 2.1: Constituent material types of planar NaS cells used in this work.

Cell components	Materials
Collars (top collar and bottom collar)	STS430/STS304/KOVAR/Al3003
Caps (top cap and bottom cap)	STS430/STS304/KOVAR/Al3003
Sodium cartridge	STS430/STS304/KOVAR/Al3003
Insert metals (IM1 and IM2)	Al3003
Insulating header (IH)	α -Al ₂ O ₃
BASE	β/β'' -Al ₂ O ₃
Glass sealing (GS)	Glass

Table 2.2: Thermo-mechanical properties of the cell materials in the temperature range of 20~520 °C.

Materials	CTE ($\times 10^{-6}$ K ⁻¹)	Poisson's ratio	Modulus of elasticity (GPa)	References
STS304	15.9-18.5	0.3	153-192	[45, 46, 47, 48]
KOVAR	4.7-6.3	0.317	129-154	[49, 50, 51, 52, 53]
STS430	10.2-11.7	0.28	139-175	[24, 25, 34]
Al3003	22.8-27	0.33	5-62.5	[24, 25, 34]
α -Al ₂ O ₃	6.3-8.8	0.23	368-395	[24, 25, 34]
β/β'' -Al ₂ O ₃	5.3-7.8	0.23	368-395	[24, 25, 34]
Glass	6.9	0.22	62	[24, 25, 34]

2.2.3 Computational conditions

The thermal loading conditions that are typically assigned to the NaS cell assembly, operation, and maintenance process can be found elsewhere [24, 25, 34]: 950 °C (GS joining process) \rightarrow 20 °C \rightarrow 520 °C (cell joint assembly) \rightarrow 20 °C (cell container assembly) \rightarrow 350 °C (cell operation) \rightarrow 20 °C (cell maintenance). The cell operation and cell maintenance recur in cycles depending on the maintenance schedule (typically every 4 to 5 years). Considering the rubbery nature over the glass transition temperature and the nearly elastic characteristics of glass materials, it was suggested that simplified temperature profile is adequate for the FEA thermal loading conditions [25, 34]. Therefore, the FEA computation step incorporated in this work is divided into 3 steps given by: (i) cell joint assembly and freeze (520 \rightarrow 20 °C), (ii) cell container assembly to thaw for cell operation (20 \rightarrow 350 °C), and (iii) cell operation to freeze for cell maintenance (350 \rightarrow 20 °C). Here, only the first cell operation and maintenance cycle was modeled. As a displacement BC, the vertical displacements for the outer edge of the bottom surfaces in the assemblies (*i.e.* bottom collar or bottom cap) were fixed. All the interfaces between two adjacent cell components were tied together assuming non-sliding, high-friction conditions.

2.3 Results and discussion

In Figure 2.3(a), we first show the deformation behaviors and the von-Mises stress distributions (in MPa) of cells with various cell container materials after freeze (520 \rightarrow 20 °C) and thaw (20 \rightarrow 350 °C). The deformation and the von-Mises stress are represented using the cell shapes and the color distributions in the figure. Here, the degree of deformation is magnified by a factor of 10 for visual clarity. After the joint assembly, when the temperature is decreased from 520 to 20 °C, one can clearly notice that the radial contraction degrees of the collars are in the sequence of Al3003 > STS304 > STS430 > KOVAR cells. This is because the general CTE values of the associated materials in most of the temperature

ranges are decreased in the order of Al3003 > STS304 > STS430 > ceramics > KOVAR, as shown in Figure 2.2(b). In fact, for the KOVAR cell case, the freeze (520 \rightarrow 20 $^{\circ}$ C) process leads to a ‘relative’ expansion of cell collars with reference to the IH position, as CTE of KOVAR is lower than those of α - or β/β'' -alumina. The deformation behaviors during freeze can be explained by the contraction mechanism illustrated in Figure 2.3(b). Because the CTE values of metallic components are higher than that of ceramic parts (except KOVAR), the relative strain of metallic parts must be higher than that of ceramic parts upon cooling. In the figure, the red arrows represent the displacement aspect of metallic parts while the blue arrows represent the displacement aspect of ceramic parts. In a cooling process, the planar cell would contract in the radial direction, as indicated by the arrows #1, 3, 6, 7, 8 and 10. In this situation, because the metallic components shrink more towards the center of the cell, it gives rise to normal tensile stresses in the cell height direction, as indicated by the arrows #2, 4, 5 and 9. Upon heating (*i.e.*, 20 \rightarrow 350 $^{\circ}$ C), the container expands radially, inducing the normal compressive stresses along the cell height direction. In this case, the displacements will take place in the opposite directions of Figure 2.3(b).

After thaw, when the cell temperature is increased from 20 to 350 $^{\circ}$ C, it is seen that the Al3003 and STS304 cells still show severe deformations with a higher degree of distortions in the cell containers. Although the deformation amount is magnified by 10-fold, these results already indicate the benefits of applying STS430 or KOVAR alloys. In addition to the cell shape changes after freeze and thaw, the von-Mises stress contours presented in Figure 2.3(a) also clearly manifest the general influences of fabricating planar NaS cells with different container materials. In the figure, red-to-blue color legends with an identical scale for different materials are used to denote the maximum and minimum stresses, respectively, at each temperature. The ranges of the von-Mises stress distributions are varied from 3 to 373 MPa and from nearly 0 to 171 MPa after freeze and thaw, respectively, implying that the residual von-Mises stresses are partly recovered through the heating process. From the stress contours, it is expected that the STS304 cells would contain the highest residual stress

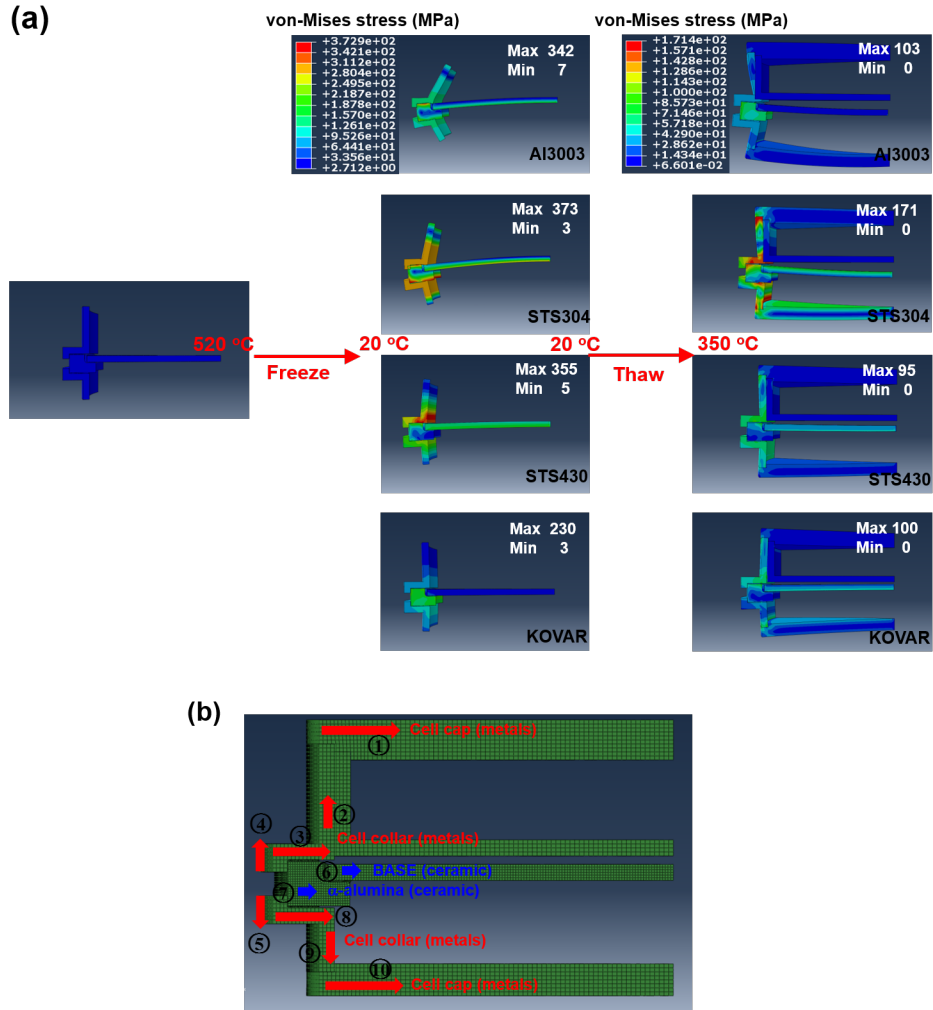


Figure 2.3: (a) Deformation behaviors (shapes) and von-Mises stress distributions (color contour) of cells with various cell container materials after freeze (520 → 20 °C) and thaw (20 → 350 °C), and (b) schematic to show the cell contraction aspect upon cooling. In Figure 2.3(a), the deformation amounts are magnified by 10 times for visual clarification.

despite the CTE of Al3003 is higher than that of STS304. These results come from the lower elastic moduli of Al3003 compared with that of STS304 (see Table 2.2 and Figures 2.4(a) and (b)). From the figure, the general trends for the accumulation of residual stresses in the cells are recognized as STS304 > STS430 ≈ Al3003 > KOVAR cells and STS304 > Al3003 ≈ STS430 ≈ KOVAR cells for the freeze and thaw processes, respectively. As previously addressed, the concentration of residual stress in the cell joint area is important, as the metallic cell cap would have a much higher tolerance to the stress and corresponding plastic

deformations. It is found that the trends for the stress accumulation in the cell joint areas of different cell types are similar as the overall trends, *i.e.*, STS304 > Al3003 > STS430 \approx KOVAR cells (see cropped images in Figure 2.5).

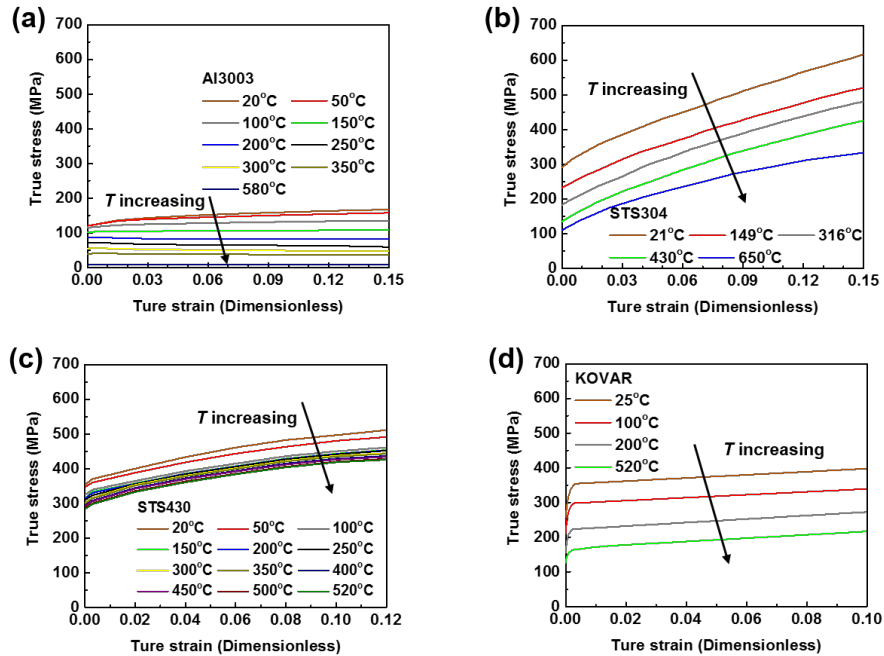


Figure 2.4: Stress-strain curves at various temperatures for (a) Al3003, (b) STS304, (c) STS430, and (d) KOVAR materials.

With this information, in the next sub-sections, we attempt to analyze details of the residual stress (*i.e.*, normal stress and shear stress) accumulations on various cell joint areas and BASE. The areas of interest include IH outer surfaces, IH/IM interfaces, and BASE surfaces. The residual stress on IH outer surface is of concern as the in-house experiments often encounter the cell fracture originated from this area, as reported in Reference [34]. The stress in the interfacial area between IH and IM need to be examined to gauge the reliability of TCB. In addition, from Figure 2.3(a), we showed that the thin and brittle BASE may bend during the cooling and heating cycles, which necessitates to closely track the residual stress distribution on it. None the less the von-Mises stress concentrations in the cell collars and caps could be comparably high after the freeze and thaw cycles, the concentration of thermo-mechanical stress in the metallic collars is not focused on here due to relatively higher

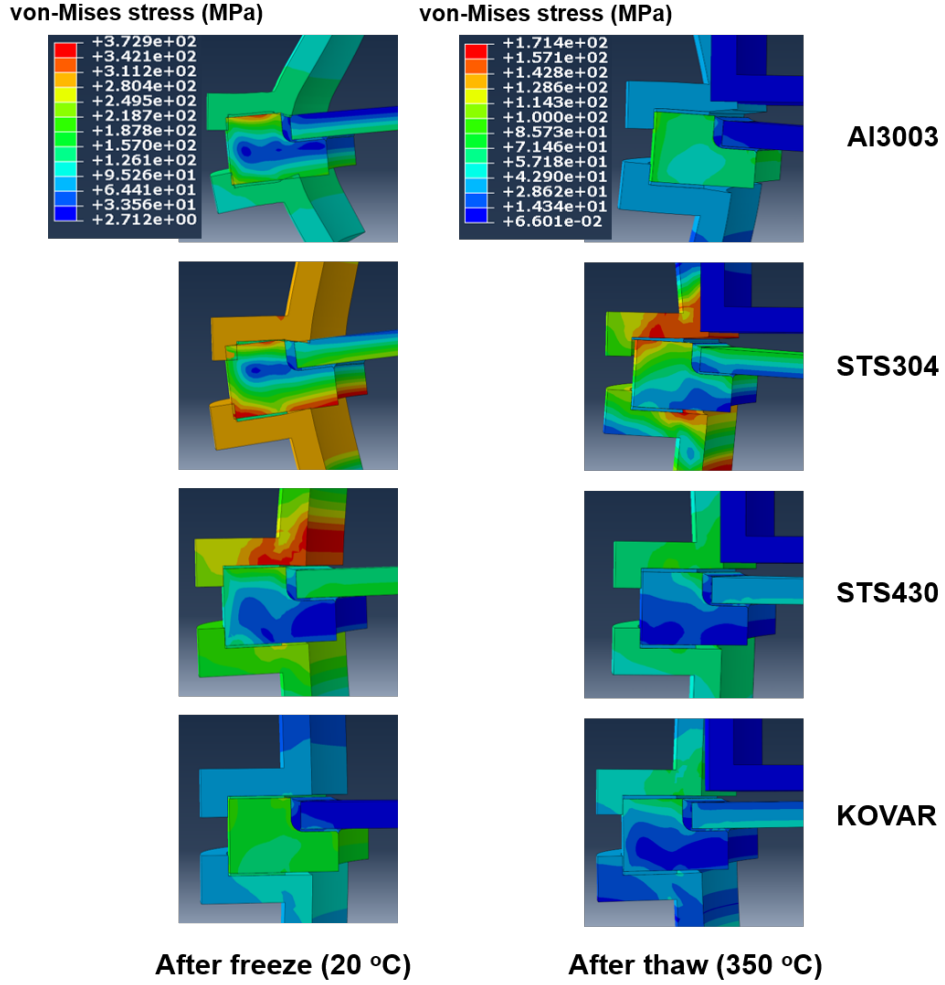


Figure 2.5: Cropped images from Figure 2.3(a) to show the deformation behaviors (shapes) and the von-Mises stress distributions (in [MPa], color contour) of cells with various cell container materials after freeze ($520 \rightarrow 20 \text{ }^\circ\text{C}$) and thaw ($20 \rightarrow 350 \text{ }^\circ\text{C}$) in the cell joint areas. The deformation amounts are magnified by 10 times for visual clarification.

fracture strength and robust metal-to-metal bonding in these areas.

2.3.1 Insulating header (IH) outer surface

The normal stress accumulation along the cell height direction on the outer surface of IH (*i.e.*, height normal stress, σ_{33}) is important because it is directly correlated with the mode I-type fracture from the IH outer side during the cell assembly, operation and maintenance processes. Figure 2.6 presents contour maps with a same legend scale showing the variations

of the calculated σ_{33} on the outer surface of IH. In the left-hand side image, the area of interest (*i.e.*, outer surface of IH) in the prototype cell system is indicated by the pink circle and black dashed line. In each contour map, the x- and y-axes denotes the positions on the IH outer surface (from top to bottom) and the temperature changes of computations upon cell assembly, operation, and maintenance. The same 2D analysis contour map style with identical legend scale for each computational set is used in the following Figures 2.7, 2.9, and 2.10. In the figure, the local peak positions along with their maximum and minimum values of σ_{33} are also contained in each contour map. From the figure, one can clearly notice that, for the planar NaS cell systems fabricated using Al3003, STS304 and STS430, the IH outer surface continuously experiences accumulated tensile stresses in the freeze process after joint assembly (520 \rightarrow 20 °C). In the following thaw process after container assembly (20 \rightarrow 350 °C), the concentrated tensile stresses are gradually released and less severe compressive stresses can be accumulated. Finally, when the system is cooled down for maintenance (350 \rightarrow 20 °C), σ_{33} shows a similar distribution to the one after the cell joint assembly and freeze (520 \rightarrow 20 °C). On the contrary, the σ_{33} distributions on the IH outer surface of KOVAR cell exhibit a nearly opposite trend with the temperature changes. From 520 to 20 °C, σ_{33} exhibits a maximum tensile value, 50 MPa, at 412.5 °C but then decreases to show a maximum compression value, -100 MPa at 20 °C. When the cell temperature increases from 20 to 350 °C and decreases from 350 to 20 °C, calculated σ_{33} indicates local peak values of 46 and -92 MPa, respectively. This opposing trend for the contours of IH outer surface σ_{33} in the KOVAR cell can be attributed to the lower CTE of KOVAR relative to α - and β/β'' -alumina as discussed previously.

In addition to the general distribution of σ_{33} on the IH outer surface, the peak values that the cells would experience are clearly different depending on their container material types. For the Al3003, STS304, and STS430 cells, the peak tensile σ_{33} on the IH outer surface is obtained at 20 °C (either at the cell container assembly temperature or the maintenance temperature) with the peak values of 188, 231, and 166 MPa, respectively. However, for

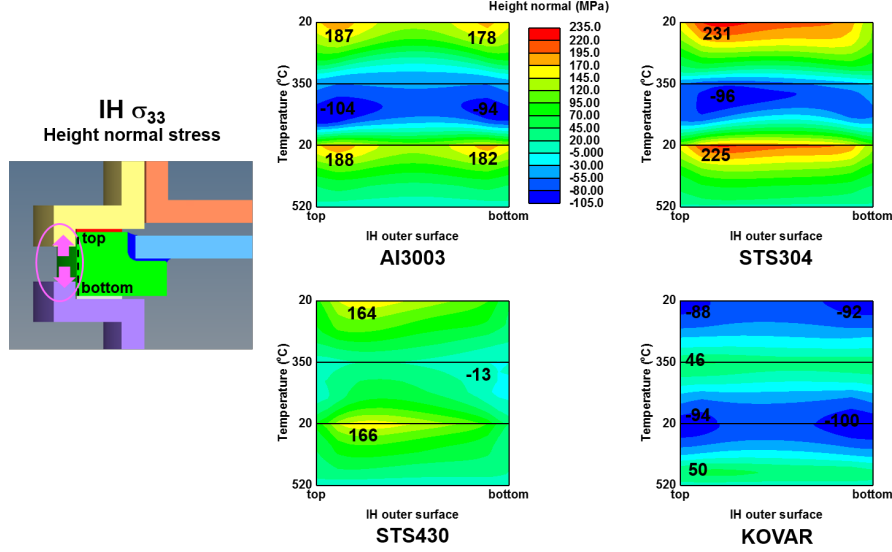


Figure 2.6: Height normal stress (σ_{33}) distributions on the outer surface of IH with cell temperature changes for four prototype planar NaS cells.

the KOVAR cell, the maximum tensile σ_{33} is captured at 412.5 °C with a value of 50 MPa, much smaller than those of the cell systems made up of other three alloys. Here, we focused only the tensile component for IH outer surface σ_{33} because the tensile strength of ceramic materials is typically much important; the bulk tensile strength of tensile strength is ca. 200-500 MPa while the bulk compression strength is ca. 1500-2500 MPa for typical α -alumina materials [34]. In the Al3003 cell case, there are two peaks of tensile σ_{33} at 20 °C indicating the most likely regions of potential thermo-mechanical fracture. The STS304 and STS430 cells show one peak of tensile σ_{33} located near the top position of IH outer surfaces at two different 20 °C. In the KOVAR computation results, one peak of tensile σ_{33} is located near the top of IH outer surfaces at 412.5 °C (during freeze after cell joint assembly) and at 350 °C (during cell operation). All of these peak positions of high σ_{33} correspond to the regions near the end of direct contact between IH and IM.

The critical crack size (a_c) that would initiate the spontaneous crack propagation on these IH outer surfaces can be estimated using the classical Griffith brittle fracture criterion: $a_c = (K_{IC}/f\sigma_{app})^2/\pi$, where a_c , K_{IC} , f and σ_{app} are the critical crack length in an infinite plate, fracture toughness, a shape parameter determined by the specimen and crack geometry,

Table 2.3: Critical crack lengths (a_c) on the outer surface of IH in the prototype planar cells with different container materials.

Container materials	a_c (μm)	
	$f=0.60$	$f=1.12$
Al3003	225~400	64~114
STS304	148~263	42~75
STS430	288~510	82~147
KOVAR	3205~5700	920~1630

and applied tensile stress, respectively. Given that $K_{IC} = 3.0 \sim 4.0 \text{ MPa}\sqrt{\text{m}}$ for typical alumina materials and the shape factor $f = 0.60 \sim 1.12$ for a semi-circular crack on the surface ($f = 0.6$, the largest critical crack size but the semi-circular crack has a length of $2a_c$) and a through-edge crack on the IH outer surfaces ($f = 1.12$, the smallest critical crack size), the estimated ranges of a_c for various cell types are summarized in Table 2.3. For cracks with other shapes, the critical lengths will fall between these two extreme case results. Using modern techniques for synthesizing α -alumina IH, if the largest crack size is maintained below ca. $100 \mu\text{m}$, which corresponds to the in-house experimental observations, then applying Al3003, STS304, and STS430 container materials will have some probabilities for cell fracture, depending on the existing crack shapes, from the outer surface of IH at the cell container joint temperature and the cell maintenance temperature. On the other hand, the KOVAR cell modeled using the current prototype planar NaS design with a BASE disk size of 90 mm will unlikely to initiate crack propagation and subsequent cell fracture from this IH outer surface.

2.3.2 Interface between insulating header (IH) and insert metals (IMs)

Shear stress on IH top surface

The shear stress component along the cell radial direction (radial shear stress, σ_{13}) at the interfaces between IH and IM is also important because it can lead to interface decohesion

when the accumulated stress is greater than the shear bonding strength between IH and IM. In Figure 2.7(a), we provide σ_{13} distributions on the IH top surface that is in contact with the bottom surface of IM1 using contour maps for Al3003, STS304, STS430, and KOVAR cells. The area of interest is indicated by the pink ellipse with dashed line in the left-hand side cross-section image. The edge positions of the contacting IM1 are given by the black dotted lines in each contour map. It is found that two peaks of σ_{13} are located near the outer and inner edges of the IH/IM1 interfaces at 20 °C (cell container assembly temperature and maintenance temperature), with the σ_{13} at the outer edge being relatively larger. The respective maximum peak values of σ_{13} on the IH surfaces for the Al3003, STS304, STS430, and KOVAR cells are 70, 84, 77, and 21 MPa. In this shear σ_{13} case, the magnitude is important because the sign of σ_{13} merely dictates the direction of stress that can both initiate the interfacial decohesion, negative being the inward shear and positive being the outward shear, respectively. From these results, it is predicted that the KOVAR cell would not initiate the interfacial decohesion along the IH/IM1 interface, as the shear bonding strength of Al3003 IM and α -alumina IH is expected to be over ca. 100 MPa [34]. Using other three alloys as the container materials for the prototype planar cells, however, would increase the probability of the decohesion between IH/IM1 interface depending on the interfacial bonding conditions to contain imperfections and/or impurities.

Normal stress on IH top surface

Now, in Figure 2.7(b), we show the normal stress distributions along the cell height direction (height normal stress, σ_{33}) on the top surfaces of IHs for four different cell types. As before, the black dotted lines again represent the edge positions of IM1 in touch with IH. After freeze at 20 °C (cell container assembly temperature and cell maintenance temperature), the predicted maximum tensile σ_{33} on the IH top surface near the outer edge is approximated as 165, 160, and 100 MPa for Al3003, STS304, and STS430 cells, respectively. In the KOVAR cell case, maximum σ_{33} on the IH top surface is observed at the cell operation

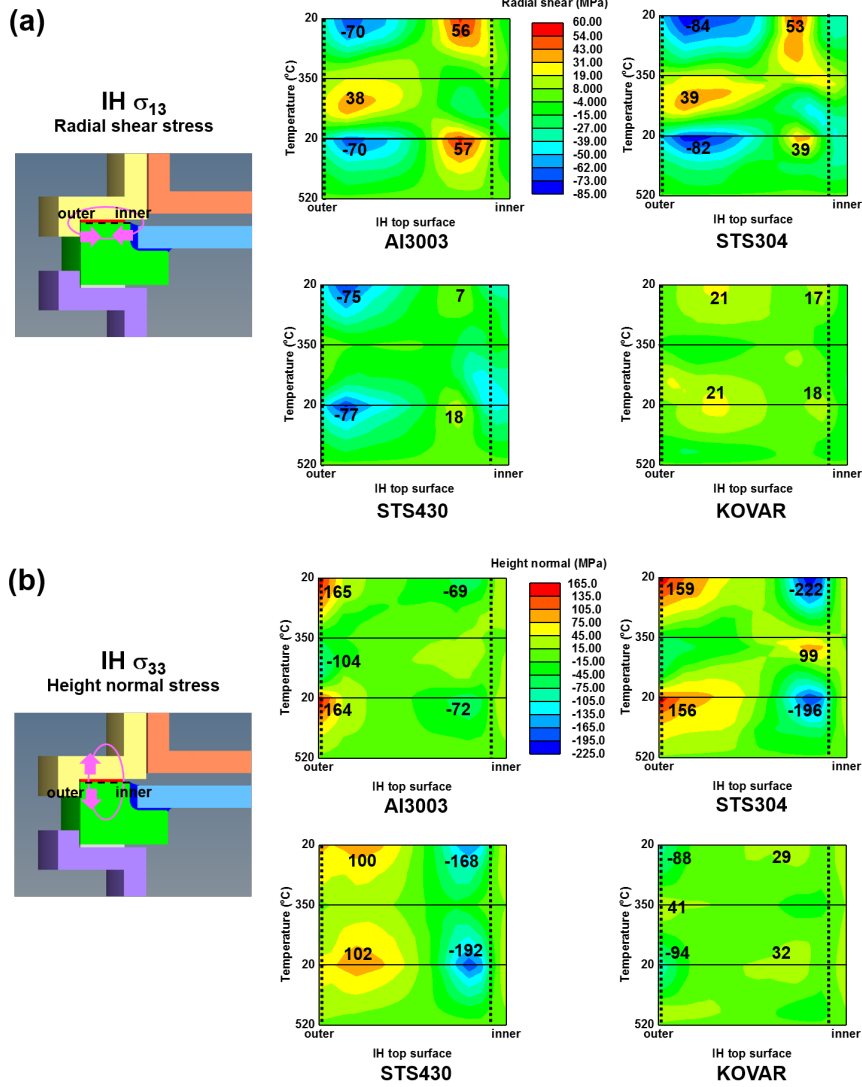


Figure 2.7: (a) Radial shear stress (σ_{13}) and (b) height normal stress (σ_{33}) distributions on the top surface of IH with cell temperature changes for four prototype planar NaS cells.

temperature, 350 °C, again near the outer edge. Because the normal bonding strength of IH/IM is measured as ca. 40-80 MPa in the in-house experiments, it is highly likely that the interfacial failure of IH/IM for Al3003 and STS304 cells can be initiated from the IH edge side even in the cell assembly stage. Given that the maximum tensile σ_{33} position is not at the edge location, the chance of interfacial fracture for the STS430 cell would be much smaller than those of Al3003 and STS304 cells, as the interfacial decohesion is experimentally observed to be originated from the bonding edge area. For the KOVAR cell, the maximum

σ_{33} falls in the range of ca. 30-40 MPa, which may or may not give rise to the interfacial decohesion through the normal stress failure mechanism. Here, the compression σ_{33} is not focused on, as the it would not majorly influence the interfacial decohesion through the normal failure mechanism. From these results, it is suggested that applying the KOVAR materials would much increase the cell safety and security by reducing the probability of IH/IM interfacial decohesion. Note that the shear and normal stress accumulations along the interface of IH/IM1 have been discussed here. This is because the stress distributions with changing temperatures for σ_{13} and σ_{33} components in the IH/IM2 are lower or nearly comparable to those in the IH/IM1 (see Figure 2.8 to show the contour maps of (a) radial σ_{13} and (b) normal σ_{33} distributions on IH surfaces with changing temperatures along the interfaces of IH/IM2 for the STS304 cell, as examples).

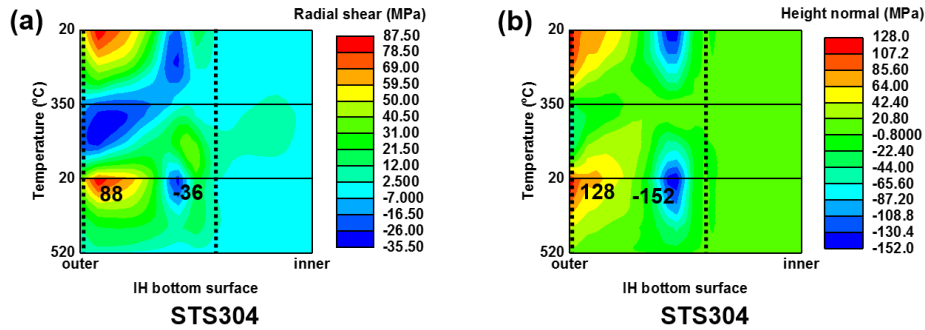


Figure 2.8: Contour maps of (a) radial shear σ_{13} and (b) height normal σ_{33} distributions on IH surfaces with changing temperatures along the interfaces of IH/IM2 for the STS304 cell.

The black dotted lines in each map indicate the edge positions of IM2 in direct contact with IH bottom surface.

Shear and normal stresses on IM1 bottom surface

Figure 2.9(a) provides the radial shear stress (σ_{13}) distributions on the bottom surface of IM1 in the cells with four distinct container materials. As the radial dimension of IM surface is smaller than that of IH surface, the IM edge lines shown in Figure 2.7 are not shown here. From the computation results, when the cell container materials altered from Al3003, STS304, STS430 to KOVAR, the maximum local σ_{13} on the IM1 bottom surface are identified

as -91 , -96 , -86 and 48 MPa, respectively, near the outer edges of IM1. Again, considering that the shear bonding strength of IH/IM is over ca. 100 MPa, these σ_{13} concentrations in four cell types may not result in the interfacial fracture due to the concentration of interfacial σ_{13} . However, similar to the analysis of σ_{13} in the IH/IM1 interface from the IH surface, the Al3003, STS304, and STS430 cells have a high risk of potential decohesion of the IH/IM1 TCB, whereas the KOVAR cell is unlikely to show the bonding fracture through the interfacial shear decohesion mechanism. In Figure 2.9(b), we now present the predicted results of the height normal stress (σ_{33}) distributions on the IM1 bottom surfaces in the cells. The maximum tensile σ_{33} values on this IM1 surfaces are expected as 173, 130, 111, and 47 MPa for the Al3003, STS304, STS430, and KOVAR cells, respectively. As predicted from the σ_{33} variations on the IH surface, the analysis of σ_{33} concentration on the IM1 surfaces clearly shows that there is a high probability of interfacial decohesion initiated from the outer bonding edge for the cells made up of Al3003 and STS304 materials. It is also noted that, the general stress accumulation aspects and stress concentration positions coincide on both surfaces, *i.e.*, IH top and IM1 bottom surfaces. It is found that the degree of residual stress concentration is by and large higher on the IM1 side probably resulted from much higher deformation of metallic components.

2.3.3 alumina solid electrolyte (BASE) surfaces

Finally, in Figure 2.10, the calculated normal stress distributions along the cell radial direction (σ_{11} , radial normal stress) on the top surface of BASE upon cell temperature changes for the prototype planar NaS cells with various cell container materials are presented. In the BASE case, the radial normal stress σ_{11} concentration is important because it can cause the mode I-type fracture on the surface of BASE. From the figure, it is seen that σ_{11} on the top surface of BASE mostly changes homogeneously with temperature variations, except the outer edge regions. This is probably due to the direct contact with GS compartment, as marked by the black dotted lines in Figure 2.10 to indicate the GS edge positions. When

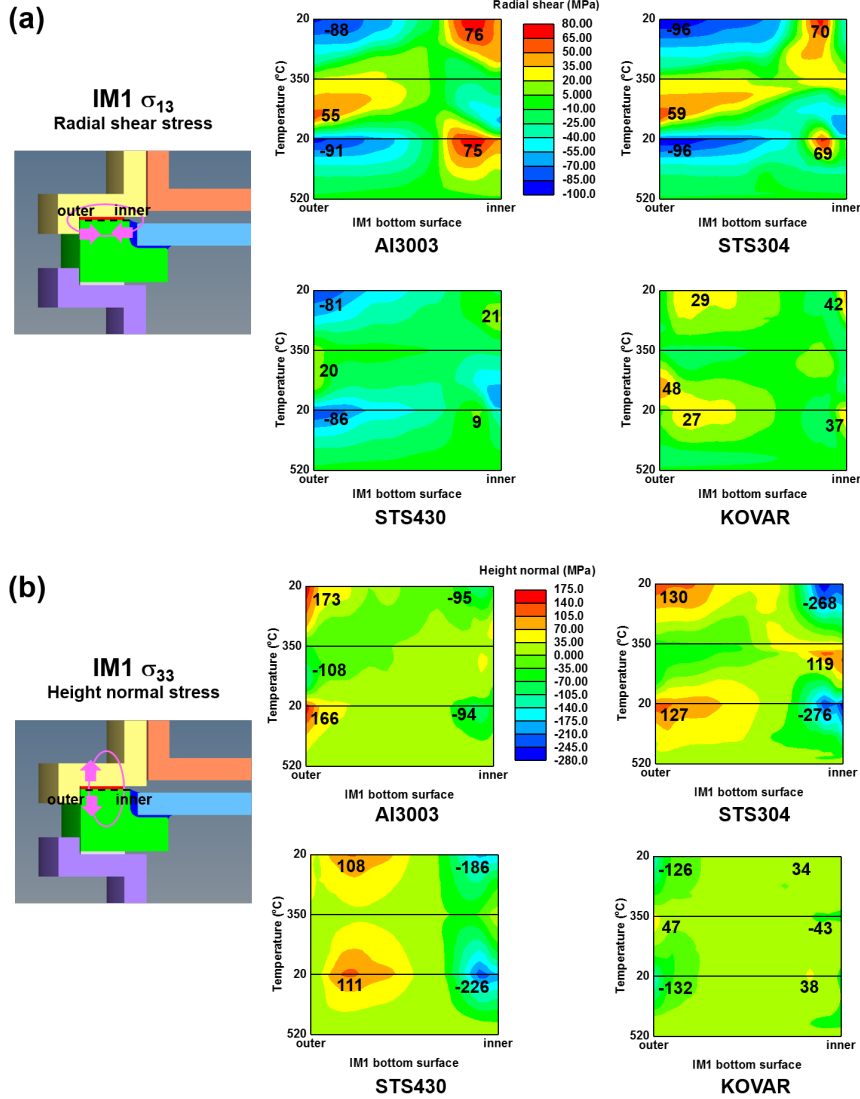


Figure 2.9: (a) Radial shear stress (σ_{13}) and (b) height normal stress (σ_{33}) distributions on the bottom surface of IM1 with cell temperature changes for four prototype planar NaS cells.

the maximum tensile σ_{11} on the top surfaces of BASE is compared for different systems, the sequence is lined up as, STS304 > Al3003 > KOVAR cells with their corresponding tensile σ_{11} values of 125, 43, and 16 MPa, respectively. It was calculated that, for the STS304 cell in particular, the concentrated radial σ_{11} on the top surface of BASE can reach as large as 125 MPa during the thaw process after the complete cell assembly. Although imposing tensile stress of 125 MPa on the BASE surface would not directly lead to an electrolyte

fracture, given that very thin disc shaped geometry of BASE can be distorted, it is thought that applying STS304 materials as the container of cell is not feasible for the prototype planar design considered in this work. For STS430 cell, the radial σ_{11} stress is predicted to be all compressive throughout the entire temperature profile changes. For KOVAR cell, the trend of σ_{11} variations with temperature changes is opposite to the trend of Al3003 and STS304 cells because of lower CTE values of KOVAR with respect to the CTEs of α - or β/β'' -alumina. Also, note that the computation results presented in Figure 2.10 are based on an idealized experimental condition. Therefore, any imperfections in the experimental conditions and/or material preparations such as non-flat BASE and off-centering of BASE may substantially increase the residual stress accumulation and subsequent cell failure. Here, the results of radial σ_{11} distributions only on the top surface of BASE are discussed because higher tensile stress is concentrated on the top surface probably due to the geometrical proximity to the metallic components (*i.e.*, top collar) of the cell. For reference, the calculated results of radial σ_{11} distributions on the bottom surface of BASE for four cell systems are given in Figure 2.11.

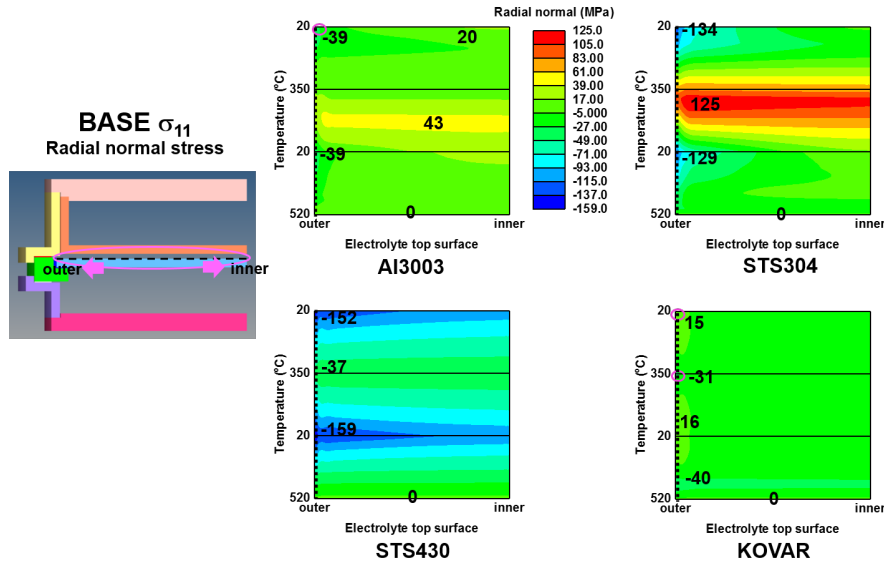


Figure 2.10: Radial normal stress (σ_{11}) distributions on the top surface of BASE with cell temperature changes for four prototype planar NaS cells.

In Figure 2.12, we summarize the predicted maximum local stress concentrations at

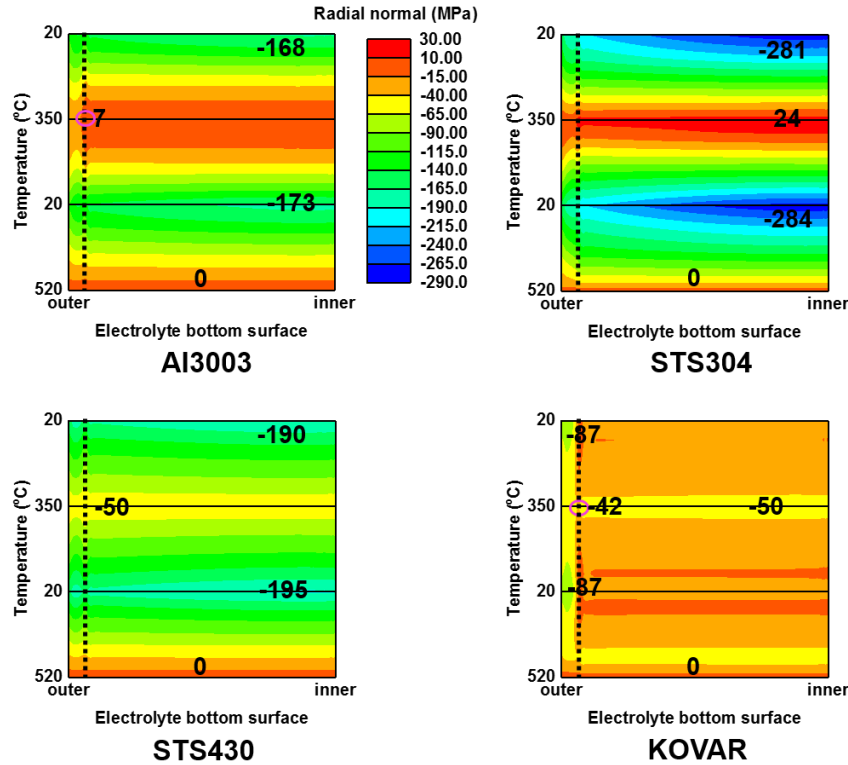


Figure 2.11: Radial normal stress (σ_{11}) distributions on the bottom surface of BASE with cell temperature changes for the prototype planar NaS cells with various cell container materials. The black dotted line in each map indicates the edge position of GS in direct contact with BASE bottom surface.

various cell components for four prototype planar NaS cells. In the first set (far left-hand side column set), the maximum von-Mises local stress in the cell for different cell types is shown, and the rest of sets are indicated by the stress component (σ_{33} , σ_{13} , or σ_{11}) with corresponding cell parts (IH, IM1, or BASE). Some of the data in BASE are missing in Figure 2.12 because only the tensile stress is included for the normal stress components. From the summary figure, using Al3003 or STS304 materials are seemingly impractical; these materials may result in a cell failure originated either from the IH outer surface or from the bonding delamination between IH/IM. STS304 cell may contain a high probability of BASE failure depending on the cell fabrication conditions. It is surmised that applying STS430 is better than Al3003 and/or STS304, however, it may also possess a chance of IH/IM bonding decohesion. On the other hand, one can readily recognize that incorporating KOVAR as the

cell container material would exhibit high benefits to reduce the accumulated residual stresses in nearly all of the cell compartments. It is understood that adopting relatively expensive KOVAR materials into the cell container can present a challenge for commercialization of cells by reducing the manufacturing cost. Nevertheless, through the current computation modeling study, we clearly demonstrate that employing alloy systems with lower CTE values (*i.e.*, lower than CTE of STS430) is necessary to develop a safe and secure planar NaS cell. Lastly, it must be again addressed that, the computation results and analyses shown in this work are based on the prototype planar NaS cell design with a BASE disk diameter of 90 mm, which is contemporarily regarded as the largest fabricable planar NaS cell. If the cell size is increased beyond 90 mm, the impacts of cell container materials on the residual stress accumulation will become more critical as the deformation amount during the assembly and cell cycles is increased.

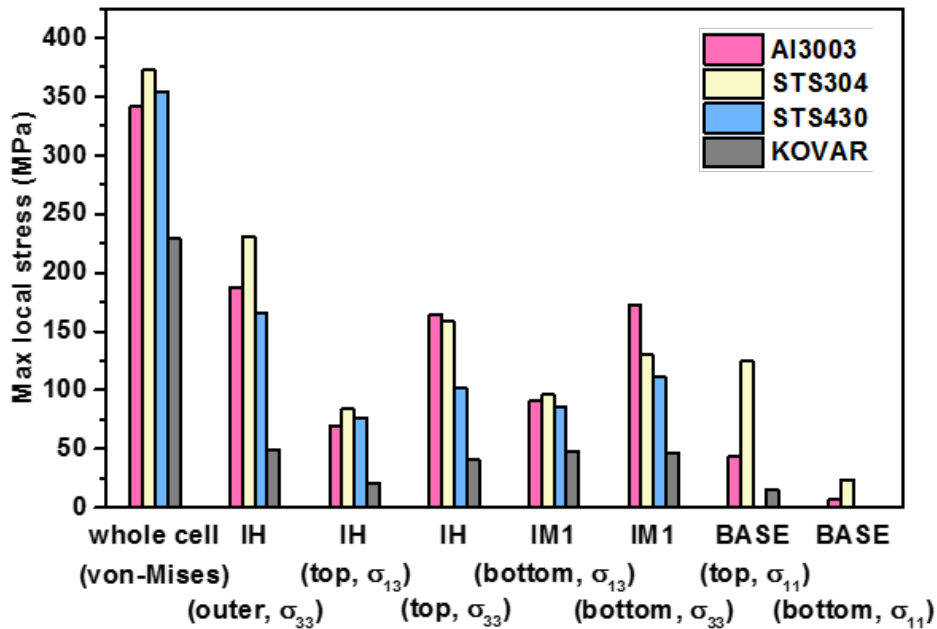


Figure 2.12: Summary of predicted maximum local stress concentrations at various cell components for the four prototype planar NaS cells.

2.4 Conclusions

Based on a prototype cell design, a series of FEA computational assessments have been performed on the thermo-mechanical residual stress accumulations in the cell joint areas and BASE components of contemporary planar NaS cells with different container materials.

- The maximum local shear or tensile stresses in IH, IM1 and BASE of cells with different container materials are schematically illustrated in the summary chart presented in Figure 2.12. It can be seen that using KOVAR as the container material (presented by the grey columns in Figure 2.12) can considerably reduce the thermo-mechanical stresses in the joint part, thereby increasing the thermo-mechanical stability and safety of the P90 cell.
- The height normal tension at IH/IM1 interface will cause the decohesion of the TCB either from the IH side or the IM1 side. In other words, if a P90 NaS cell is broken, the most possible reason is the mode I decohesion of the IH/IM1 seal. For the cell using Al3003 as container material (presented by the pink columns in Figure 2.12), the decohesion at IH/IM1 interface will take place at the outer edge of the interface either from the IH side or the IM1 side during step #1. For the cell with STS304 as container material (illustrated by the yellow columns in Figure 2.12), the decohesion of the IH/IM1 interface will initiate at the outer edge from the side of top surface of IH during the computation step #1. For the cell employing STS430 as container material (presented using the blue columns in Figure 2.12), the decohesion of IH/IM1 interface will happen either from the IH side or the IM1 side during step #1 and the decohesion position is near the outer edge of the interface. Even applying KOVAR can greatly reduce the thermo-mechanical stresses in the P90 cell, it can still encounter a decohesion either from the IH or the IM1 side near the inner edge of the interface which may initiate in step #1 except the normal bonding strength can achieve beyond 47.2 MPa.

- The BASE is relatively safe because the relatively small normal stresses accumulated on its top and bottom surfaces. This may indicate that a thinner BASE design can be applied in the P90 cell system.

Chapter 3

PLGA-based drug carriers

3.1 Introduction

Over the past several decades, poly(lactic acid) (PLA), poly(glycolic acid) (PGA) and their copolymer, poly(lactic-co-glycolic acid) (PLGA), have received rapidly increasing research interest, from textiles and packaging industry to more sophisticated absorbable surgical fibers and drug delivery devices because of their characteristic biodegradability and biocompatibility [54, 55, 56, 57]. Out of these, drug delivery device products are one of the most important sectors for the application of PLGA-based materials. The drug release behaviors from PLGA-based drug delivery systems can be dictated by the physicochemical properties of PLGA copolymers, such as degradation rate, which can be adjusted by molecular weight (M_w), monomers ratio, and monomer sequence [55, 56]. For example, it is well known that degradation and drug release rate will be accelerated with decreasing molecular weight of PLGA and increasing the glycolic acid (PGA) ratio of PLGA copolymers [56, 58, 59]. Other than the properties of PLGA copolymers, there are numerous other factors including drug type (hydrophilic or hydrophobic), drug molecule size, acidity of drugs, and device shape that can substantially influence degradation rates and concurrent drug release behaviors of PLGA-drug products [56].

Among these factors, the structures of PLGA-drug materials could play an essential role in determining the release characteristics. The most studied aspects are drug loading and PLGA polymer matrix size, especially after recent advances that have been made for controlling drug loading and micro-/nanosphere size during production [60, 61]. For instance, Acharya *et al.* [61] have observed the faster drug release from smaller micro particle size of PLGA-felodipine microcylinders. In addition to drug loading and polymer matrix size, the size of drug particles embedded in the polymer matrix also can influence drug release kinetics [62, 63]. Other microstructural features, such as micro phase-separated morphology of block PLGA components, can also profoundly impact drug release. For example, increased drug polymer phobicity and drug loading could lead to drug and polymer separating into compact, drug-rich domains, within a polymer-rich matrix. Choi and coworkers [64] investigated the release of sirolimus from PLGA matrix for the application of drug-eluting stents (DES). Their findings proved that, in the larger drug-rich regions, the faster the drug was released in vitro due to water absorption and swelling. It is likely that the miscibility/immiscibility between PLGA and drug also substantially affects drug-rich domain distribution and size in the continuous polymer phase. Since the two monomers of PLGAs, PLA and PGA, would exhibit different thermodynamic activities, the different sequences can markedly influence the hydrolysis and drug release kinetics from PLGA-based drug delivery systems [65].

In this part of work, we combined the multi-scale modeling (*i.e.*, atomistic and meso-scale computations) and experimental approaches to understand the thermodynamic interactions of polymer-drug and resulting structural evolution of PLGA-tetracycline hydrochloride films. Tetracycline hydrochloride (TC-HCl, referred to as “TC” for simplicity in the following manuscript) was used in this study because it is relatively inexpensive, safe to handle, and broadly used in medical devices [66, 67, 68, 69]. For this, we quantified the polymer-drug interactions using Flory-Huggins parameter (χ) that is a criterion of miscibility/immiscibility of polymeric material systems. In quantifying such interaction parameters, an atomistic molecular dynamics (MD) computation technique has been employed in the

present work. In general, it is known that the thermodynamic data for PLGA-drug systems are not readily available and obtaining those material property data through experimental techniques requires higher challenges [70]. Replacing the experimental characterizations, an attractive alternative is to use theory and computation to establish the requisite thermodynamic properties in understanding the interaction in the drug-PLGA systems. In addition, the self-diffusion coefficients (D_{self}) of TC molecules in PLA and PGA polymers were separately calculated and they were correlated with the structural evolution. Using those material properties obtained through MD computations, meso-scale simulations were conducted using phase-field method (PFM) to predict the surface structures of PLGA-TC films. In conjunction with the computational simulations, two sets of PLGA-TC films having different copolymer ratios were experimentally fabricated and their surface structures were characterized to support the theoretical predictions.

3.2 Methodology

3.2.1 Computational section

Molecular dynamics (MD)

For atomistic MD computation to quantify the Flory-Huggins interaction parameters (χ), the Materials Studio commercial software package (version 7.0, Accelrys Inc.) has been used. Through a series of MD computations, the χ values for various PLA/PGA, PLA/TC, and PGA/TC systems were calculated separately. The PLA/PGA composition ratios were varied from 0/100 to 100/0 with a 10 wt% increment interval. In the PLA/TC and the PGA/TC systems, the drug ratios in the binary systems were 15 and 45 wt%. Polymer chains of PLA and PGA were firstly built with the number of the repeat monomer unit of 50, and the charge modification and the geometry optimization were conducted for the created polymer chains and the imported TC molecules. It is generally accepted that systems comprised of

polymer chains of 50 monomer units can successfully represent the bulk properties [71, 72]. The structures of PLA and PGA chains and TC molecule are shown in Figure 3.1(a). In the figure, the white, gray, red, blue, and green spheres represent the H, C, O, N, and Cl atoms, respectively. Cubic simulation boxes were then constructed with a periodic boundary condition. The lengths of each box were in the range of 30-35 Å. The densities of PLA, PGA, and TC at 298.15 K were set as 1.25 g cm⁻³ [73], 1.53 [74, 75] g cm⁻³, and 1.1821 g cm⁻³ [76], respectively. For the PLA/PGA materials, a blend structure was constructed instead of copolymers because χ calculations from these blend and copolymer systems showed nearly identical results. For PGA/TC and PLA/TC systems as well, a blend structure was constructed containing polymer chains and TC molecules. The details for the PLA/PGA blends of different compositions are summarized in Table 3.1 and the details for the blend systems of PLA/TC and PGA/TC considered in the present MD simulations are summarized in Table 3.2, respectively. When constructing the candidate blend structures, 100 independent configurations were initially built for each composition and five of them that showed the highest energetic stability (*i.e.*, lowest energy values after the geometry optimization) were selected for subsequent computations. The calculated results were obtained based on the MD computations from these five independent molecular configurations. Figure 3.1(b) contains some of examples of PLA/PGA, PLA/TC, and PGA/TC simulation boxes used in the work of this part.

Then energy minimization of each computation MD box was accomplished to eliminate the local non-equilibrium by geometry optimization. To further relax local hot-spots and achieve equilibrium, these structures proceeded to a 3-circle thermal anneal from 300 to 800 K. 15 ps MD simulation was conducted using NVT thermodynamic ensemble at each temperature. After the annealing, a 15 ps NVT MD simulation was conducted to render the temperature back to 300 K with a 100 K interval, then a 1000 ps NVT MD simulation was carried out at 298.15 K. At last, based on the 1000 ps NVT MD computations, the cohesive energy density (CED) for each system was calculated. Trajectories were saved

Table 3.1: PLA/PGA blend systems with various composition ratios considered in the present MD simulations.

PLA/PGA Compositions (wt%)	Number of LA units per chain	Number of GA units per chain	Numbers of chains per box	Density (g cm^{-3})	Box length (\AA)
0/100	–	50	13 PGA	1.530	34.5
10/90	50	50	1 PLA/11 PGA	1.502	34.1
20/80	50	50	2 PLA/10 PGA	1.474	34.5
30/70	50	50	3 PLA/9 PGA	1.446	34.9
40/60	50	50	4 PLA/7 PGA	1.418	34.5
50/50	50	50	5 PLA/6 PGA	1.390	34.9
60/40	50	50	5 PLA/4 PGA	1.360	33.1
70/30	50	50	6 PLA/3 PGA	1.334	33.6
80/20	50	50	7 PLA/2 PGA	1.302	34.1
90/10	50	50	7 PLA/1 PGA	1.278	33.2
100/0	50	–	8 PLA	1.250	33.8

Table 3.2: PLA/PGA blend systems with various composition ratios considered in the present MD simulations.

Compositions	Number of LA units per chain	Number of GA units per chain	Numbers of TC molecules and polymer chains per box	Density (g cm^{-3})	Box length (\AA)
Pure TC	–	–	58 TC	1.1821	34.0
PLA/TC (15 wt%)	50	–	7 PLA/9 TC	1.2401	34.1
PGA/TC (15 wt%)	–	50	10 PGA/11 TC	1.4768	33.8
PLA/TC (45 wt%)	50	–	4 PLA/25 TC	1.2192	33.1
PGA/TC (45 wt%)	–	50	6 PGA/30 TC	1.3728	33.8

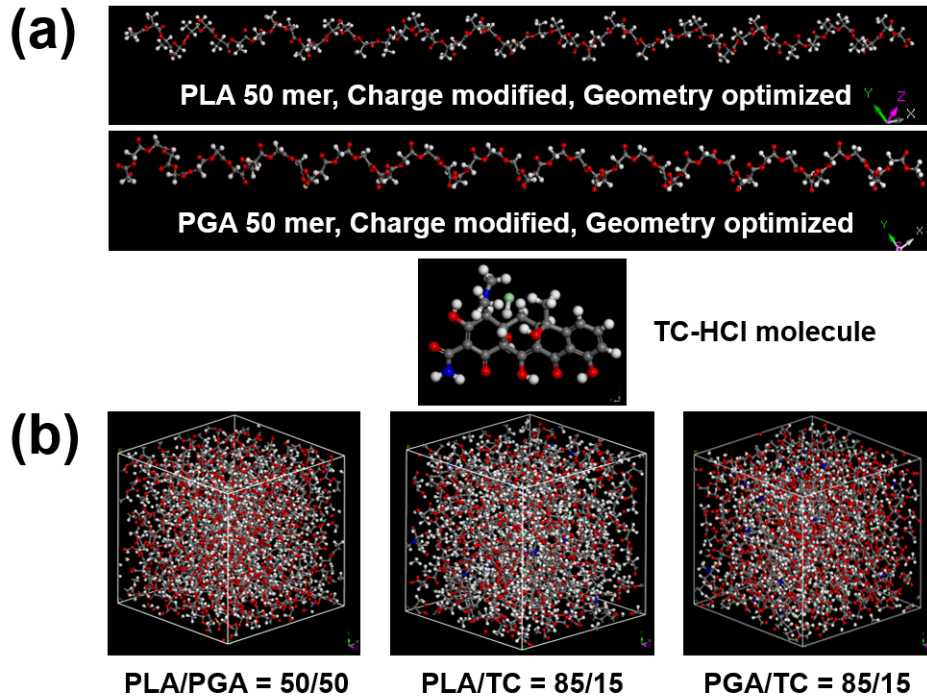


Figure 3.1: (a) Structures of PLA and PGA chains and TC molecules, and (b) examples of MD boxes to contain PLA/PGA, PLA/TC, and PGA/TC blends.

every 5 ps in the 1000 ps NVT procedure and the last 100 trajectories were applied for the estimation of CED and average χ . D_{self} of TC molecules were extracted from the 1000 ps NVT MD simulations using the mean square displacement (MSD) analysis. During the NVT simulations, the temperature of the computation domain was controlled by the Andersen ensemble. Throughout the MD simulations, the forcefield COMPASS II (condensed-phase optimized molecular potentials for atomistic simulation studies II) implemented in Materials Studio package was used for all of the computations of interatomic interactions [77, 78].

Phase-field modeling (PFM)

The phase-field method (PFM) predicated on a thermodynamic description of materials system provides an attractive route to predict the meso-scale structural evolution during processing/fabrication. PFM was originally developed to portray various evolution phenomena such as phase separation, diffusion, crystallization, and coarsening using a small set of

system-specific parameters in metallic systems [79]. This PFM can be applied to polymer-drug systems to describe the structural evolution that will eventually impact delivery kinetics of the prescribed system. PFM starts with by defining the bulk configurational free energy density, $f(\varphi_i)$, of a molecular system [80, 81].

$$f(\varphi_i) = RT \sum_i^n \frac{\varphi_i}{V_i^m} \ln \varphi_i + \frac{RT}{V^s} \sum_i^n \sum_{j,j>i}^n \chi_{ij} \varphi_i \varphi_j \quad (3.1)$$

where i iterates over all phase variables (*i.e.*, polymer, drug, and solvents), n is the total number of phases, φ_i and φ_j are the mole fractions of the system phase i and j , V_i^m is the molar volumes of the individual phases, V^s is the molar volume of solvents, χ_{ij} is the Flory-Huggins parameter between the system phases (i and j), R and T are the gas constant and the absolute temperature, respectively. While Equation 3.1 specifies the bulk contribution to the free energy of a system, the interfacial contribution resulted from distinct phase boundaries must be taken into consideration. PFM includes the interfacial contribution by introducing the gradient terms to a system by constructing the isothermal free energy, F , over the system volume V .

$$F = \int dV \left[f(\varphi_i) + \sum_i^n \frac{\varepsilon_i^2}{2} |\nabla \varphi_i|^2 \right] \quad (3.2)$$

where ε_i are the coupling parameters for the gradient terms. By adding the gradient terms in Equation 3.2, the system will have interfacial free energy that is proportional to ε_i . When the system of interest is assumed to be isothermal and incompressible, the temporal evolution of the concentration of individual phase variables can be governed by the following Cahn-Hilliard equation [82].

$$\frac{\partial \varphi_i}{\partial t} = \nabla \cdot M_i \nabla \frac{\delta F}{\delta \varphi_i} + \zeta_i \quad (3.3)$$

where M_i is the mobility and ζ_i is the “noise” (*i.e.*, Langevin fluctuation) of phase i , respectively. For a given polymer-drug system, the parameters in Equations 3.1-3.3, are typically

well-defined with the exception of χ_{ij} and M_i that depend on φ_i and/or φ_j . The coupling parameter, ε_i , can be a function of φ_i , however, since the interfacial properties are generally not well-established, $\varepsilon_i = \varepsilon$ (*i.e.*, constant) is a standard assumption [83]. The mobility, M_i , is typically represented as the product of diffusivity (D_i) and thermodynamic factor (*i.e.*, second derivatives of homogeneous energy density). In this work of multi-scale modeling, χ_{ij} and D_i parameters were quantified using the atomistic MD computation results.

3.2.2 Experimental section

A polymer-drug solution was prepared by dissolving TC (*i.e.*, TC-HCl, T7660, BioReagent; Sigma-Aldrich, Milwaukee, WI) and a PLGA M_w -50,000 g mol⁻¹ in tetrahydrofuran (THF, 401757, anhydrous, inhibitor-free; Sigma-Aldrich, Milwaukee, WI). PLGA with PLA/PGA=75/25 (P1941, PLGA75/25) and PLA/PGA=50/50 (739944, PLGA50/50) were obtained from Sigma-Aldrich, Inc. The ratios of PLGA and drug are 85 and 15 wt% and the final solution concentration containing a polymer and a drug of 1 % (w/v) was filtered (0.4 μ m). All solutions were stored in a cooler (ca. 5 °C) and used for film casting in 18 hours. Films were prepared by dropping 0.37 ml of PLGA-TC-THF solution at room temperature onto a 22 \times 22 mm² microscopic cover glass. Solvent was evaporated in a petri dish (diameter 6.5 in \times height 0.75 in) with a rate of about 75 mg h⁻¹. The petri dish was covered by porous Al foil to control the evaporation rate [69]. Before performing the atomic force microscopy (AFM) experiment, all films were placed under house vacuum at room temperature for 18 hours. Surface structures of coating were obtained using an AFM (model MFP 3D) in tapping mode with a silicone OMCL-AC240TS probe (spring constant 1-3 N m⁻¹). Multiple sections with the scan area of 10 \times 10 μ m² were used to measure the drug particle sizes.

This experiment was done by Donghun Koo from Sigma-Aldrich Inc., Milwaukee.

3.3 Results and discussion

3.3.1 MD computation

First, using MD simulations, we have calculated the cohesive energy densities (CED) and the solubility parameters (δ) of pure PLA, PGA, and TC materials. CED is the energy required to completely remove the unit volume of molecules from their amorphous bulk state to infinite separation. δ is typically estimated by $\delta = \sqrt{\text{CED}}$ and is one of the principal quantities for prediction of blend miscibility [84, 85]. When the δ values of two pure substances are similar, it is generally anticipated that the blend systems are miscible. δ values of pure PLA, PGA, and TC at 298.15 K predicted by MD simulation are given in Table 3.3. Each δ is an average value derived from 5 independent simulations. Table 3.4 lists the δ values of individual polymers obtained by other methods [86, 87, 88]. The predicted δ value for the pure PLA at 298.15 K in this work is 20.51 (J cm⁻³)^{0.5}, consistent with the previous data ranging from 17.64 to 21.73 (J cm⁻³)^{0.5} in Table 3.4. In general, the δ value of PLA is smaller than that of PGA because PGA has higher attractive interactions compared to PLA, as shown in Tables 3.3 and 3.4. The δ value of PGA in the previous literatures varies from 19.24 to 27.11 (J cm⁻³)^{0.5}, and our results (26.84 (J cm⁻³)^{0.5}) are closer to the high end of the prior data set. This dictates that the current MD calculation shows a fairly consistent result for the δ values of PLA and PGA compared with the previous findings, which manifests that the MD procedures employed in the current work could be applied to quantify the Flory-Huggins parameters (χ) for various compositional PLGA-TC systems within a tolerable error range. Note that δ of TC (*i.e.*, TC-HCl) is currently not available from previous experiments and/or computations.

As a first approximation, if $(\delta_A - \delta_B)^2$ (where δ_A and δ_B are the Hildebrand solubility parameters of polymers A and B, respectively) is smaller than 4 J/cm³, the two polymers may be treated as miscible [85]. With this, it is thought that pure PLA ($\delta=20.51$ (J cm⁻³)^{0.5}) and pure PGA ($\delta=26.84$ (J cm⁻³)^{0.5}) would not be miscible. This simple approximation agrees

Table 3.3: Solubility parameter (δ) values of PLA, PGA, and TC predicted by simulation at 298.15 K.

System	Number of repeat unit per polymer chain	Number of polymer or drug molecules per box	Molecular mass (g mol ⁻¹)	Density (g cm ⁻³)	Box length (Å)	Solubility parameter (J cm ⁻³) ^{0.5}
PLA	50	8 PLA	3621.16	1.250 [73]	33.8	20.51
PGA	50	13 PGA	2919.81	1.530 [74, 75]	34.5	26.84
TC	–	58 TC	480.901	1.1821 [76]	34.0	21.61

Table 3.4: Solubility parameter (δ) values of PLA and PGA estimated using different experimental and theoretical approaches at 298.15 K.

Polymer	Method	Solubility parameter (J cm ⁻³) ^{0.5}	Ref.
PLA	Van Krevelen group contribution	17.64	[86]
	Intrinsic 1D viscosity	19.16	
	Intrinsic 3D viscosity	19.28	
	Classical 3D geometric	19.53	
	Fedors group contribution	21.42	
	Optimization	21.73	
	Hoflyzer-van Krevelen group contribution	21.4	[87]
PGA	Hoy group contribution	21.3	
	Van Krevelen group contribution	19.24	[86]
	Fedors group contribution	23.82	
	Hoflyzer-van Krevelen group contribution	24.7	[87]
	Hoy group contribution	24.2	
	Molecular simulations	27.11	[88]

with the conclusion based upon the critical χ argument that will be discussed later. TC has a δ value of $21.61 \text{ (J cm}^{-3}\text{)}^{0.5}$, similar to the value of PLA compared with that of PGA. However, it would not be accurate to conclude that PLA and TC are more miscible because the above criterion of miscibility regarding Hildebrand solubility parameter is only useful for judging nonpolar and slightly polar systems without hydrogen bonding [84, 89]; although PLA is nonpolar, PGA and TC are polar [90, 91]. In addition, the above criterion does not include the impacts of compositional variations in the blends or copolymer systems. Rather, the Flory-Huggins lattice theory is a widely accepted approach to quantify the interactions and subsequent mixing behavior of polymeric systems [80, 81, 91, 92, 93]. Such Flory-Huggins lattice theory has been documented and considered as an excellent starting point to understand and describe not only the mixing between a large M_w component and a small M_w component, but also the mixing between two types of polymers. The Flory-Huggins parameter, χ , is commonly used as a criterion of miscibility. For a binary mixture, χ can be evaluated by [84],

$$\chi = \left(\frac{\Delta E_{\text{mix}}}{RT} \right) V_{\text{mono}} \quad (3.4)$$

where V_{mono} is the average molar volume of the repeat units of PLA and PGA for PLA/PGA blends. If one of the two components represents a drug, then V_{mono} can be approximated as the molar volume of the drug molecule because the molar volume of drug is typically much smaller than the molar volume of entire polymer chains [94, 95]. When A and B phases are mixed, the energy of mixing, ΔE_{mix} , of the mixed system can be estimated by [84, 96],

$$\Delta E_{\text{mix}} = \phi_A \left(\frac{E_{\text{coh}}}{V} \right)_A + \phi_B \left(\frac{E_{\text{coh}}}{V} \right)_B - \left(\frac{E_{\text{coh}}}{V} \right)_{\text{mix}} \quad (3.5)$$

where ϕ_A and ϕ_B are the volume fractions of polymers A and B, respectively, therefore, $\phi_A + \phi_B = 1$. Here, $\left(\frac{E_{\text{coh}}}{V} \right)_A$, $\left(\frac{E_{\text{coh}}}{V} \right)_B$, and $\left(\frac{E_{\text{coh}}}{V} \right)_{\text{mix}}$ denote the CEDs for pure A, pure B and mixture, respectively. CED (or $\left(\frac{E_{\text{coh}}}{V} \right)$) characterizes the strength of attractive interactions.

Table 3.5: χ values of PLA/PGA blend systems with various composition ratios considered in the present MD simulations.

PLA/PGA Compositions	CED_{PLA} (J cm ⁻³)	CED_{PGA} (J cm ⁻³)	CED_{mix} (J cm ⁻³)	Average χ
0/100	–	720.3618294	–	–
10/90	420.6942980	720.3618294	688.2377408	0.1151047
20/80	420.6942980	720.3618294	654.9688151	0.2606612
30/70	420.6942980	720.3618294	624.0830464	0.3762202
40/60	420.6942980	720.3618294	589.4487977	0.4078942
50/50	420.6942980	720.3618294	563.3699066	0.4016148
60/40	420.6942980	720.3618294	533.0482740	0.4191711
70/30	420.6942980	720.3618294	506.0738416	0.3040633
80/20	420.6942980	720.3618294	472.7963386	0.3151782
90/10	420.6942980	720.3618294	446.8240800	0.2539610
100/0	420.6942980	–	–	–

By combining $\delta = \sqrt{CED}$ and Eqs. 3.4 and 3.5, ΔE_{mix} and χ for a mixture can be calculated as long as the CED values for constituent phases are known.

Table 3.5 summarizes the calculated χ values for the PLA/PGA systems with various composition ratios. All of the calculated χ values are the positive values indicating that the blending of PLA and PGA polymers would not follow the ideal mixing behavior. Rather, it is expected that the PLA and PGA molecules would exhibit repulsive interactions to a certain degree. These computational results are also displayed in Figure 3.1(a) using black square symbols. In the figure, the error bar represents the standard deviations from 5 independent simulations. For a mixture of two polymer components, the critical Flory-Huggins parameter ($\chi_{critical}$) can be generally estimated by [84],

$$\chi_{critical} = \frac{1}{2} \left(\frac{1}{\sqrt{n_A}} + \frac{1}{\sqrt{n_B}} \right)^2 \quad (3.6)$$

where n_A and n_B represent the number of repeat units of A and B polymer chains, respectively. If B represents a drug, then n_A and n_B represent the number of chain segments of the polymer molecules and the number of the drug molecules, respectively, as a chain segment should have the identical volume as a drug molecule according to the Flory-Huggins lattice

theory.

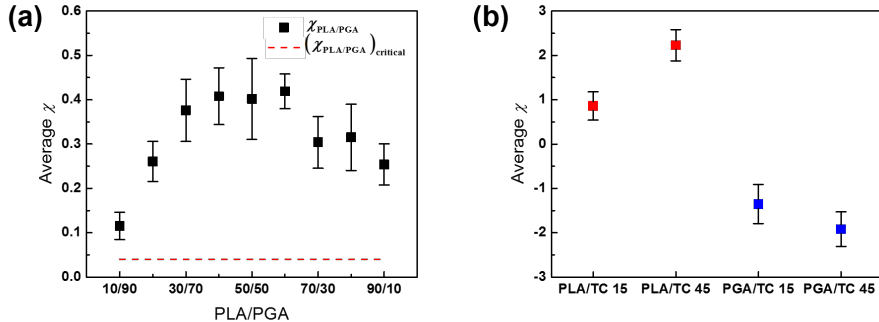


Figure 3.2: Plots to show the calculated χ values in the blend systems of (a) PLA/PGA and (b) PLA/TC and PGA/TC. In Figure 3.2(b), numerical suffixes indicate the weight % of TC in the blend.

Polymer blends are miscible if $\chi_{AB} < \chi_{critical}$ where χ_{AB} is the Flory-Huggins parameter of A and B polymers; if χ_{AB} is considerably greater than the critical value, then blends are immiscible. If χ_{AB} is somewhat greater than $\chi_{critical}$, the blends are partially miscible [84, 92]. For the PLA/PGA systems considered in this work, $n_{PLA} = n_{PGA} = 50$ and $(\chi_{PLA/PGA})_{critical} = 0.04$. It is indicated as the red dashed line in Figure 3.2(a). As shown in Figure 3.2(a), average χ values for PLA/PGA systems of entire compositions are all larger than $(\chi_{PLA/PGA})_{critical}$, thus PLA and PGA are thought to be immiscible or partially miscible. PLA/PGA 10/90 exhibits the best compatibility while PLA/PGA 60/40 possesses the lowest compatibility. As the proportion of PLA increases from PLA/PGA 10/90 to PLA/PGA 40/60 in the blends, average χ increases gradually, and, as the proportion of PLA increases from PLA/PGA 60/40 to PLA/PGA 90/10 in the blends, average χ decreases gradually. The average χ of PLA/PGA 50/50 is slightly lower than those of PLA/PGA 40/60 and PLA/PGA 60/40 with a relatively larger standard deviation, but it is still higher than those of other compositions.

In Figures 3.3 and 3.4, we show the radial distribution function (RDF), $g(r)$, of carbon atoms of PLA and PGA polymers, respectively, in the pure and blend systems. For statistical relevancy, these data were obtained from the averages of 3 independent MD simulation sets.

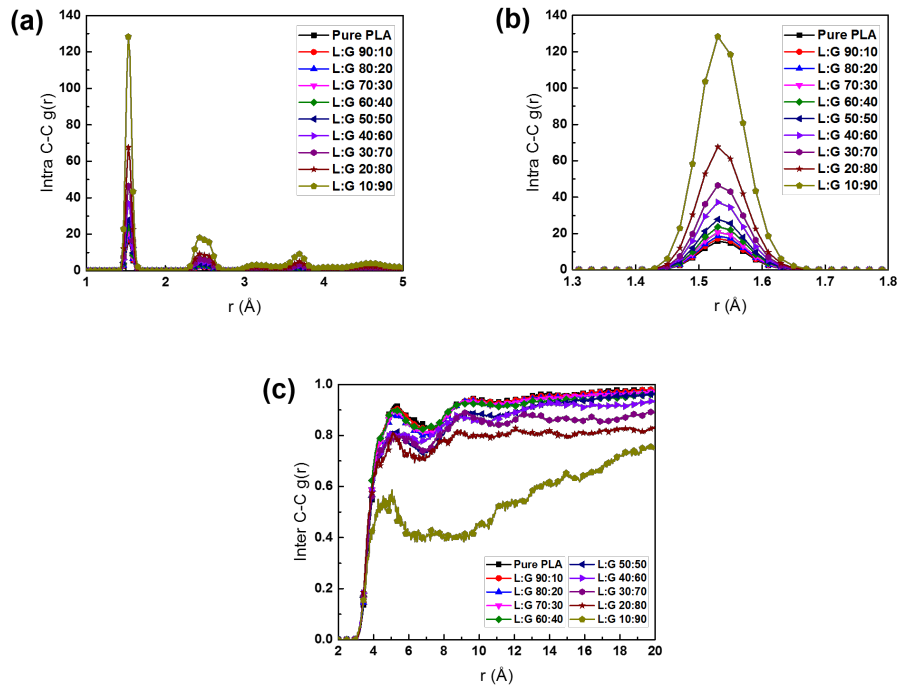


Figure 3.3: Plots to show the calculated RDF values of (a) intramolecular carbon atoms, (b) first peaks of intramolecular carbon atoms, and (c) intermolecular carbon atoms of PLA in pure PLA and PLA/PGA blend systems.

This RDF represents the probability of finding a pair of atoms at a given distance (r) with reference to bulk materials with random distribution. Therefore, the analysis of $g(r)$ will quantitatively capture the atomistic interactions of the given polymer chains. Figure 3.3(a) and (c) provide $g(r)$ of the intra- and intermolecular carbon atoms, respectively, of PLA. From Figure 3.3(a), it is clear that the highest peak of intramolecular $g(r)$ at ca. 1.54 Å that comes from the single bond connectivity decreases as the PLA/PGA ratio increases. This is because, although the overall density of PLGA blends decreases, the bulk density of PLA itself in the blends increases with increasing PLA/PGA ratio; the peak values are approximately inversely proportional to the PLA/PGA ratio. For clarity, Figure 3.3(b) presents an enlarged view for these intramolecular $g(r)$ profiles of the highest peak with varying PLA/PGA ratios. On the other hand, $g(r)$ plots of intermolecular carbon atoms of PLA in Figure 3.3(c) show that the interactions of different PLA polymer chains increase with increasing PLA/PGA ratio, as the bulk density of PLA itself in the blends increases

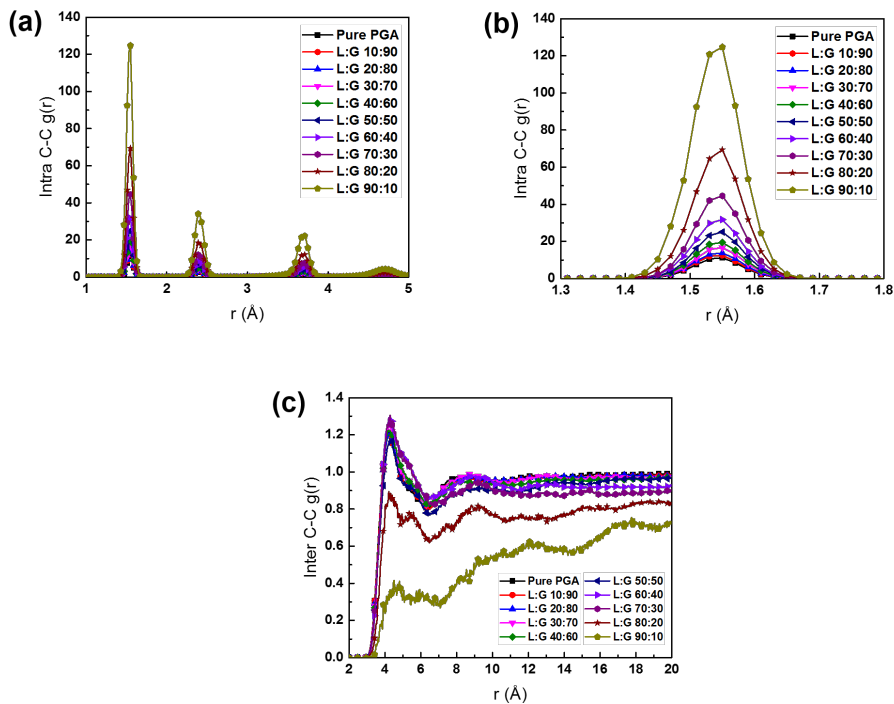


Figure 3.4: Plots to show the calculated RDF values of (a) intramolecular carbon atoms, (b) first peaks of intramolecular carbon atoms, and (c) intermolecular carbon atoms of PGA in pure PGA and PLA/PGA blend systems.

with adding more PLA chains. These intermolecular RDF profiles asymptotically approach to 1, as the intermolecular C–C interactions would exhibit the behavior of random structure with increasing the r values. The $g(r)$ profiles from PGA polymers presented in Figure 3.4 show the same trend for the intra- and intermolecular carbon atom distributions; as the PLA/PGA ratio increases, the intra- and intermolecular interactions are increased and decreased, respectively.

Table 3.6 lists the calculated χ values of PLA/TC and PGA/TC blend systems considered in the present MD simulations. The χ values of PGA/TC are negative for the 15 and 45 TC wt% compositions, therefore, it is thought that PGA would have a good miscibility with TC. On the other hand, the χ values of PLA/TC are both positive implying that PLA has a relatively poor miscibility with TC. The reason for this is probably the hydrophobicity difference [89]. TC is a hydrophilic drug and it is more miscible with PGA than PLA

Table 3.6: χ values of PLA/TC and PGA/TC blend systems considered in the present MD simulations. The unit of CED is J cm^{-3} .

Compositions	$\text{CED}_{polymer}$	CED_{TC}	CED_{mix}	Average χ	Standard deviation of χ
Pure TC	–	467.0002786	–	–	–
PLA/TC (15 wt%)	420.6942980	467.0002786	422.5442044	0.8587370	0.3194255
PGA/TC (15 wt%)	720.3618294	467.0002786	680.4904683	-1.3549031	0.4417830
PLA/TC (45 wt%)	420.6942980	467.0002786	428.7448620	2.2310665	0.3521467
PGA/TC (45 wt%)	720.3618294	467.0002786	601.3487279	-1.9211784	0.3901504

because PGA is relatively more hydrophilic than PLA due to lack of asymmetrical methyl groups (*i.e.*, hydrophobicity: $\text{TC} < \text{PGA} < \text{PLA}$) [58, 97]. These results are illustrated using a scatter plot in Figure 3.2(b). As shown in Figure 3.2(b), PLA/TC (45 wt%) has a higher χ value than PLA/TC (15 wt%). Hence, increasing PLA content in the blend would decrease the miscibility of TC, whereas for PGA/TC, increasing PGA content in the blend system would decrease the miscibility of TC; the results provided in Figure 3.2(b) show the sequence of χ values, *i.e.*, $\text{PLA/TC } 45 > \text{PLA/TC } 15 > \text{PGA/TC } 15 > \text{PGA/TC } 45$. In Figure 3.5, we show $g(r)$ of (a) intramolecular and (b) intermolecular carbon atoms from PLA (red) and PGA (blue) materials with 15 % (square symbols) and 45 % (circular symbols) TC, respectively. Here, the $g(r)$ functions were obtained from the PLA or PGA chains in the MD computation domain. The general trend found in the PLA/PGA systems is again observed in the PLA/TC and PGA/TC materials. When $g(r)$ profiles from PLA and PGA are compared for the intramolecular interactions, the peak positions are nearly identical, located at ca. 1.54 \AA , however, the peak values from PLA are much higher than those from PGA because of higher bulk density of PGA. In addition, it is clear that, as the relative polymer contents are decreased, the peak value of $g(r)$ is increased, which can be again explained by the relative density change argument. From Figure 3.5(b), it is also clearly seen that the degrees of intermolecular interactions between different PLA and PGA chains are decreased by adding more TC molecules in the blend system.

In Figure 3.6, we summarize the results of calculated self-diffusivity, D_{self} , of TC molecules

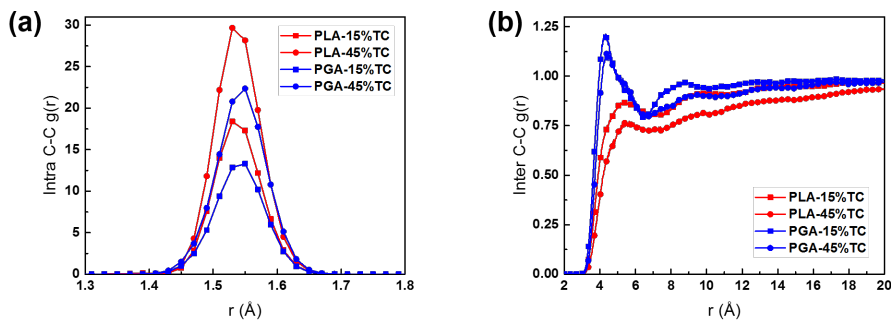


Figure 3.5: Plots to show the calculated RDF values of (a) intramolecular carbon atoms and (b) intermolecular carbon atoms of polymers in the TC/polymer blend systems.

in the PLA and PGA polymers. D_{self} was estimated based on the mean square displacement (MSD) analysis as a function of MD computation time. The data reported in Figure 3.6 are averages of at least 50 TC molecules from MD simulation box. In the figure, the error bars represent the standard deviations. From the results, it is seen that D_{self} of TC in PLA are approximately one order higher with larger standard deviations than those of TC in PGA because of lower affinity between TC molecules and PLA chains. Therefore, under absence of solvents, it is expected that the transport of TC molecules would be easier in the PLA system. However, for an adequate thermodynamic/kinetic description for the evolution of microstructures for a polymer-drug-solvent system, ternary diffusivities over entire composition ranges are required, which presents a formidable challenge.

3.3.2 Experimental film surface characterization

In Figure 3.7(a) and (b), the examples of the surface morphologies obtained from AFM scans ($10 \times 10 \mu\text{m}^2$) for 50/50 and 75/25 (PLA/PGA) PLGA films are provided. The TC contents was 15 wt% for these specimens. As expected from the χ value calculation results for the PLA/TC and PGA/TC materials, the surface morphology clearly portrays a phase-separated structure consists of drug particles (bright contrast) and PLGA matrix (dark contrast). The fraction of TC drugs on the film surface is much higher than its actual wt% (ca. 15 wt%) because the nucleation of drug particles will be initiated near the surface

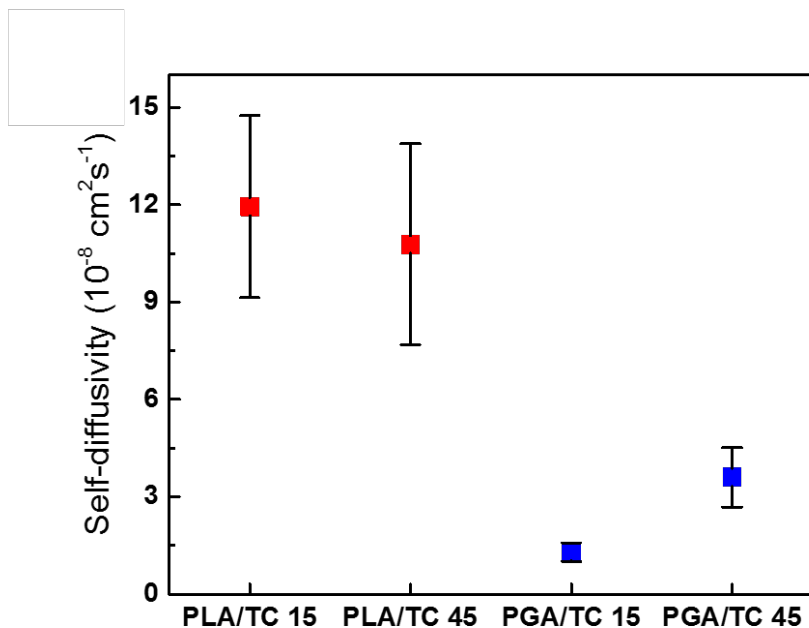


Figure 3.6: Plot of self-diffusivities (D_{self}) of TC in PLA/TC and PGA/TC systems.

of the sample as the solvent evaporation proceeds. Also, it is evident from the figures that the drug particle size in 50/50 PLGA film is much larger than that in 75/25 film. To more quantitatively elucidate the composition ratio effect on the drug size distribution, the average radii of the drug particles were evaluated by measuring the major- and minor-axis of the drug particles for each section. Here, we assumed that the drug particles take the form of ellipsoids. The average radii of the particle were obtained by equating the areas of a perfect circle with the average radius and ellipsoids with measured major- and minor-axis. Based on the analysis of more than ca. 60 drug particles from each film, the average drug particle radii were calculated as $1.05 \pm 0.17 \mu\text{m}$ and $0.68 \pm 0.10 \mu\text{m}$ for the 50/50 and 75/25 samples, respectively. In Figure 3.7(c) and (d), the histograms to show the normalized frequency of the drug particle radius are displayed. From the figures, it is seen that about 30 % and 35 % of the total population are in the ranges of 1.0-1.1 μm and 0.6-0.7 μm for the PLGA 50/50 and the PLGA 75/25 coatings, respectively. Such drug particle size in the polymer matrix can impact the drug release kinetics [64]. It is generally accepted that the drugs with

smaller particles are relatively easier to dissolve while the drugs with larger particle sizes will dissolve less readily.

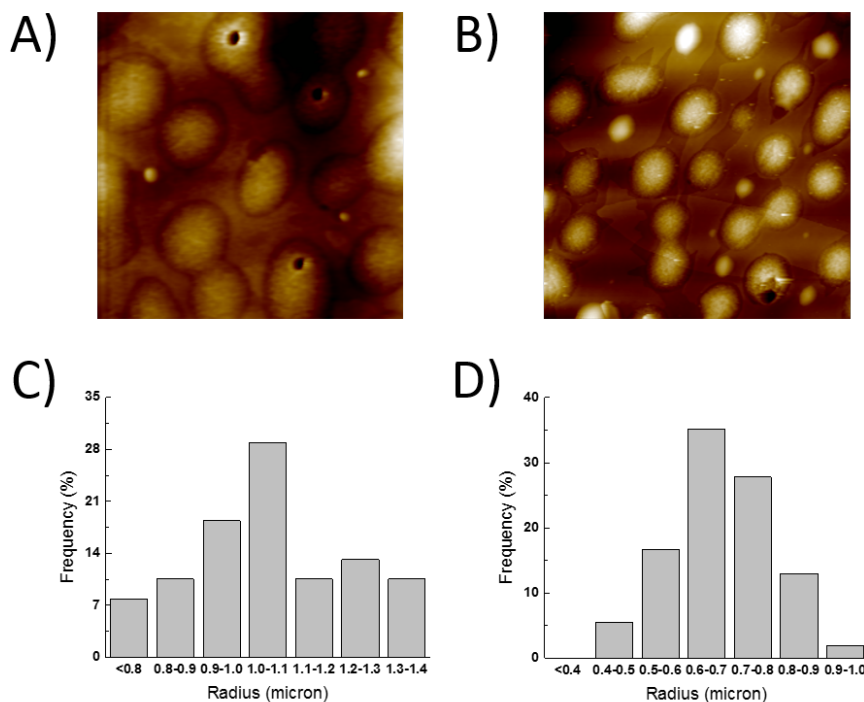


Figure 3.7: Examples of AFM scans from (a) PLGA50/50-TC and (b) PLGA75/25-TC films, and drug size distributions from (c) PLGA50/50-TC and (d) PLGA75/25-TC films.

3.3.3 Free energy density calculation and meso-scale simulation

To further examine the mixing behaviors of PLGA-TC, the free energy of change of mixing for these materials was analytically evaluated. As introduced in the previous ‘Phase-field modeling (PFM)’ section, in the Flory-Huggins solution model, the bulk homogeneous free energy density (f) for a system with arbitrary number (n) of constituent components can be described by Equation 3.1 [80, 81]. When the interfacial energies between the polymer and drug phases are relatively smaller than the bulk energies, f could be a direct measure for the spontaneity of mixing. To quantify the bulk free energy densities, we assumed that the PLA, PGA, and TC molecules are completely dissolvable in the THF solvent, and the molar volumes of PLA, PGA, TC, and THF are 40000, 32680, 407, and 81 cm³ mol⁻¹, respectively;

we used M_w ca. 50,000 g mol⁻¹ for PLA and PGA materials and molecular mass of 480.901 g mol⁻¹ for TC based on the MD calculations. Because we assumed that the polymers and TC drugs are completely miscible in the THF solvent, the Flory-Huggins parameters, χ , between the solute (*i.e.*, PLA, PGA, or TC) and the solvent (*i.e.*, THF) can be estimated by,

$$\chi = \frac{V^s(\delta_{solute} - \delta_{solvent})^2}{RT} \quad (3.7)$$

where δ_{solute} and $\delta_{solvent}$ are the Hildebrand solubility parameters of the solute and solvent, respectively, and V^s is the molar volume of the solvent. With this, Figure 3.8 shows the free energy density variations for the PLA/TC and PGA/TC systems of different solvent fractions. From the figure, it is seen that when THF solvents start to evaporate, the free energy density of PGA/TC is rather higher than that of PLA/TC primarily due to the large difference between the χ values of PGA and TC. However, in the final stage of film casting when the solvent fraction decreases by evaporation, the free energy density of mixing in PLA and TC phases becomes much higher than those in PGA and TC phases, which will thermodynamically prevent the mixing of PLA and TC materials. In particular, when the TC wt% is large (*i.e.*, 45 wt%, green symbols in Figure 3.8), it is predicted that the free energy density of PLA and TC would show a high positive value. The drug morphologies shown in Figure 3.7 can also be explained by the results of the free energy density plot in Figure 3.8. As the THF solvents evaporate, the diffusion of drug molecules in the higher PLA composition would be easier, which can retard the nucleation of TC drug particles. If the nucleation of TC drug is slowed down, the actual drug precipitates will be formed later in the evaporation process, and the number and the size of drug particles will be larger and smaller, respectively, as shown in the surface morphology of PLGA 75/25 film samples in Figure 3.7(b). However, it should be noted that, the nucleation and the growth kinetics of these TC particles will also be influenced by the interface energies of PLA/TC and PGA/TC and the diffusion rates of TC molecules through the polymers/solvents. Further, the diffusion

of TC molecules would be highly dependent on the evaporation rates of the THF solvents. Generally, when the solvent evaporation rate is fast, the drug particle morphology of the film surface will be similar to the one shown in Figure 3.7(b), *i.e.*, smaller in size and larger in the number of particles.

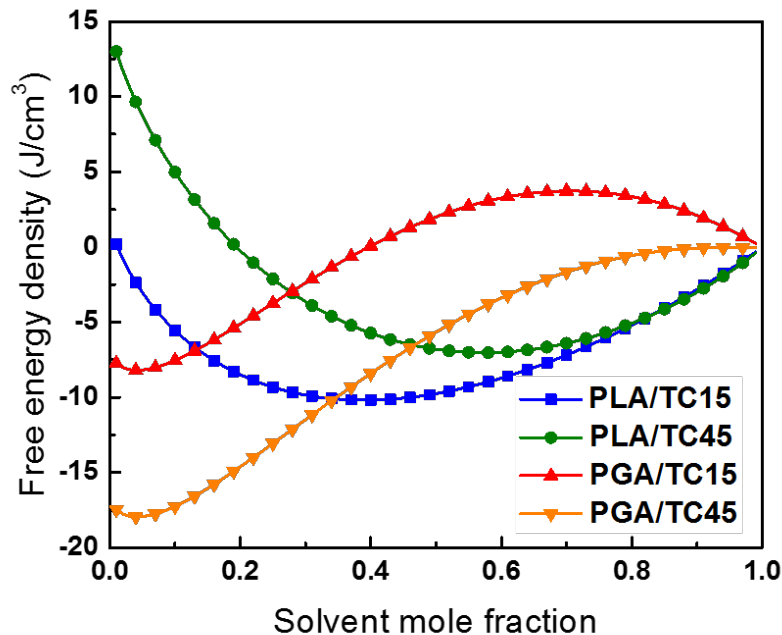


Figure 3.8: Plot of free energy densities using the Flory-Huggins solution model for PLA/TC and PGA/TC systems.

For meso-scale simulations for the structural evolution of polymer-drug coatings, we tested the two different systems shown in Figure 3.7, *i.e.*, PLGA50/50-TC and PLGA75/25-TC. As the structural evolution simulation requires inclusion of the solvent materials, *i.e.*, THF, in the computational domain, a quaternary system consists of PLA, PGA, TC, and THF should be considered. In the current work, however, for simplicity, we treated single polymer phase with different material properties for PLGA50/50 and PLGA75/25 materials. The corresponding material properties of PLGA were weight-averaged by their corresponding PLA/PGA ratios. The molar volumes of PLGA50/50 and PLGA75/25 were 36340 and 38170 $\text{cm}^3 \text{mol}^{-1}$, and the χ values of PLGA50/50 and PLGA75/25 were 0.4016 and 0.3096,

respectively. The χ values for each phase were assigned using the concurrent MD simulation results presented in Table 3.6 and Figure 3.2. The interfacial energies were set to 15, 5, 10 mJ m⁻² for PLGA-TC, TC-THF, and PLGA-THF interfaces, respectively [83, 98]. The mobility, M_i , in Equation 3.3 is typically represented as the product of diffusivity (D_i) and thermodynamic factor (second derivatives of homogeneous energy density). Diffusivities for PLGA and TC were set to 1×10^{-12} and 5×10^{-7} cm² s⁻¹ for the characteristic system considered here. The diffusivity of TC molecule is based on the MD computation results given in Figure 3.6. Note that, for a film-based (*i.e.*, coating) drug delivery system processed using casting, the diffusivities of polymer and drug molecules are majorly determined by the contents of solvents [64, 70, 83, 98]. To incorporate the effect of local amount of solvent on the diffusivities, they were incrementally reduced to 10^{-3} and 10^{-1} of original diffusivity value for PLGA and TC phases, respectively, as the local solvent concentration decreases from 20 vol% to 0 vol% [70, 98]. The thermal fluctuation term of Equation 3.3, ζ_i , was ignored because all of the constituent phases are amorphous. With these material properties, all simulations were started by a homogeneous initial system that is composed of solvent (70 vol% solvent) with dissolved drug and polymer. Here, we assumed that no significant structural evolution would occur in the solvent concentration range of 70 to 99 vol%. As mentioned, two distinct homogeneous systems with different copolymer ratios (*i.e.*, PLGA50/50 and PLGA 75/25) with polymer/drug ratio of 80/20 were initiated. Although the polymer/drug ratio of 85/15 w/v was used in the experimental fabrication of PLGA-TC coatings, 80/20 v/v PLGA/TC was used in the PFM simulation to capture the high propensity of drug particle formation and/or segregation near the evaporating surface, as explained before. The meso-scale PFM computations were conducted on a 2D 500 \times 100 rectangular grid space with no flux boundary conditions, and final microstructure was obtained when 1 vol% solvent remained in the system. In this rectangular grid space, the solvent was intentionally removed from the surface of coating so that the volume fraction of solvent continuously decreases with processing time. The rate of solvent removal

(evaporation) is assumed to be proportional to the average solvent concentration of surface.

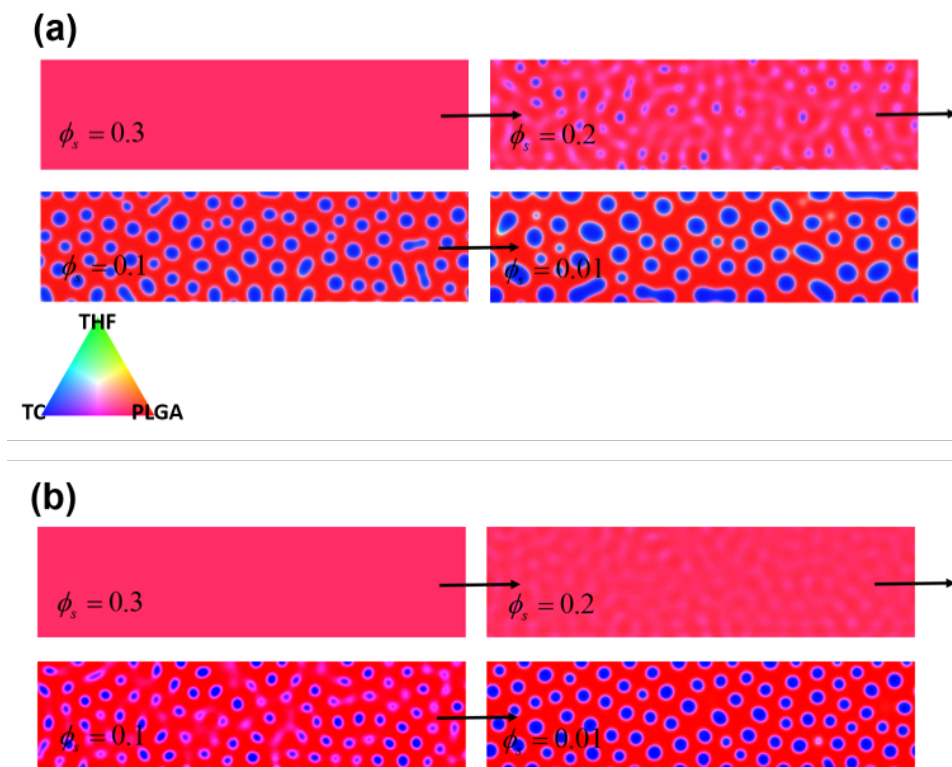


Figure 3.9: Microstructural evolution predicted using phase-field method for (a) PLGA50/50-TC and (b) PLGA75/25-TC systems. ϕ_s represents the solvent volume fraction.

In Figure 3.9, we show the microstructural evolution of PLGA-TC surfaces predicted from PFM computations for (a) PLGA50/50 and (b) PLGA75/25. In the figure, ϕ_s represents the THF solvent volume fraction. The ternary triangular legend was used to indicate the individual concentrations of PLGA (red), TC (blue), and THF (green) phases. With adequate scaling, the dimension of the computational domain was calculated as approximately $50 \times 10 \mu\text{m}^2$. As clearly depicted in the structural morphologies in Figure 3.9, changing the PLA/PGA composition ratios can have a strong impact on the development of coating microstructures, which is qualitatively consistent with the experimental observations shown in Figure 3.7. The final drug particle size is much larger and the drug particle number is smaller in PLGA50/50-TC compared with those in PLGA75/25-TC. Also, it is seen that the onset of drug particle formation occurs after more solvent has been removed when PLA/PGA ratio

is higher. The differences in the structural development during coating fabrication majorly comes from the Flory-Huggins parameters between PLA-TC and PGA-TC. Note that, as mentioned earlier, the final structure of these films could be influenced by other factors such as the solvent evaporation rates, contents of additives, etc. However, it is thought that the quantitative understanding between the Flory-Huggins parameters and the resultant underlying structures of PLGA-TC coatings obtained in this work can be usefully applied for the design of drug delivery systems.

3.4 Conclusions

A series of MD computations has been performed to evaluate the Flory-Huggins parameters (χ) between TC drugs and PLA/PGA polymers. By quantifying χ values between PLA and PGA blend systems, it is shown that mixing of PLA and PGA polymers is not thermodynamically favorable throughout the entire composition range of 10/90 to 90/10 wt% PLA/PGA. The χ parameters between PLA and/or PGA polymers and TC drugs were estimated for the TC compositions of 15 and 45 wt%. Based on the thermodynamics considerations using the Flory-Huggins solution model, the free energy densities for these PLA/TC and PGA/TC systems were correlated to the surface structural morphology of PLGA/TC films. The meso-scale modeling based on PFM method using the material properties obtained through MD computations revealed that the overall size distributions of drug particles embedded in PLGA matrices with different PLA/PGA copolymer ratios are comparable to the experimental observations. Such variations of drug particle sizes can directly influence the drug release kinetics from PLGA-TC coatings.

Chapter 4

Polymeric binders: a case for Li–S batteries

4.1 Introduction

4.1.1 General introduction to Li–S batteries

Countries around the world are working on mitigating the profound negative impacts of gas and diesel automobiles on the sustainability of our environment, resources and economy [99]. This marks a crescendo of demand for batteries with large capacity in favor of electric or hybrid vehicles (EVs or HVs). The state-of-art lithium–ion (Li–ion) technology has certainly attracted great attention in this field due to its high energy densities (110~700 Wh L⁻¹) and high specific power (up to 300 W kg⁻¹) [100, 101]. Specifically, Li–ion batteries have been successfully applied to power modern commercial Tesla Model S [102] and Model X [103] as well as Nissan LEAF [104] EVs, and the two models of Tesla allow a mile range of 348~402 and 305~351, respectively, which are almost the highest in EV market. While the Li–ion technology is getting mature, it slowly reaches the performance limits, which are ca. 830 Wh L⁻¹ and ca. 330 Wh kg⁻¹ in terms of energy density and specific energy, respectively [100].

As a promising candidate battery system to be applied in EVs and HVs, rapidly growing attention has been paid to lithium–sulfur (Li–S) batteries since last decade. Due to the nature of the active materials of the electrodes, Li–S batteries have been expected to succeed Li–ion cells in terms of larger specific energy at a reduced cost [105], which realistically means an extended mile range at a cheaper price for EVs. Unlike the Li–ion batteries using Li–intercalation compounds (e.g. transition metal oxides) as anode materials, typical Li–S cells employ metallic lithium as the active material in anode, which means that more energy can be provided per unit weight of its anode. Together with a sulfur cathode partner, a Li–S cell can discharge at the voltage of ca. 2.15 V [106], relatively lower than the ca. 3.7 V [107] of Li–ion batteries. But the theoretical specific energy of Li–S battery systems is ca. 2700 Wh kg⁻¹, which is nearly five times higher than that of Li–ion batteries (see Table 4.1 [100, 108, 109, 110, 111, 112]). This is because sulfur can provide very high theoretical specific capacity of 1675 mAh g⁻¹ based on its moderate molecular weight and the fact that each sulfur atom can accept two electrons when being reduced thoroughly. Moreover, the abundance, extremely low cost and non-toxicity of sulfur are favorable to drastically decrease the final cost of Li–S batteries. The price of Li–S battery packs could be less than 150 USD kWh⁻¹, while that of Li–ion battery packs could be 600 USD kWh⁻¹ [108]. Although the increasing market of EVs and HVs seems to be the strongest motivation for developing Li–S technology, note that this technology is also expected to be applied in aircrafts, large-scale energy storages and other fields which need large amount of energy and to fulfill light weight meanwhile.

Table 4.1: Comparison of specific energy and energy density between Li–S and Li–ion batteries.

Battery type		Specific energy (Wh kg ⁻¹)	Energy density (Wh L ⁻¹)
Li–S	Theoretical	2700	2600
	Today	90~471	90~300
	Target for 2020	500	550
Li–ion	Theoretical	580	1800
	Today	50~300	110~700
	Practical limits	330	830

A significant progress has been made for Li–S technology during last decade (see Table 4.1). Currently the Li–S battery company OXIS Energy in UK offers the Li–S pouch cells with specific energies up to 425 Wh kg⁻¹ for aerospace and automotive, significantly better than most Li–ion batteries, which are in the range of 150 to 250 Wh kg⁻¹, and a stunning 500 Wh kg⁻¹ is on target by the end of 2020. For the near future, practical specific energy values on the order of 600 Wh kg⁻¹ are expected with solid state lithium–sulfur technology.

However, the Li–S technology still suffers from several unresolved issues, which induces a gap between expectation and reality, and impede complete transfer of this technology to commercial market. Next subsection briefly presents the basic working mechanism of Li–S batteries, along with its sulfur cathode issues.

4.1.2 Working mechanism and cathode issues of Li–S batteries

A conventional Li–S battery consists of a sulfur-based cathode and a metallic lithium anode, which are separated by a polymeric separator soaked with a liquid organic electrolyte. As it is shown in Figure 4.1 [113], the cathode has sulfur as its active material. However, bare sulfur has a low conductivity of ca. 10⁻¹⁶ S cm⁻¹ at room temperature [113]. Therefore, the discharge/charge rate of Li–S batteries has been limited. To improve the conductivity of cathode, a conductive carbon additive, such as carbon black, is always mixed with sulfur powder. To keep the integrity of the composite and provide enough contact between the composite and the current collector, poly(vinylidene difluoride) (PVDF) or poly(ethylene oxide) (PEO) is typically added in the cathode as a binder. As a result of the additive and the binder, the battery capacity dependent on the load of sulfur is sacrificed. Usually, the weight ratio of sulfur, carbon additive and binder are 70~80 wt%, 10~15 wt% and 10~15 wt%, respectively, as illustrated in Figure 4.1.

Besides the above-mentioned two limitations, the so-called “shuttle effect” [114] is one of the main problems of Li–S battery systems, which is caused by a phenomenon that active materials (*i.e.*, the intermediates of the electrochemical reaction, polysulfide species, such as

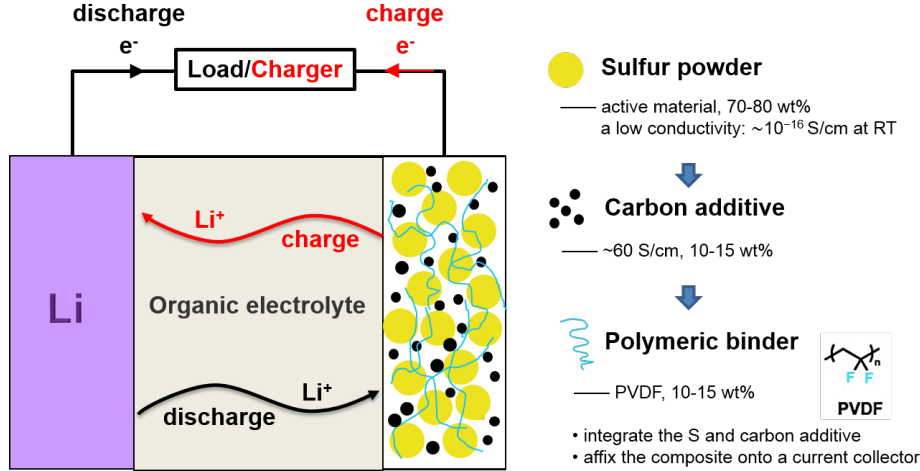


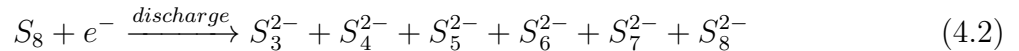
Figure 4.1: Schematic of a conventional Li-S battery and its cathode composition.

polysulfide dianions (PSs)) diffuse back and forward between the two electrodes. This needs to be explained along with the electrochemical processes of Li-S batteries.

At fully charged state, sulfur exists as solid, whose atoms form cyclic octatomic molecules with a chemical formula S_8 . During discharge, metallic lithium is getting oxidized at the anode and produces Li^+ cations and electrons:



Li^+ cations move to the cathode through the separator/electrolyte, while electrons go through external electrical circuit (see Figure 4.1). Sulfur is gradually reduced into PSs (S_n^{2-} ($n=3, 4, \dots, 8$)) by accepting electrons in the cathode:



At fully discharged state, the final product of the electrochemical reaction of sulfur with Li^+ cations and electrons is solid lithium sulfide (Li_2S). During charge, the process takes an opposite way.

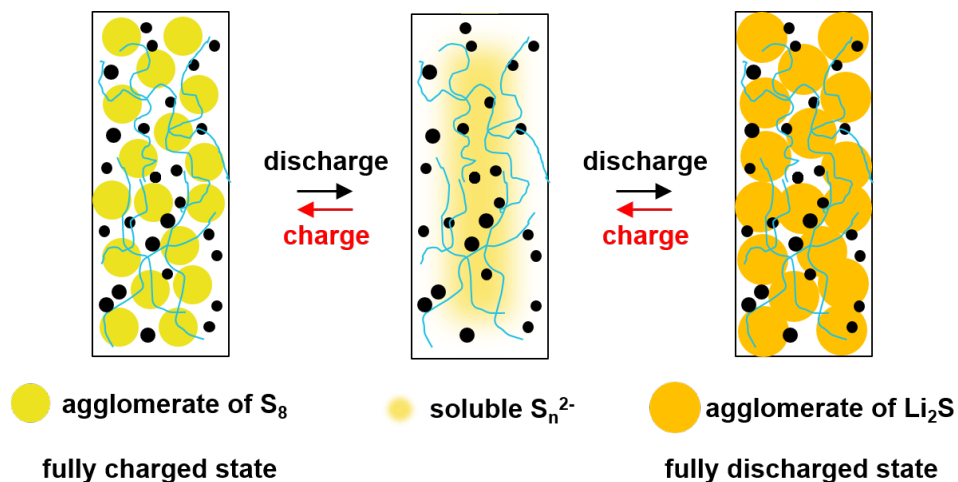


Figure 4.2: Products and intermediates of electrochemical reactions of sulfur species in cathode.

As illustrated in Figure 4.2, the PSs are easily soluble in the organic electrolyte and shuttle between the cathode and anode due to the concentration gradients, thereby causing prolonged charge process, capacity degradation, shortened battery life and other side effects to the performance of the batteries. Particularly, the PSs with longer chain are more soluble. While the most stable PSs in the electrolyte are S_4^{2-} and S_5^{2-} according to the previous research [115].

Although the original purpose of adding a conventional polymer binder, such as PVDF and PEO, is to maintain the integrity of cathode materials and affix the composite onto the current collector when assembling a cell, functional polymer binders have been designed and tested for effective capturing of polysulfide intermediates to enhance the electrochemical performance of Li-S batteries [116, 117, 118, 119, 120, 121, 122]. Next subsection will introduce polymeric binders in terms of properties, structures and the influence on Li-S battery performance.

4.1.3 Polymeric binders: properties, structures and influence on the battery performance

A type of polymeric binder is generally dissolved in a solvent and then added into the composite of carbon additive and sulfur powder, and mixed well with them to be able to maintain the integrity after drying the mixture. Due to the complexity of a Li-S battery system, an effective binder should fulfill multiple requirements, which has shrunk the range of choices from available binders. First of all, the basic properties that a binder should have are the chemical and the electrochemical stabilities. Then, binders need to provide enough binding strength with the cathode materials through interfacial forces (intermolecular forces and chemical bonds) or/and by acting as a physical barrier. Besides those properties, a binder should have proper or good mechanical strength/flexibility to cushion the effect caused by volume change of the active materials during discharge/charge. Also, binders with proper or high ionic conductivity and electric conductivity are always favorable for getting fast charge rate. Currently, PVDF and PEO are commonly used in Li-S batteries. However, researches have never been stopped on developing new binders because both of PVDF and PEO exist some problems. The PVDF may limit the performances of the cell because of poor electronic and ionic conductivities. Also, the toxic organic solvent that PVDF used is difficult to evaporate from the prepared electrodes [106]. PEO is poorly-adhesive to the current collector which may induced by its swelling in some ether-based electrolytes (e.g. TEGDME), and it has low ionic conductivity at room temperature [123].

From the point view of materials science and engineering, material properties are decided by structures. As for binders, the properties depend on their functional groups, polymeric architectures, shapes and so forth, from atomic scale to large scale structures. Seh *et al.* [124] used Li-S \cdot radical as an approximation to stand for long-chain lithium polysulfides (*i.e.*, Li₂S_n or LiPSs) to study the binding strength between LiPSs and different functional groups of polymeric binders. They found that the heteroatoms with lone electron pairs, such as oxygen, nitrogen, and fluorine atoms on the functional groups were able to bind

with the lithium atom in LiS \cdot radical, consequently providing a strong interaction with LiPSs. They also concluded that ester, amide and ketone groups are the top three in binding strength among the model functional groups. It is worthy to note that conductive polymers can play a role of a bifunctional binder which is able to trap the PSs meanwhile improve the conductivity of the cathode. Research groups of Liu and Yang [120, 121, 122] designed a multifunctional binder consisted of fluorenone to optimize electronic conductivity, polyfluorene with octyl side chains to enhance processability, fluorene with triethyleneoxide monomethyl ether side chains to uptake electrolyte and provide mechanical flexibility, and methyl benzoate ester to offer mechanical flexibility as well. In short, synthesis of the multifunctional binder allows enhancement of adhesion, ductility and electrolyte uptake to the levels of those available only in nonconductive binders before, without detrimental effect on electronic conductivity by the modifications of side chains. What's more, even linear polymeric binders are the majority, some branched and network polymeric binders have also been developed due to their mechanical flexibility and strength [125, 126]. In addition, polymers can be manufactured as a coat on sulfur nanospheres [127], nanotubes [128], or a layer of film between cathode and separator to work as a binder and physical barrier to trap polysulfide species [129].

Li-S batteries using different binders show different performance. Ai *et al.* [120] reported that cells with different binders show different cycling stability and self-discharge prevention ability; *i.e.* PVDF < poly(3,4-ethylenedioxythiophene) (PEDOT) < poly(vinylpyrrolidone) (PVP) < poly(9,9-dioctylfluorene-co-fluorenone-co-methylbenzoic ester) (PFM). The best performance of PFM was explained by both its highest electronic conductivity and highest binding strength between carbonyl groups and lithium polysulfides. The binding strength had an effect on inhibiting the shuttle effect. Researchers also benefited from the physical confinement of dissolved polysulfides by polymer binders. For instance, Li *et al.* [127] coated S nanospheres with three types of conductive polymers. The chemical interaction between the heteroatoms of the polymers and lithium polysulfides, in addition to the physical confinement

of lithium polysulfides within the polymer shells, improved the cycling performance of Li-S batteries.

In conclusion, dissolution of PSs in the electrolyte is one of the main problems in Li-S batteries, and binders can be used to trap the dissolved intermediates. The binding strength has an effect on inhibiting the shuttle effect. Moreover, conductive binders can be applied to speed up the charge/discharge rate so that the cycle period of electrochemical experiment and charge time of a real product can be shortened. Accordingly, the electrochemical performance of Li-S cells is able to be improved. Binding strength can be quantified by calculating binding energy. Precious density functional theory (DFT) models computing binding energies will be discussed in the following subsection.

4.1.4 Binding energy between binder and dissolved polysulfides

DFT simulation studies, delving into the mechanism of binding between lithium polysulfides and polymer binders in vacuum, have been well documented for identifying promising binders to effectively tether polysulfide species in Li-S batteries. The binding energies between lithium polysulfides and binders are typically calculated as:

$$\Delta E_{bind} = E_{binder-LiPS} - (E_{binder} + E_{LiPS}) \quad (4.3)$$

where the $E_{binder-LiPS}$, E_{binder} and E_{LiPS} are the calculated energies of the complex, the binder and the lithium polysulfides, respectively. The calculated energies equal to the sum of electron energy and repulsive energy between nuclei:

$$E = E_{ele} + V_{NN} = (T_{ele} + V_{ele}) + V_{NN} \quad (4.4)$$

where the subscript *ele* means electrons, T is kinetic energy, V means potential energy, NN

donates repulsion between two nuclei. Higher binding strength is expected at higher negative binding energies. In addition, heteroatoms with lone pair(s), such as oxygen, nitrogen, and fluorine atoms, in the functional groups of binders are able to bind with Li in lithium polysulfides; consequently, providing strong interaction with lithium polysulfides [124, 127, 130, 131, 132]. The interaction between Li and heteroatoms with lone pair(s) dominates the electrostatic attraction [133, 131], while the interaction between S and binder mainly contributes to the dispersion attraction [119, 133]. Previous studies [119, 124, 127] showed that the binding energy between an atom of a polymer binder and an atom of lithium polysulfide species was typically less than ca. 1.5 eV, which is a weak interaction.

In 2013, Cui's research group published two literatures [124, 127] in which binding energies between polymeric binders and LiPSs were calculated using DFT method and projector augmented wave/Perdew-Burke-Ernzerhof functional (PAW/PBE) [134, 135] level. Regarding LiS· radicals as an approximation to stand for long-chain LiPSs, Seh *et al.* [124] systematically investigated the binding energies between LiS· radicals and different functional groups on polyvinyl backbones using the Vienna ab Initio Simulation package (VASP) [136, 137]. Through the same DFT method, Li *et al.* [127] studied binding energies between three of the most well-known conductive polymers and LiS· radicals. In general, the heteroatoms with lone electron pairs (such as oxygen, nitrogen, and fluorine atoms) were able to bind with the lithium atom in LiS· radical. Their model provides a meaningful reference to compare binding strengths between LiS· radicals and a series of functional groups. More than that, their experimental results proved the computed binding strength relationship that $\text{Li}_2\text{S-PVP} > \text{Li}_2\text{S-PVDF}$. However, a long-chain LiPS is a ring-like structure and has much larger spatial volume and dispersion interaction (also called dispersion forces) with binders or anchoring materials than the radical [138, 133]. In addition, the contribution of sulfur atoms to binding energy could be underestimated. This may be one of the reasons why their experimental results regarding binding strengths of PANI and PPY were inconsistent with the computational results, as mentioned in last subsection.

In 2015, Cui’s research group [133] modified the model using a vdW-DF2 functional [139, 140] to consider the effect of dispersion interaction, and lithium (poly)sulfide molecules (Li_2S_8 , Li_2S_6 , Li_2S_4 , Li_2S_2 , and Li_2S as well as S_8) but not the radicals were modeled to study their binding energies with two-dimensional (2-D) layered materials (oxides, sulfides, and chlorides) and graphene. In agreement with our expectation, their results showed that the dispersion interaction is very important. They found that the chemical interaction mainly comes from the Li atoms, whereas the dispersion interaction is largely contributed by S atoms. For graphene, Li_2S_8 among the LiPSs owned the highest binding energy; while for 2-D layered materials, Li_2S was possessed of the highest binding energy. The ratio of dispersion interaction in the case of S_8 for all tested materials was more than 90% while that of Li_2S was in the range of ca. 5~70 %, computed by:

$$R = (E_{bind_D} - E_{bind_{noD}})/E_{bind_D} \quad (4.5)$$

where R , E_{bind_D} and $E_{bind_{noD}}$ represent ratio of dispersion interaction, binding energies calculated with and without dispersion interaction, respectively. They pointed out a concept for the anchoring material (AM) design that suitable electron donating group should be used: not too strong to facilitate Li^+ ion diffusion and not too weak to trap the lithium polysulfides. For the graphene case, the amorphous structure was found to be able to improve the binding effect than the crystal structure. These two conclusions could be helpful for binder design. The effect of dispersion interaction on conformation has been visualized. The distance between a S_8 molecule and the TiS_2 surface decreased, and lying-in-plane configuration was favorable for Li_2S_8 and Li_2S_6 because of the relatively long sulfur chains. As for Li_2S_4 , Li_2S_2 and Li_2S , the adsorption configurations were almost not influenced. In 2018, Cui’s group made a progress for the binding interactions of PVDF-LiPS and ammonium polyphosphate (APP)-LiPS [119] with the same dispersion correction (*i.e.*, vdW-DF2 functional) as their previous model [133]. The PVDF- Li_2S interaction was 0.72 eV [124] after considering the

dispersion correction, which was different with the previous value of 0.64 eV [119]. The interactions of PVDF-LiPS were 0.59, 0.61 and 0.74 eV for PVDF-Li₂S₈, PVDF-Li₂S₄ and PVDF-Li₂S₂, respectively [119]. Consider the variation of values, they were not suitable to be represented by the PVDF-LiS· interaction which was 0.83 eV [124].

Recently, more and more DFT modeling has been performed in literatures to elucidate why PS species can be or cannot be adhered strongly on various types of binders or anchoring materials. Xu *et al.* [130] studied the adsorption of Li₂S and LiS· on polyacrylic acid (PAA) by PAW/PBE level. They concluded that Li atom of LiPSs formed Li-O bond with PAA and interacted with the coterminous oxygen in PAA, and possessed a higher binding energy with LiPSs compared with PVDF. As a result, the Li-S battery based on PAA offered better cycling performance than that based on PVDF. Ji *et al.* [131] assembled four types of the constituent deoxynucleotides (DNs) of DNA to model the anchoring environment for PSs, and calculated the binding energies of Li₂S_n (n=3, 4, 6, 8) with the assembly of DNs. Consider the fact that Li₂S₈ had the largest solubility in the electrolyte [124, 141], which meant LiPSs species could be confined as long as Li₂S₈ could be trapped, Ji *et al.* simplified the model by selecting Li₂S₈ to investigate the anchoring behaviors of LiPSs in DMol³ package [142] and demonstrated that the sulfur atoms would interact with the positively charged portion of DNs via H-bonds, which had enhanced the adsorption strength. Deng *et al.* [132] calculated binding energies between Li₂S_n (n=1, 4, 6 or 8) and polydopamine (PDA). They got the similar conclusion as Seh *et al.* [124] and Li *et al.* [127] that the N and O atoms with lone electron pairs would promote the strong interactions between PDA and LiPSs. Note that the software, method and calculation level were VASP, DFT and PAW/PBE in these three researches [124, 127, 132].

Theoretical modeling and analysis of the interaction between LiPSs and nitrogen-doped graphene (N-G) can also shed light on binder innovation for Li-S batteries. Yin *et al.* [143] implemented DFT computation using PAW/PBE in VASP [137] and incorporated dispersion interactions by the optB88 exchange functional [144, 145]. Through calculating

binding energies between lithium (poly)sulfides and N-G with different doping configurations, this systematic study provided a fundamental understanding on the interactions. It was found that only N-G doped with clustered pyridinic N (pN) could bind soluble LiPSs much more strongly than the electrolyte solvents (1,3-dioxolane and 1,2-dimethoxyethane) did, implying clustered pN-dopants in N-G were the intrinsic reason for the effective suppression of LiPS shuttling by N-G. Hou *et al.* [146] took pN as a typical example to investigate the nature of Li bond between Li and pN. Geometry optimizations were performed at a B3LYP (Becke's three-parameter hybrid method using the Lee-Yang-Parr correlation functional)/6-311++G(2d,p) level [147] in Gaussian 09 [148]. The binding energy of a model molecule, pyridine (PD) with Li_2S_8 was examined by DFT in DMol³ package [142]. Finally, the nature of Li bond was identified as an electrostatic dipole-dipole interaction rather than a typical chemical bond where charge transfer occurs, considering the large dipole of Li_2S_8 -PD cluster with minor charge transfer between Li_2S_8 and PD cluster. Its bond strength was probed to mainly rely on the dipole of Li_2S_8 -PD cluster along with extra conjugative and inductive effects. Concretely, π -electrons in the conjugated system of PD were obviously attracted to the Li...pN bond. Simultaneously, the Wiberg bond order of N-C bond changed from 1.423 to 1.385 after PD binding to Li_2S_8 , and the bond order of Li...pN bond was 0.108. The authors also theoretically predicted ⁷Li NMR spectroscopy which was in good accordance with the experimental one, suggesting the chemical shift in ⁷Li NMR spectroscopy as a quantitative descriptor of Li bond strength. Sun *et al.* [149] followed their previous modeling method [143] and found that Li_2S_6 had a binding energy of 1.07 eV with pN-G, much smaller than that with vanadium nitride (VN) (3.75 eV). This has been attributed mainly to the much weaker polar-polar interactions between Li_2S_6 and pN-G than those between Li_2S_6 and VN.

Despite extensive DFT simulation studies on binding strength of lithium polysulfide species and binder chains in vacuum environment, reliable molecular dynamics (MD) modeling of the binding effectiveness is very limited. In the framework of MD, important atomistic details with respect to polymer binders can be studied. In the present work in the chapter,

explicit solvation models are built using MD modeling in order to consider the effect of solvent molecules on the binding effectiveness between binders and polysulfides. Not only the interaction energies between polysulfides and polymers are calculated, but also the movements of polysulfides and polymers in the solvent over time are predicted. Furthermore, the binding effectiveness is also studied when considering the real weight ratio between sulfur and binder.

4.2 Full-atomistic MD simulation

4.2.1 Model species and the relevant partial atomic charges

It is well known that polysulfide species with a longer chain are more soluble in electrolytes [124, 141] while being relatively easier to be physically captured in a porous matrix, a protective interlayer or other porous structures in the cathode, or by the separator. Furthermore, according to the previous research [115], S_n^{2-} species with $n \leq 5$ are more stable with lithium metal than the long-chain S_n^{2-} species with $n \geq 6$. Therefore, as a relatively stable and soluble polysulfide species in the electrolyte, tetra-sulfide (S_4^{2-}) was selected to represent polysulfide species in this work. Although early studies have reported the formation of sulfur radical species during discharge [150, 151, 152, 153], this work focuses on polysulfide dianions. The following conductive polymers were selected as model binders: PEDOT, polypyrrole (PPY), and polyaniline (PANI) due to their electrochemical stability in Li-S batteries [127], commercial availability and popularity in research studies on Li-S batteries [120, 127, 129, 154, 155, 156, 157, 158]. And we applied the previous concept of simplicity [127] that choosing the undoped form of each polymer.

The partial atomic charges of the relevant molecules and ions are shown in Figure 4.3, which were derived by first optimizing the geometry in a polarizable continuum model using the integral equation formalism variant (IEFPCM) [159, 160, 161] (dielectric constant $\epsilon=7.1$) [162]) based on B3LYP-D3(BJ)/def2-TZVP level [147, 163, 164, 165] of calculation using

Gaussian 16, Revision B.01 [166] and then fitting the electrostatic potential surface using restrained electrostatic potential (RESP) method [167] by employing Multiwfn package [168]. The IEFPCM model [159, 160, 161] treated solvent effects approximately with the $\epsilon=7.1$ to describe the polarity of the surrounding 1:1 v/v DOL:DME environment. As for the dielectric constant $\epsilon=7.1$, it was calculated based on the volume fractions of DOL and DME according to an approach which has long been recognized [169]: $\epsilon = \epsilon_{DOL} \times 50 \text{ vol\%} + \epsilon_{DME} \times 50 \text{ vol\%}$, where $\epsilon_{DOL}=7.0$ and $\epsilon_{DME}=7.2$ [162]. All of the optimized geometries were verified as minima by frequency computations (zero imaginary frequencies). Figure 4.3 was drawn using GaussView 6.0 [170].

4.2.2 Establishing MD box

The side length of a box should be large enough to give at least a distance of 20 Å between polymer and its own mirror image in a periodic system in order to avoid undesirable interactions during MD simulations. Additionally, the length of a polymer chain needs to be confined to prevent such interactions. If a polymer chain coils during MD simulation thus avoiding such interactions, then a chain length longer than the side length of the box is acceptable for the polymer. Otherwise, the chain length of a stiff polymer chain such as PPY or PEDOT needs to be shorter than the side length of a MD box. Based on current computational resources, a side length of a cubic box as large as approximately 10 nm was used in the present work. Then length of polymer chains was limited to this range, considering the stiffness of PPY and PEDOT chains, namely the hardness to coil in MD box. In addition, PEDOT, PPY, PNB and LEB chains were designed to have similar molecular weight in the simulations. As a result, their molecular weights were 1123.29, 1108.26, 1083.25 and 1095.34, for polymer chains consisting of 8, 17, 6 and 6 repeat units (Figure 4.3), and the lengths of their straight chains were approximately 32 Å, 63 Å, 68 Å and 68 Å, respectively. The ends of polymer chains were terminated with hydrogen atoms.

In a typical sulfur electrode of Li-S batteries, the weight percentage of polymer binder

is no more than 10 wt%, and the weight percentage of sulfur is no less than 50 wt% [120, 157, 171, 172]. Using a weight ratio of 50 wt% sulfur to 10 wt% binder in his work, the weight ratio of S_4^{2-} to binder, which was assumed as 5:1, is equal to the weight ratio of 43 S_4^{2-} dianions to 1 polymer chain. The number of Li^+ ions added to a system was twice the number of S_4^{2-} dianions in order to maintain electric neutrality of the system.

The initial structures of five types of simulations were built using Packmol [173]: (1) one polymer chain, one S_4^{2-} dianion and two Li^+ ions (Figure 4.4(a)); (2) one polymer chain, 43 S_4^{2-} dianions and 86 Li^+ ions (Figure 4.5(a)); (3) one polymer chain, one S_4^{2-} dianion and two Li^+ ions dissolved in the solvent mixture (Figure 4.4(c)); (4) one polymer chain, 43 S_4^{2-} dianions and 86 Li^+ ions surrounded by the solvent mixture (Figure 4.5(c)); and (5) randomly packed 1 polymer/43 S_4^{2-} /86 Li^+ and solvent molecules.

The initial structures of the first two types of simulations were established by randomly packing the species. For the third and the fourth types of explicit solvation models, the assembled polymer, S_4^{2-} and Li^+ ions were placed at the center of a cubic box periodic in XYZ direction. Then the free volume in the box was filled with the organic solvent mixture of 1:1 v/v dioxolane/dimethoxyethane (DOL/DME). According to the reported densities of DOL (1.05862 g cm⁻³) and DME (0.86109 g cm⁻³) [174, 175] at 298.15 K, the ratio of the number of DOL molecules to the number of DME molecules was approximately 300:200 in such a solvent mixture. For the last type of explicit solvation model, the numbers of DOL and DME molecules were the same for each polymer system for comparison purposes. The numbers of molecules and ions in this type of model were 1 polymer+43 S_4^{2-} +86 Li^+ +4500 DOL+3000 DME.

4.2.3 MD simulation

Full atomistic MD simulations on S_4^{2-} , Li^+ and polymer binder in 1:1 v/v DOL/DME were performed using GROMACS version 2018.4 [176, 177, 178, 179, 180, 181, 182] with the general AMBER force field (GAFF) [183]. The classical non-polarizable force field could

significantly underestimate or overestimate some important parameters such as diffusion coefficient and viscosity of a system with high ionic concentration due to the polarization effect [184]. But according to a previous work which also used the GAFF to run MD simulations for systems of Li(TFSI) and Li_2S_x ($x = 4, 6, 8$) in DOL:DME [162] and compared properties such as diffusion coefficients of Li^+ , TFSI $^-$, DOL as well as DME in Li(TFSI)/DOL:DME at different ionic concentrations with experimental counterparts, it is acceptable to use GAFF for the systems in the present work since their ionic concentrations are no larger than 0.068 M (represented by concentration of S_4^{2-} in the solvent mixture). The van der Waals (vdW) parameters of Li^+ was from the AMBER99 force field [185]. The acpype.py script [186, 187] was executed to employ Antechamber module [188] of AmberTools 18 [189] to create topology files of the species and subsequently convert the topology files to the GROMACS format. The procedures for the first four types of MD simulations are summarized in Figures 4.4 and 4.5, in which the structures regarding PPY are shown as examples. Unless mentioned otherwise, the snapshots of structures in this work were presented using VMD [190]. The structures of molecular fragments are presented in Figure 4.3.

At the beginning of each simulation for systems without the consideration of the solvent mixture, single- S_4^{2-} systems went through a MD step of 4 ns while multiple- S_4^{2-} systems went through a longer MD step of 14 ns. In order to accelerate the calculations, the lengths of bonds involving hydrogen atoms were converted to constraints using the LINCS algorithm [191], and the time step for integration was 2 fs. Temperature was controlled at constant 298.15 K using velocity-rescale thermostat [192] with a time constant of 0.2 ps. The cut-off treatment scheme was group. For both electrostatic and vdW interactions, the interaction types were plain cut-off with pair list radius, vdW cut-off and Coulomb cut-off equal to 0 thereby interactions between all particles were able to be calculated. The neighbor list was only constructed once at the beginning and never updated.

For each system with the solvent mixture, the initial structure (Figure 4.4(c) or 4.5(c)) was constructed by using the assembly with the lowest interaction energy between Li_2S_4 and

polymer (Figure 4.4(b) or 4.5(b)), which was derived from the corresponding simulation in vacuum. The energy minimization (EM) for each system was conducted with the conjugate gradient algorithm with a tolerance of $100.0 \text{ kJ mol}^{-1} \text{ nm}^{-1}$ and position restraints imposed on S_4^{2-} , Li^+ and polymer chain in XYZ direction. For some cases, a steepest descent step was done while doing every two steps of conjugate gradient energy minimization. Then the solvents were equilibrated through a 1 ns MD process which was implemented with position restraints imposed on S_4^{2-} , Li^+ and polymer chain in XYZ direction. During the process, the temperature of the system was gradually increased from 0 K to 298.15 K in the first 100 ps and then maintained at 298.15 K, which was controlled by the velocity-rescale thermostat [192] with a time constant of 0.2 ps; and the pressure was maintained at 1 bar with a time constant of 0.5 ps using the isotropic Berendsen barostat [193]. Finally, a MD step of 20 ns was run for the single- S_4^{2-} system, while a MD step of 50 ns was run for the multiple- S_4^{2-} system. In this step, the pressure and temperature were controlled by the isotropic Parrinello-Rahman barostat [194] with a time constant of 3.0 ps and by the velocity-rescale method [192] with a time constant of 0.2 ps; respectively. For the MD and position-restrained MD steps, the cut-off scheme was Verlet. The Smooth Particle-Mesh Ewald method [195] was used to account for long range electrostatic interactions. The short range vdW interactions were calculated by a cut-off method. The distance was set as 1.0 nm for both the short-range electrostatic interactions in real space and the vdW interactions. Long range dispersion corrections for energy and pressure were applied. The time step for integration was 2 fs while the lengths of bonds with H-atoms being constrained using the LINCS algorithm [191].

As for the simulations of randomly packed polymers, S_4^{2-} , Li^+ and solvent molecules, the procedures and parameters were the same as those mentioned above except with no position restraints on species. Additionally, the equilibrium stage and production stage were respectively run for 6~8 ns and 200~300 ns for systems with 1 polymer chain.

To validate the accuracy of the force field parameterization for the pure solvents, the

densities of DOL and DME were calculated by a procedure of three successive steps EM + 4 ns MD equilibrium run + 4 ns MD production run, then extracted from the MD production runs based on a cubic box of pure solvent with side length of approximate 5.5 nm, and finally compared with data reported in literature [174, 175]. The calculated density of DOL (0.97744 g cm⁻³) is slightly underestimated by 8% while that of DME (0.88909 g cm⁻³) is slightly overestimated by 3% with respect to the corresponding values in literature (1.05862 g cm⁻³ and 0.86109 g cm⁻³ at 298.15 K); differences below 10% are usually considered as acceptable [196].

4.2.4 Calculation of interaction energy

In MD, the non-bonded interaction energy between two groups of particles is contributed by vdW and electrostatic interaction energies which are respectively computed by Lennard-Jones (LJ) and Coulomb (Coul) terms in GAFF, as shown below:

$$E^{nonbond} = \sum_{A>B} (E_{AB}^{vdW} + E_{AB}^{ele}) = \sum_{A>B} (E_{AB}^{LJ}(r_{AB}) + E_{AB}^{Coul}(r_{AB})) \quad (4.6)$$

where the sum operator means the summation of interactions between each pair of atoms, and r_{AB} indicates the distance between atom A and atom B. For model systems without consideration of the solvent, the interactions between all particles are calculated for both electrostatic and vdW interactions. But in explicit solvation models, both the electrostatic interactions and the vdW interactions are calculated by cut-off method within a cut-off distance of 3.0 nm.

4.3 Results and discussion

4.3.1 Single polymer chain and single lithium tetra-sulfide in vacuum

Three replicas of each simulation of the polymer systems were run and the frame with the strongest Li_2S_4 -polymer attractive interaction was selected for analysis. In the case of LEB, the frame with a straight chain segment, as shown in Figures 4.6(b) and (f), was selected for comparison with previously published results [127]. Note that an LEB chain can form a coiled conformation in vacuum due to its interaction with Li_2S_4 (Figure 4.7), which has a higher Li_2S_4 -LEB attractive interaction. Figure 4.6 illustrates the structures for these frames, (a)-(h), and the interaction energies of S_4^{2-} -polymer and Li_2S_4 -polymer. To investigate which atoms are major contributors to the components of the interaction energy (*i.e.* vdW and electrostatic interaction energies), an energy decomposition analysis based on molecular force field (EDA-FF) [197, 198] was performed based on GAFF using Multiwfn package [168], as presented in Figure 4.8. The vdW interaction energy, which is described by LJ potential, is divided into an exchange repulsion term and a dispersion term. Also, Figure 4.8 shows that Li_2S_4 mainly interacts with three adjacent units of the polymer in each case. Therefore, the polymer lengths applied in the work should be long enough for calculating the interactions between the polymers and the ions.

The S_4^{2-} dianion attracts Li^+ ions while the two Li^+ ions repulse each other. As a result, the favorable configuration of a S_4^{2-} dianion and two Li^+ ions is a sandwich-like Li_2S_4 assembly. The electrostatic interaction between the Li^+ and polymer contributes to the attraction between Li_2S_4 and polymer, significantly. This is illustrated in Figure 4.8 and the comparison between the S_4^{2-} -polymer interaction energy, Figure 4.6(i), and the Li_2S_4 -polymer interaction energy, Figure 4.6(j), for each polymer system. The vdW interactions between the Li^+ and the polymers PNB, LEB and PPY are repulsive due to the larger contribution of exchange repulsion (Figure 4.8(e), 4.8(f) and 4.8(h)) than that of the dispersion (Figures

4.8(i), 4.8(j) and 4.8(l)). This explains why the vdW interaction energy components in the cases of PNB, LEB and PPY in Figure 4.6(j) are smaller than those in Figure 4.6(i). However, the decrease in vdW attraction is low compared to the boost in the electrostatic attraction between polymer and Li_2S_4 caused by the Li^+ .

In summary, polymer and Li_2S_4 attract each other predominantly through electrostatic interaction contributed by Li^+ , and slightly through vdW interaction contributed by S_4^{2-} . The order of the total interaction strength in these polymer systems is: $\text{PNB-Li}_2\text{S}_4 > \text{PEDOT-Li}_2\text{S}_4 > \text{LEB-Li}_2\text{S}_4 > \text{PPY-Li}_2\text{S}_4$ with a ratio of 2.91 : 1.06 : 1.03 : 1. The reason why PNB has the largest total or electrostatic interaction strength with Li_2S_4 is attributed to both Li^+ ions interacting with three N atoms of the polymer chain, as illustrated in Figure 4.8(a). Comparatively, the order achieved in this work is similar to previous published work ($\text{PEDOT-Li}_2\text{S}$ ($104.2 \text{ kJ mol}^{-1}$) $>$ $\text{LEB-Li}_2\text{S}$ (56.9 kJ mol^{-1}) $>$ $\text{PPY-Li}_2\text{S}$ (48.2 kJ mol^{-1}), $\text{PEDOT-LiS}\cdot$ ($117.7 \text{ kJ mol}^{-1}$) $>$ $\text{LEB-LiS}\cdot$ (64.6 kJ mol^{-1}) $>$ $\text{PPY-LiS}\cdot$ (61.8 kJ mol^{-1})) [127]. The quantitative difference is likely attributed to two main reasons: (a) the representative lithium (poly)sulfides used in previous simulations (Li_2S and $\text{LiS}\cdot$) were different than the Li_2S_4 used in this work. As mentioned above, S mainly contributes to vdW interaction, therefore it is inferred that Li_2S_4 may contribute more vdW interaction than Li_2S and $\text{LiS}\cdot$; and Li_2S_4 has different spatial structure than Li_2S and $\text{LiS}\cdot$, namely the distance between atoms of the (poly)sulfides and the polymers are different, thus the interactions are influenced. (b) In the present work, the atomic charges of Li^+ and S_4^{2-} were set as +1 and -2, respectively; and the atomic charges of other species were calculated using the solvation model. In other words, the atomic charges in this work are different than previous work therefore the electrostatic interactions are different.

4.3.2 Single polymer chain and single lithium tetra-sulfide in solvent

In the presence of a solvent in the polymer systems, the attractive interactions between polymers and Li_2S_4 decrease, as illustrated by the green lines in Figure 4.9. In Figure 4.9(a), the Li_2S_4 -PNB distance remains around 2.1 Å. The conformations at different times show that the PNB chain gradually uncoils with the effect of solvent and its end group 2 (see Figure 4.3e) always attaches Li_2S_4 . This indicates that the end group 1 and the repeat unit (Figures 4.3c and 4.3d) of PNB cannot effectively bind Li_2S_4 while its end group 2 can maintain the attachment over time. However, a distinguished interaction strength between the end group 2 of LEB (Figure 4.3h) and Li_2S_4 , or between the end group 1 or the repeat unit of LEB (Figures 4.3f and 4.3g) and Li_2S_4 is not observed and the Li_2S_4 gradually detaches from the LEB chain. Detaching phenomena between polymer and Li_2S_4 also happen in the cases of PEDOT and PPY, as indicated by the magenta lines in Figures 4.9(c) and 4.9(d). The examples of detached conformations are presented in Figure 4.10.

4.3.3 Polymer binders and lithium tetra-sulfides (1:5 w/w polymer/tetra-sulfide) in vacuum

The previous simulations consider how polymer chains interact with only one Li_2S_4 . Typically, the weight ratio between sulfur and binder is no less than 5 in Li-S batteries which means that each polymer chain matches 43 tetra-sulfide dianions when using tetra-sulfide dianions to represent the sulfur species. In order to analyze the binding ability of each polymer chain with 43 tetra-sulfide dianions and 86 Li^+ ions, three replicas of each simulation were carried out in vacuum for the polymer systems. The frame with the strongest Li_2S_4 -polymer interaction was selected for analysis and to be used for constructing initial structures of the explicit solvation models for each polymer system.

Figures 4.11(a)-(h) show the structures of the simulation frames. It can be observed

that Li^+ and S_4^{2-} form a cluster in each system, and the interaction between the cluster and each polymer results in a twisted and/or bended conformation of the polymer chain. Figures 4.11(i) and 4.11(j) show the S_4^{2-} -polymer and Li_2S_4 -polymer interaction energies; respectively. The Li^+ in the clusters contributes to the attractive interaction mainly through electrostatic interaction, while S_4^{2-} makes the contribution mainly by the vdW interaction, which agrees with the conclusion derived from the single- S_4^{2-} systems. The strength order of total interactions of polymer- Li_2S_4 is: $\text{PPY-Li}_2\text{S}_4 > \text{PNB-Li}_2\text{S}_4 > \text{LEB-Li}_2\text{S}_4 > \text{PEDOT-Li}_2\text{S}_4$, which is different than the single- S_4^{2-} systems. As for PEDOT, the interaction with Li_2S_4 is the weakest possibly due to its number of units is the smallest among the binders. On the other hand, PPY has the largest number of units thus possessing the strongest interaction with Li_2S_4 . Figure 4.11(e) shows that an end of the PNB chain is dangling, indicating that the end of PNB has weaker binding effect with Li_2S_4 . The LEB chain doesn't have dangling parts (Figures 4.11(b) and 4.11(f)) since its end groups and repeat units have similar interaction strengths with Li_2S_4 , but its binding effect with Li_2S_4 is still weaker than that of the PNB. The other noteworthy point is that the ratios of the vdW interaction components in the total Li_2S_4 -polymer interactions become larger.

4.3.4 Polymer binders and lithium tetra-sulfides (1:5 w/w polymer/tetra-sulfide) in solvent

In the absence of a solvent in the polymer system, the ends of the polymer chains bend and twist to attach to as much of the surfaces of Li_2S_4 clusters as possible, as shown in Figures 4.11(a)-(h). However, with the presence of a solvent in the system, the polymer chains tend to detach from the surfaces of Li_2S_4 clusters, except for PNB, as shown in Figures 4.12(a)-(d). This implies that the attractions of LEB, PEDOT and PPY with the Li_2S_4 clusters are not large enough to hold the Li_2S_4 clusters. Compared with the results in Figure 4.11(j), the Li_2S_4 -polymer interaction energies in Figures 4.12(e)-(h) increase due to the effect of solvent. And the ratios of vdW interaction to electrostatic interaction change slightly except

in the cases of LEB and PEDOT in which the vdW interactions become larger than the electrostatic interactions. The end group 2 of PNB always attaches on the surface of the cluster (Figure 4.12(a)), which renders PNB having the highest interaction strength with the Li_2S_4 cluster among the binders. Since most units of the chains have access to the solvent (Figures 4.12(b) and (d)), LEB and PPY have the weakest interaction with the Li_2S_4 cluster.

Although the binding strength is not enough for the polymer to trap the Li_2S_4 cluster firmly in each system, the assembly of the Li_2S_4 cluster and the polymer chain still exists over time because the structure of the cluster is maintained during the MD process and restricts the move of the polymer chain. In addition, the position of each cluster with respect to the polymer is stable during the simulation. The calculated interaction strengths between polymers and clusters represent the upper limit of interaction strengths between the polymer chains and 43 Li_2S_4 . When each polymer chain, 43 S_4^{2-} ions and 86 Li^+ ions were distributed randomly in the solvent mixture at the beginning of modeling process, the ions form electroneutral clusters with various sizes (Figure 4.13) rather than forming only one large cluster, which agrees with the simulation results of previous work [162]. Based on these results, it could be inferred that the interactions between these clusters and the polymer chains would not be strong enough to endure the attachments, thus the clusters would approach and then interact with the polymer chains only by chance.

The simulation results shown in Figure 4.14 confirms this inference, which displays the numbers of Li_2S_4 attached by binders at different time points during the last 20 ns of the MD simulations. Only PNB maintains attraction with Li_2S_4 due to the end group 2. And it illustrates that one end group 2 of PNB could stably maintains attraction with 2 out of 43 Li_2S_4 molecules while the repeat units of PNB, LEB, PEDOT and PPY seem ineffective in adsorbing Li_2S_4 . However, this doesn't mean PNB can effectively bind Li_2S_4 because the polymerization degree of PNB will be much larger, hence the ratio of the end group 2 relative to the repeat units is quite small. Therefore, undoped conjugated PNB, LEB, PEDOT and PPY seem to have ineffective performance in binding polysulfides through

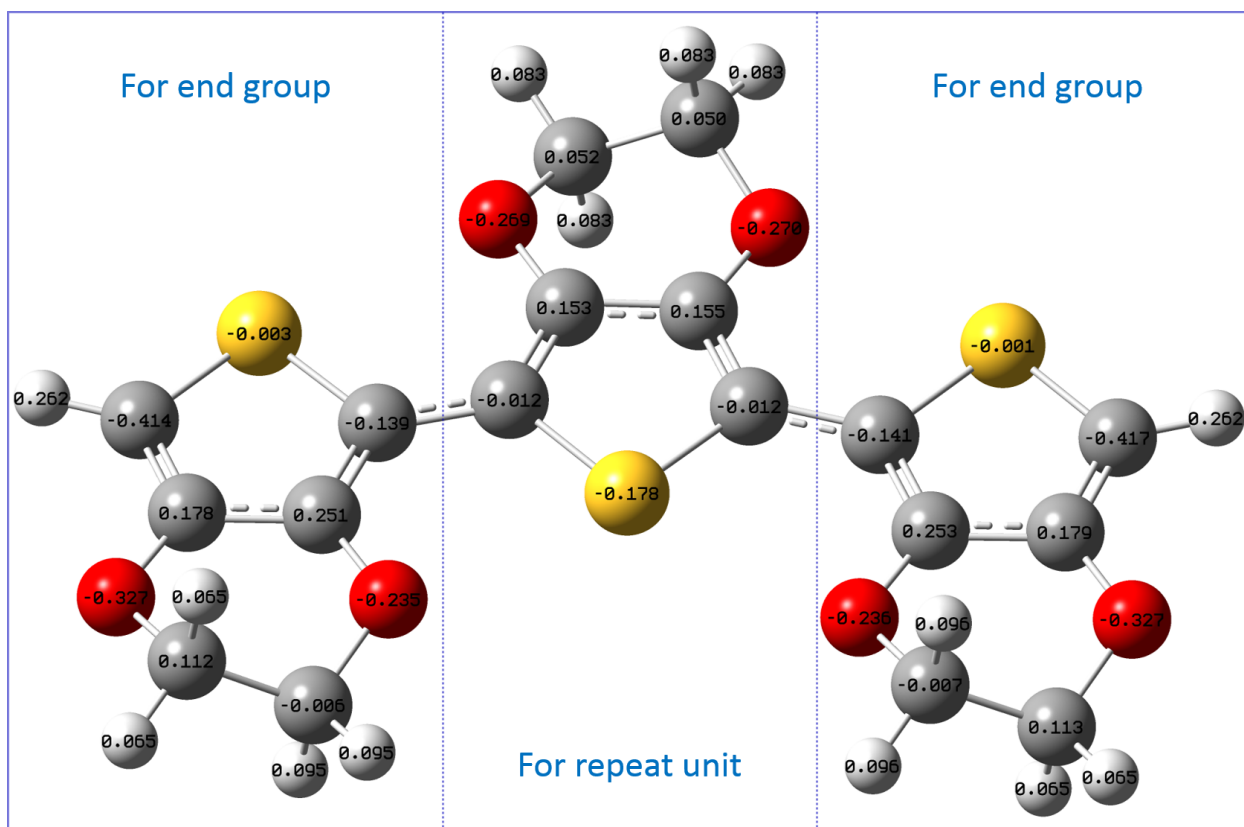
non-bonded interaction, especially when the concentration of polysulfide/binder in a local domain of the cathode is as low as that in the simulations.

4.4 Conclusions

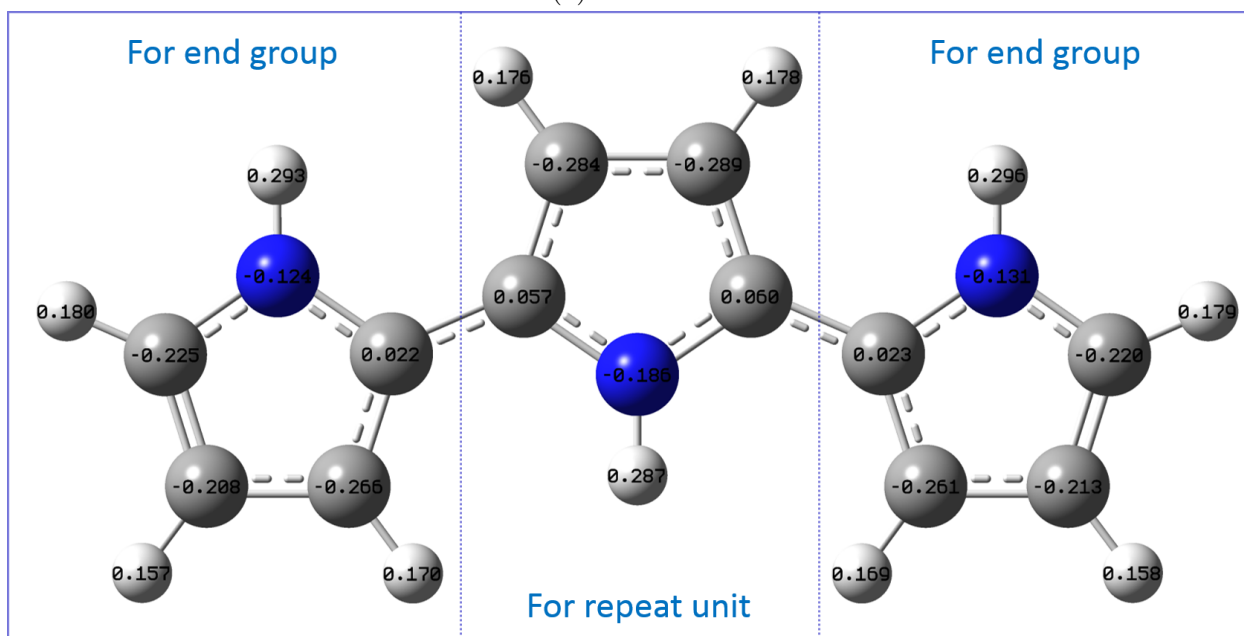
Full-atomistic MD simulations have been performed to unravel the binding effectiveness between tetra-sulfides and polymer binders PNB, LEB, PEDOT and PPY with the effect of a 1:1 (v/v) mixture of DOL/DME when considering the ratio between sulfur and binder in a real Li-S cell. The simulations in solvent demonstrate that the end group 2 of PNB can effectively bind one Li_2S_4 cluster or 2 out of 43 Li_2S_4 molecules with the effect of the solvent mixture through non-bonded interaction. However, the chain length of PNB used in this work is limited by the computing resources available. In a real case, the ratio of the end group 2 relative to the repeat units is quite small thus the group 2 will not play an important role in attracting Li_2S_4 . Therefore, PNB, LEB, PEDOT and PPY seem to be ineffective in binding polysulfides through non-bonded interaction, especially when the concentration of polysulfide/binder in a local domain of the cathode is as low as that in the simulations. Based on that, polymers with the functional group (*i.e.* end group 2 of PNB) are suggested to be further studied in order to get effective binders.

The constructed MD models have a potential to be extended to study binding effectiveness between polysulfides and polymers under other influencing factors, such as side groups of polymer binders and doped states of conductive binders. Since the solvent environment has considerable impact on the binding effectiveness between tetra-sulfides and binder, it is suggested to use the explicit solvation models, similar to the ones built in this work, to predict how other influencing factors affect binding effectiveness between polysulfides and polymers, which will contribute to the existing demand for guiding binder design and rational experiments for Li-S technology as well as propel the advancement of MD modeling methodology for understanding properties and performance of polymer materials in energy

storage systems.

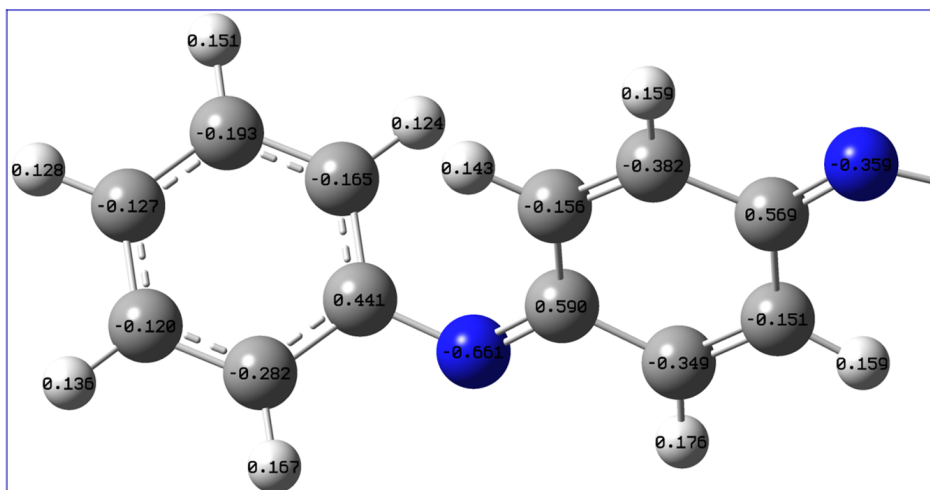


(a) PEDOT.

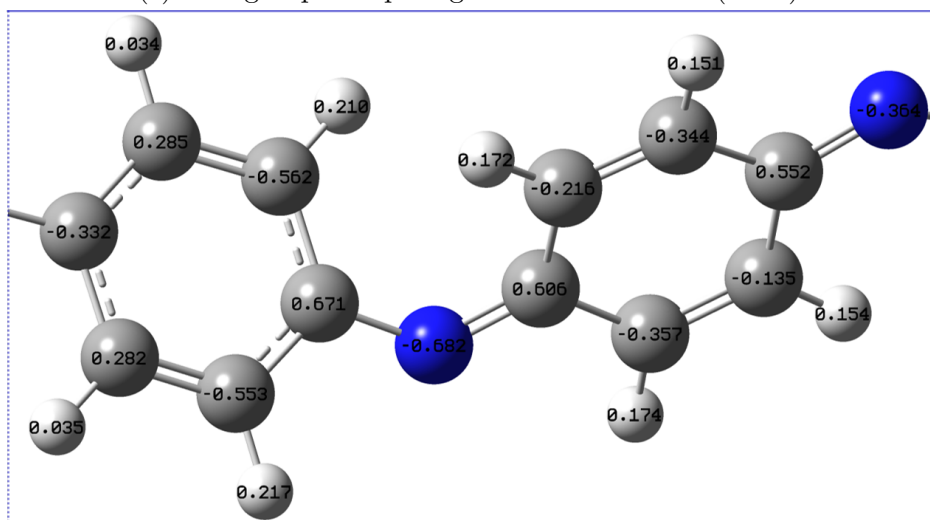


(b) PPY.

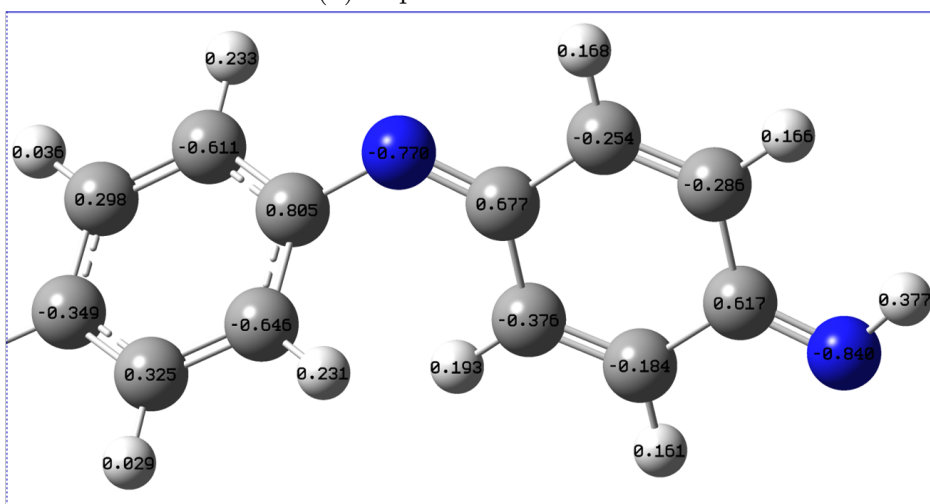
Figure 4.3: RESP charges of species.



(c) End group 1 of pernigraniline base PANI (PNB).

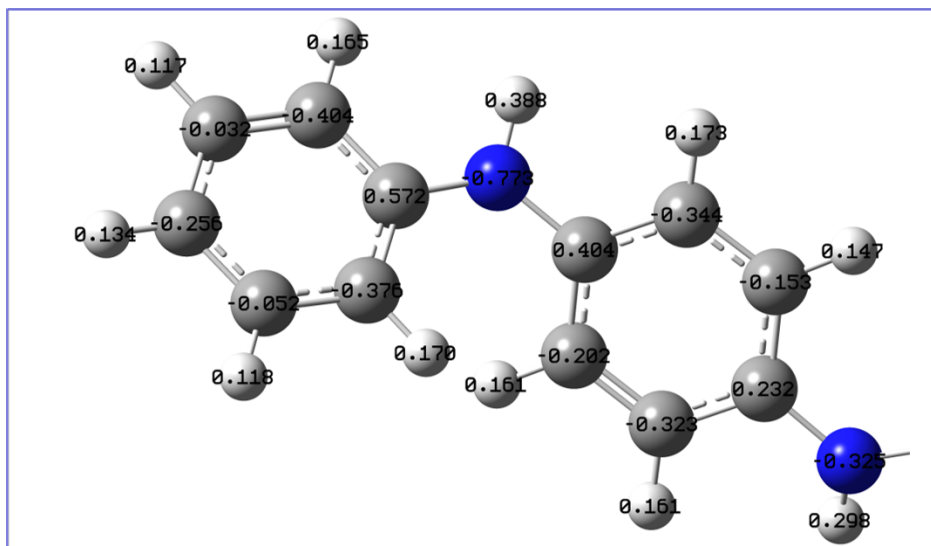


(d) Repeat unit of PNB.

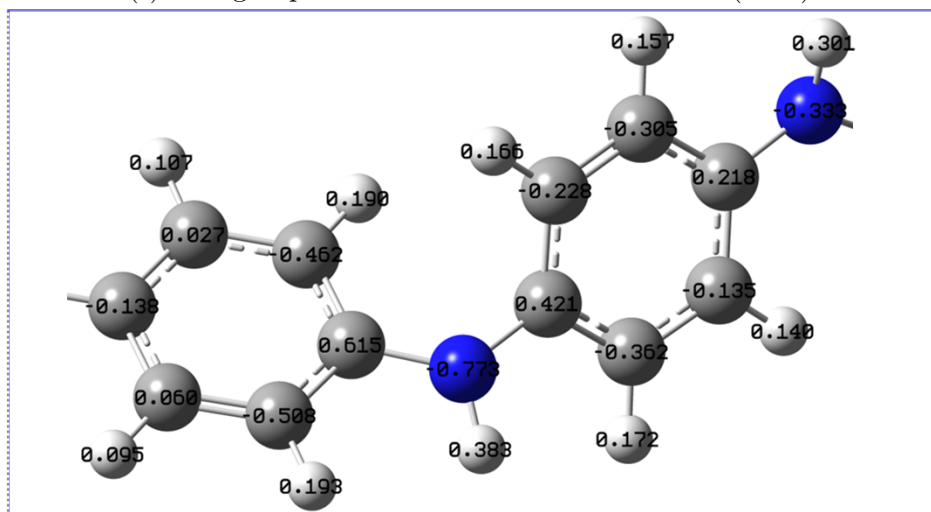


(e) End group 2 of PNB.

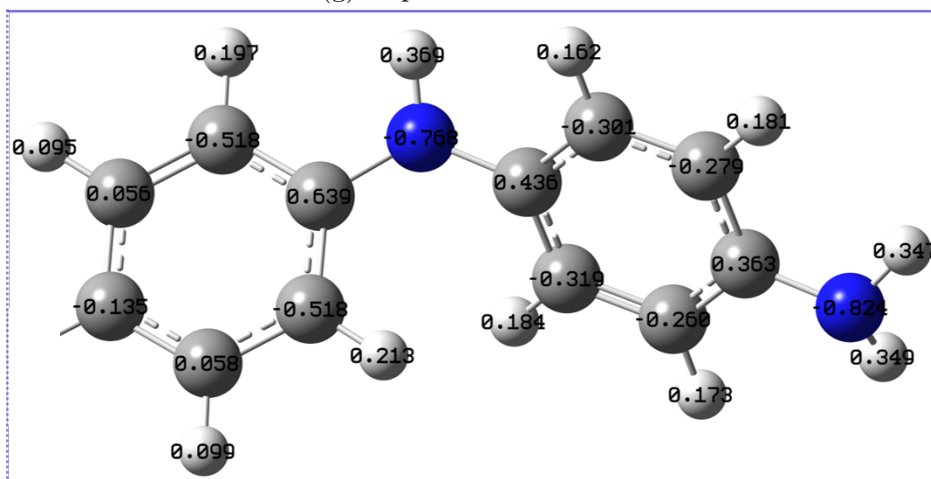
Figure 4.3: RESP charges of species (cont.).



(f) End group 1 of leucoemeraldine base PANI (LEB).

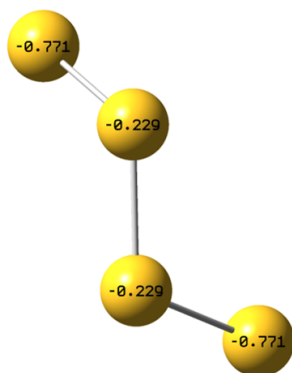


(g) Repeat unit of LEB.

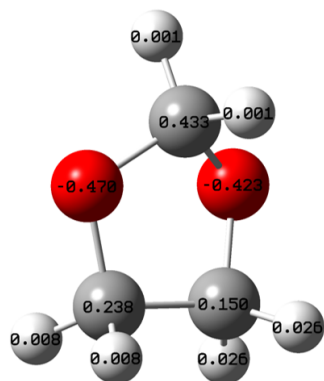


(h) End group 2 of LEB.

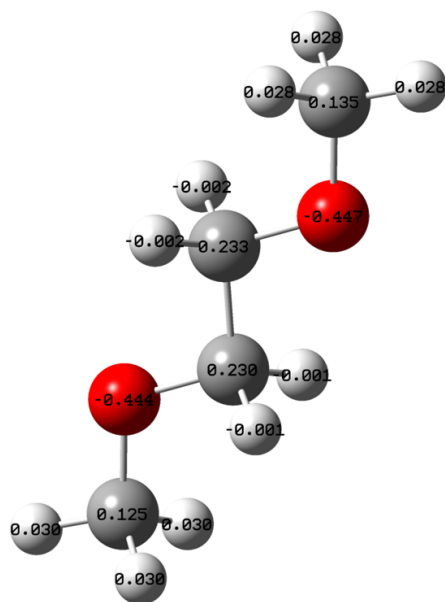
Figure 4.3: RESP charges of species (cont.).



(i) S_4^{2-} .



(j) DOL.



(k) DME.



Figure 4.3: RESP charges of species (cont.).

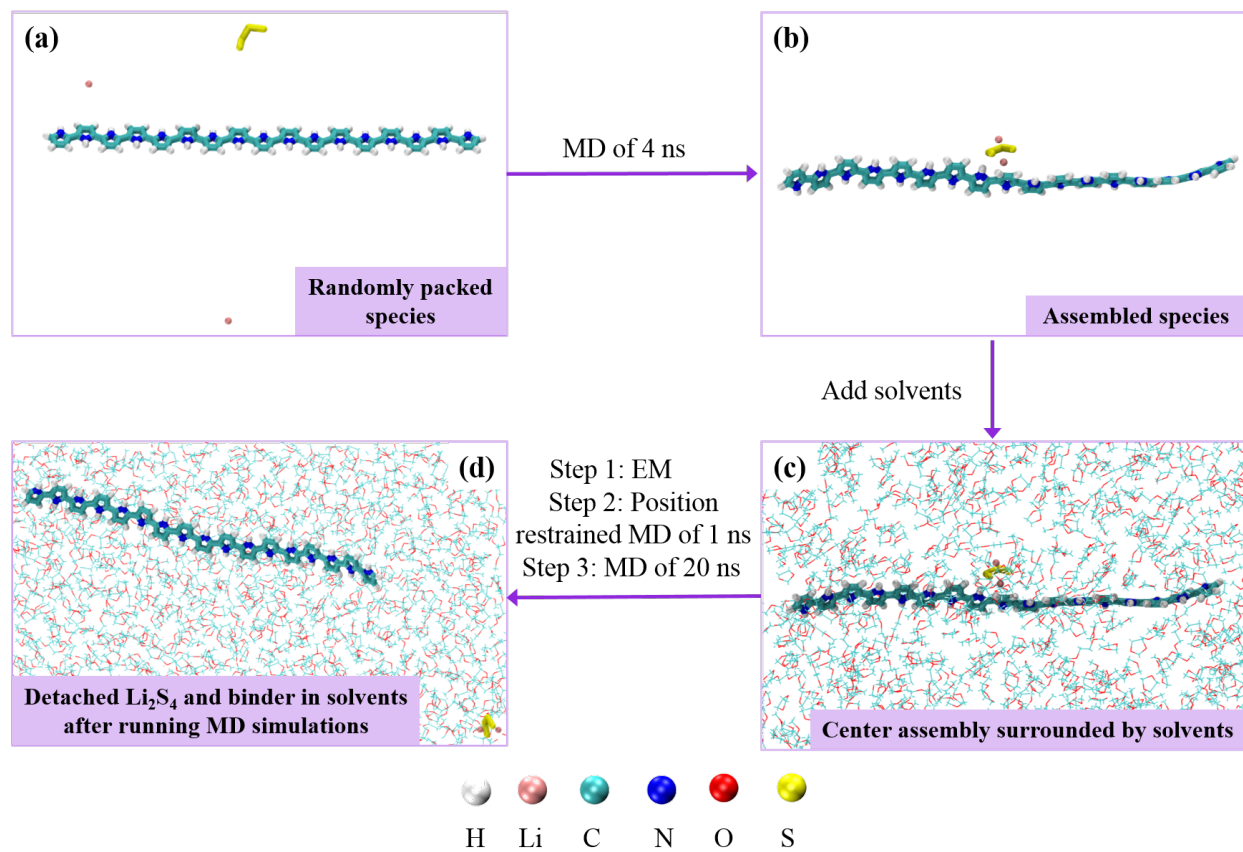


Figure 4.4: Flow diagram of MD simulations and examples of structures of (a) randomly packed PPY, Li^+ and S_4^{2-} , (b) assembled PPY, Li^+ and S_4^{2-} , (c) assembly of PPY, Li^+ and S_4^{2-} surrounded by the DOL/DME solvent mixture, (d) detached Li_2S_4 and PPY in the DOL/DME solvent mixture after running MD simulations. For clarity, the structures of PPY, Li^+ and S_4^{2-} are drawn by ball and stick, while the structures of solvent molecules are represented by fine lines and only some of them are shown. The H, Li, C, N, O and S atoms are colored by white, pink, cyan, blue, red and yellow, respectively.

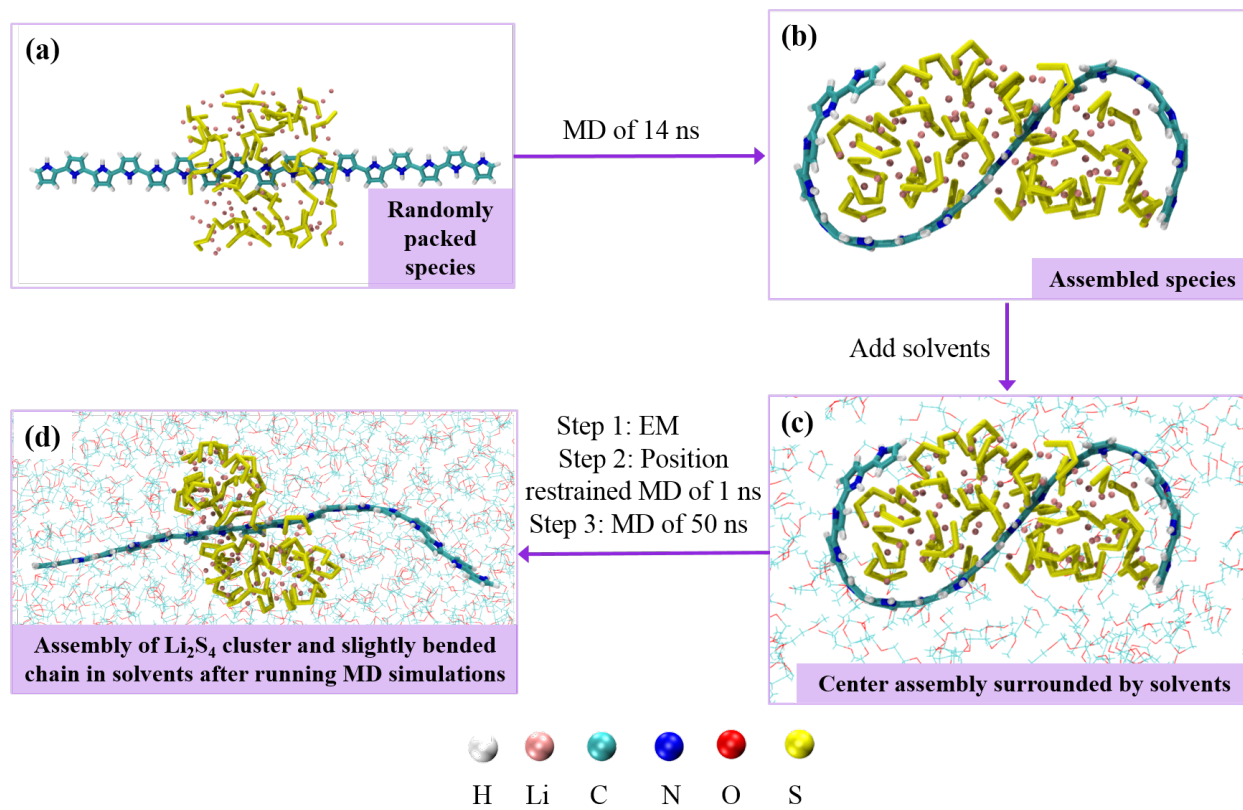


Figure 4.5: Flow diagram of MD simulations and examples of structures of (a) randomly packed PPY, Li⁺ and S₄²⁻, (b) assembled PPY, Li⁺ and S₄²⁻, (c) assembly of PPY, Li⁺ and S₄²⁻ surrounded by the DOL/DME solvent mixture, (d) assembly of Li₂S₄ cluster and slightly bended PPY chain in the DOL/DME solvent mixture after running MD simulations. The color scheme of atoms and the drawing method of molecular structures are the same as that in Figure 4.4.

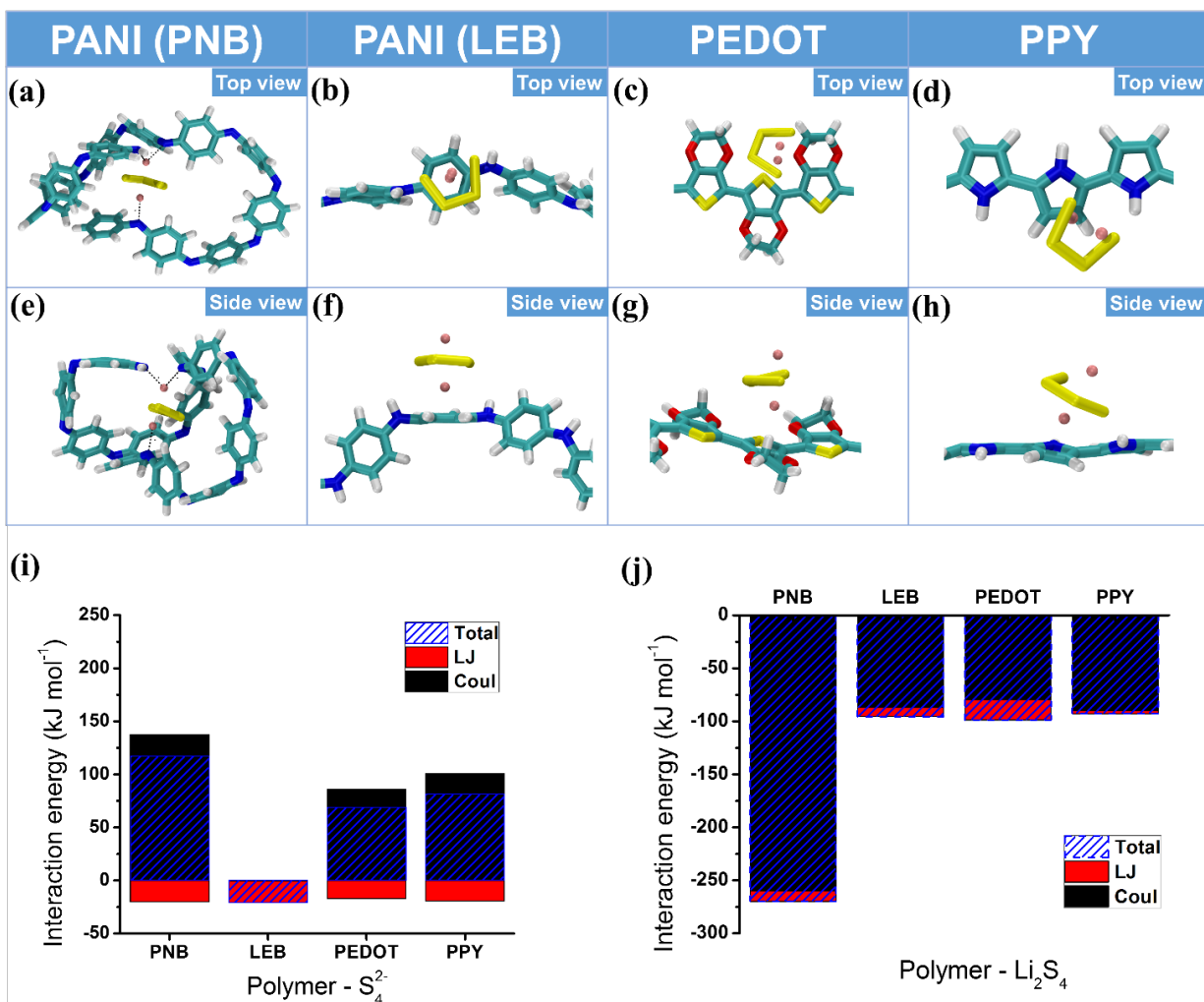


Figure 4.6: (a)-(h) Structure, (i) polymer-S₄²⁻ interaction energy, and (j) polymer-Li₂S₄ interaction energy of the self-assembled single S₄²⁻ dianion, Li⁺ ions and single polymer chain. The color scheme of atoms is the same as that in Figure 4.4. Columns with heights equal to the value of the interaction energy components are stacked up, where the summation is the total interaction energy corresponding to each polymer system.

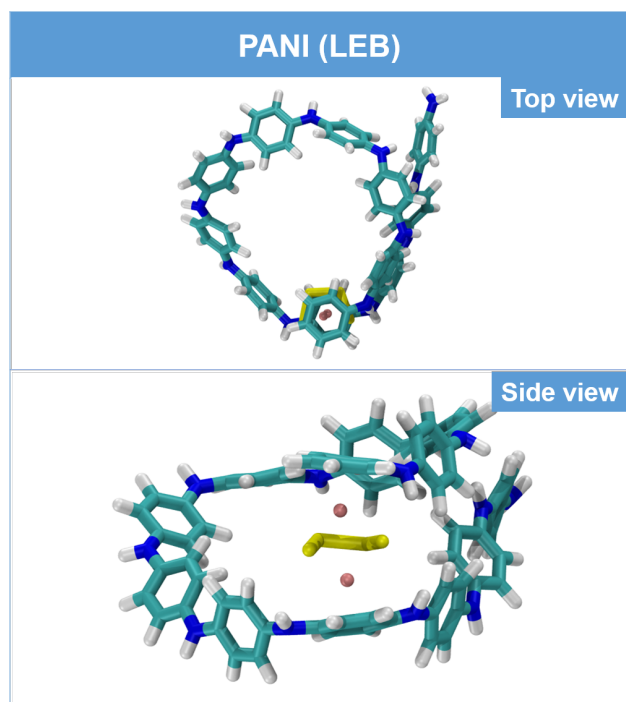


Figure 4.7: Structure of LEB and Li_2S_4 with the strongest Li_2S_4 -LEB interaction. The color scheme of atoms is the same as that in Figure 4.4.

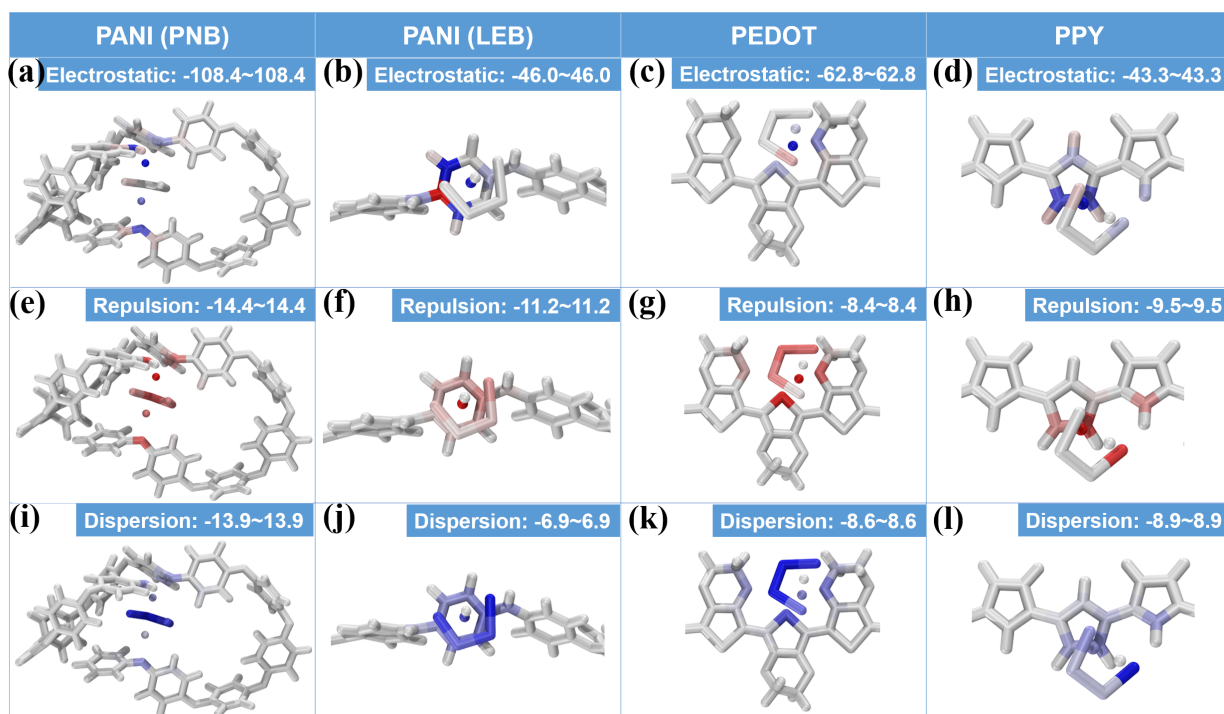


Figure 4.8: Energy decomposition for systems of self-assembled single S_4^{2-} dianion, Li^+ ions and single polymer chain. The atoms are colored by BWR method according to their contributions to each component of Li_2S_4 -polymer interaction energy, where bluer atoms have more negative contribution (*i.e.* more contribution to attraction), redder atoms have more positive contribution (*i.e.* more contribution to repulsion), and whiter atoms have less contribution. The color scales of electrostatic, exchange repulsion and dispersion interactions are noted in each subfigure and the unit is $kJ\ mol^{-1}$. The exchange repulsion is noted as “Repulsion” in subfigures (e)-(h).

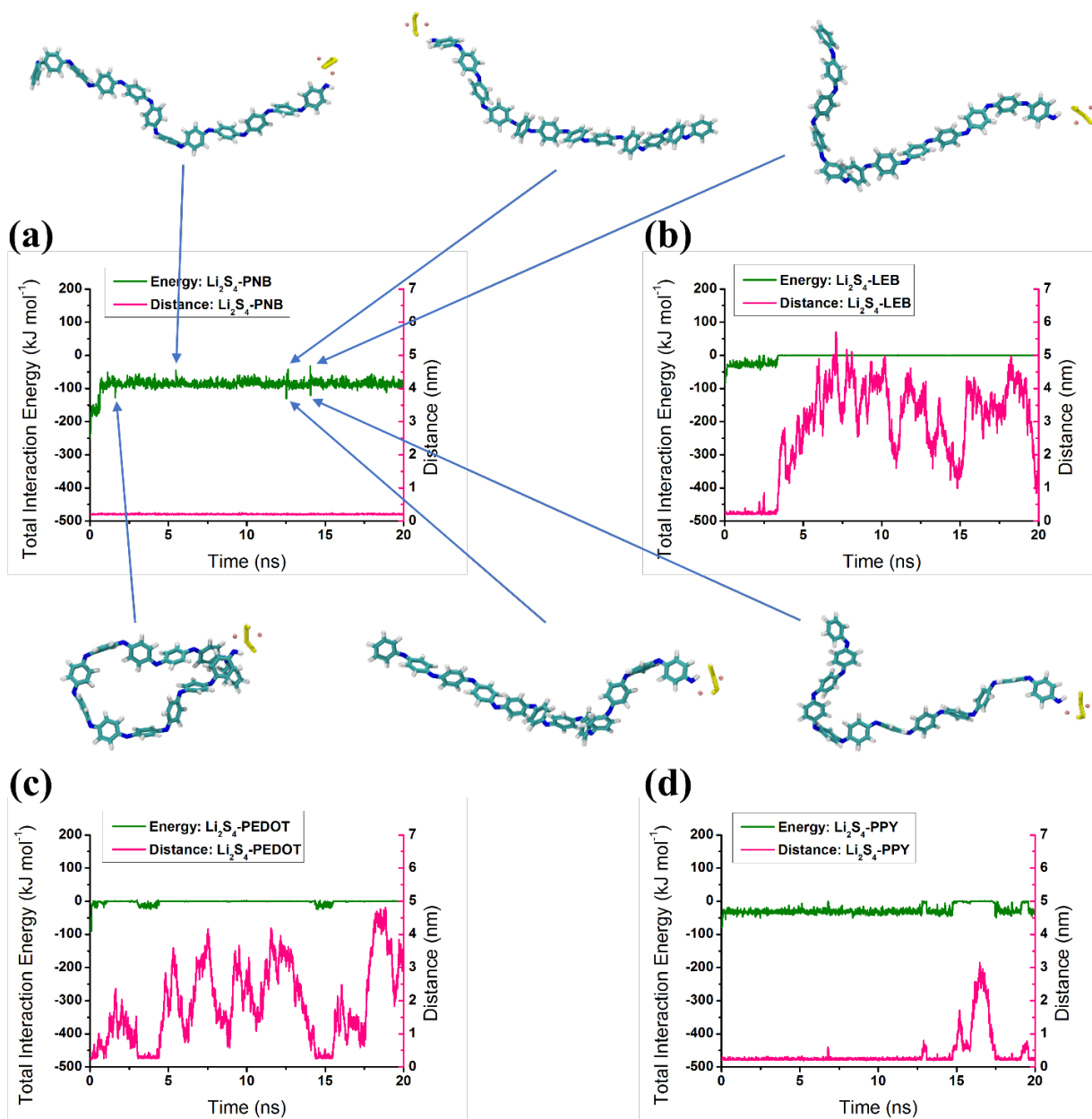
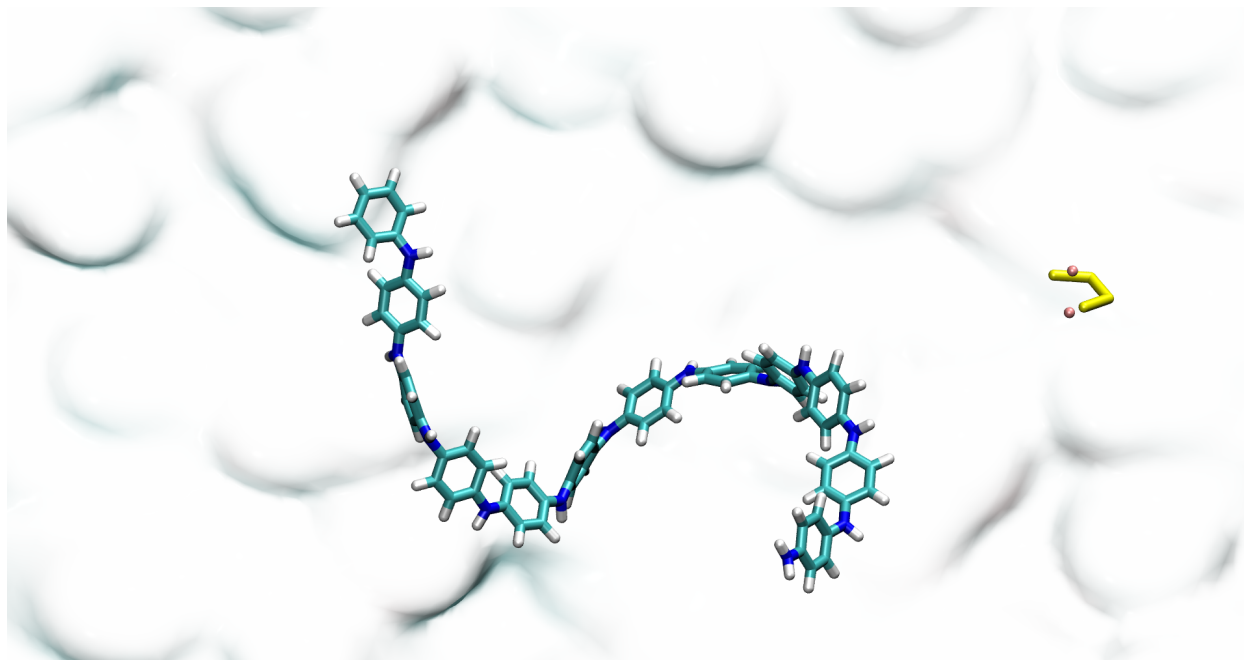
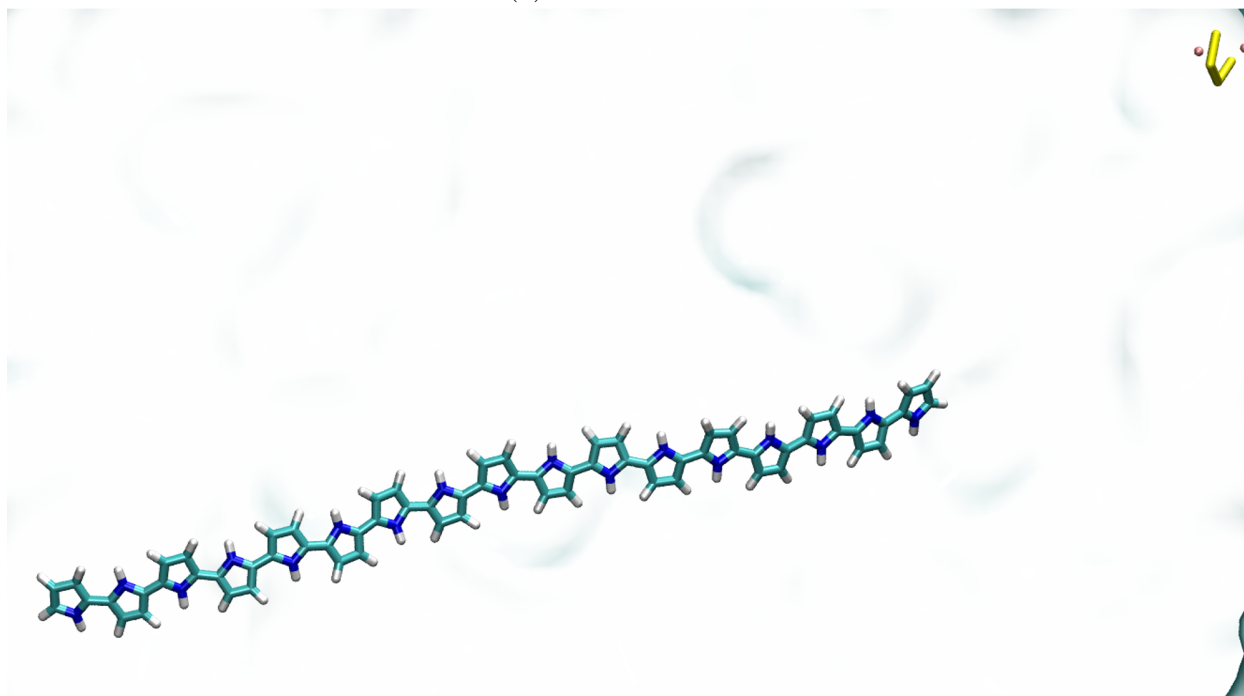


Figure 4.9: Total interaction energy and distance of (a) Li_2S_4 -PNB, (b) Li_2S_4 -LEB, (c) Li_2S_4 -PEDOT, and (d) Li_2S_4 -PPY with the effect of the solvent mixture over time.

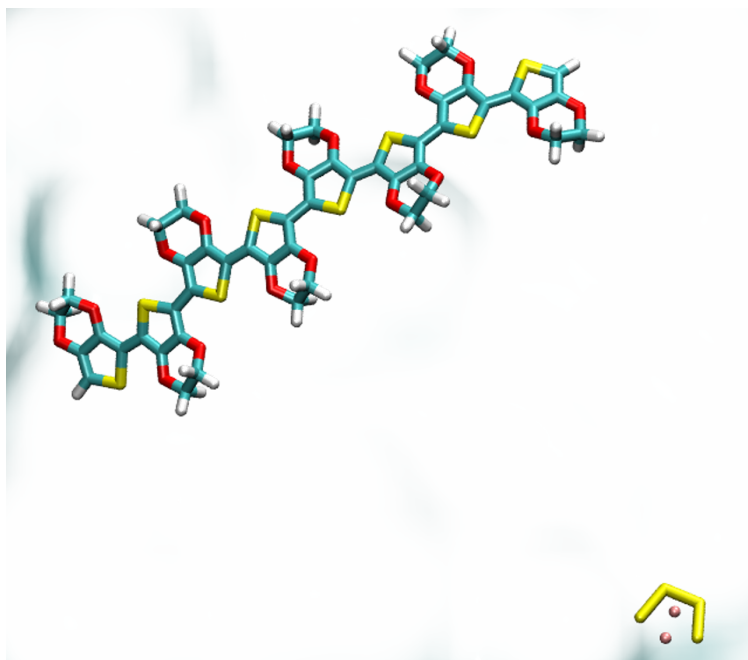


(a) LEB and Li₂S₄.



(b) PPY and Li₂S₄.

Figure 4.10: Detached polymer binder and Li₂S₄ with the effect of the solvent mixture. For clarity, the solvent mixture is drawn as the blue background using QuickSurf method provided in VMD.



(c) PEDOT and Li_2S_4 .

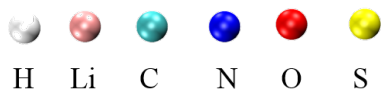


Figure 4.10: Detached polymer binder and Li_2S_4 with the effect of the solvent (cont.). For clarity, the solvent mixture is drawn as the blue background using QuickSurf method provided in VMD.

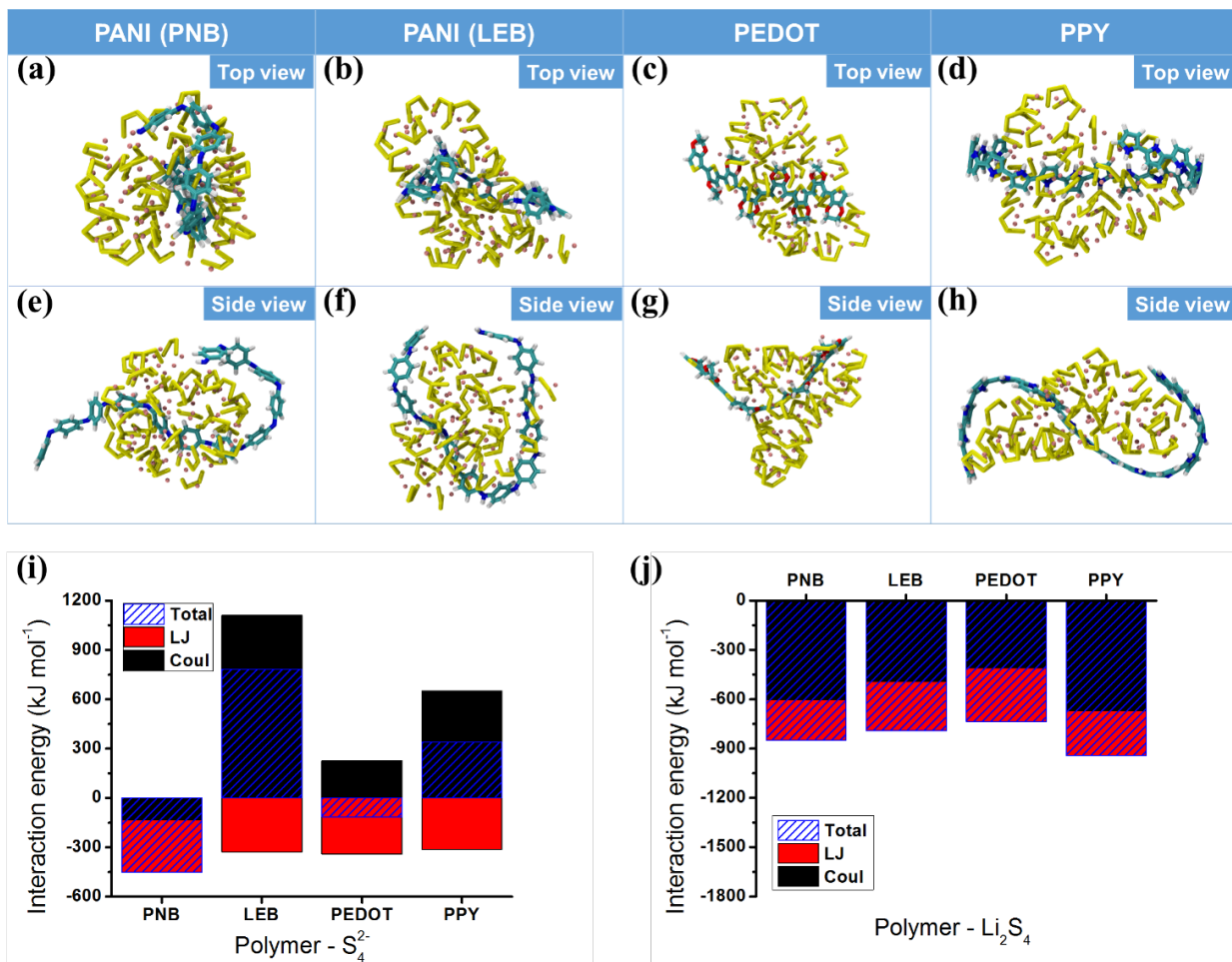


Figure 4.11: (a)-(h) Structure, (i) polymer-S₄²⁻ interaction energy, and (j) polymer-Li₂S₄ interaction energy of the self-assembled multiple S₄²⁻, Li⁺ and single polymer chain. The color scheme of atoms is the same as that in Figure 4.4. Columns with heights equal to the value of the interaction energy components are stacked up, where the summation is the total interaction energy corresponding to each polymer.

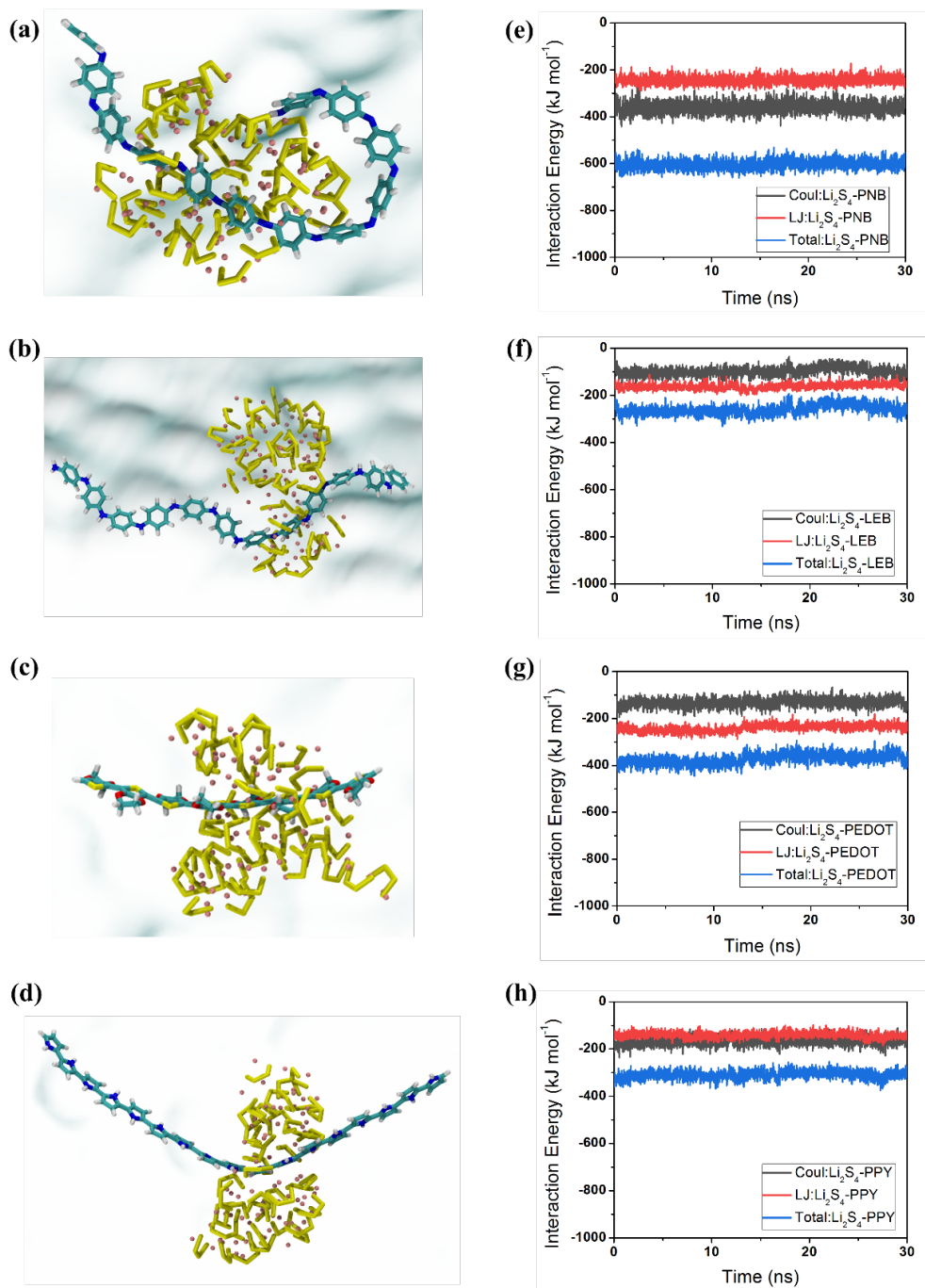
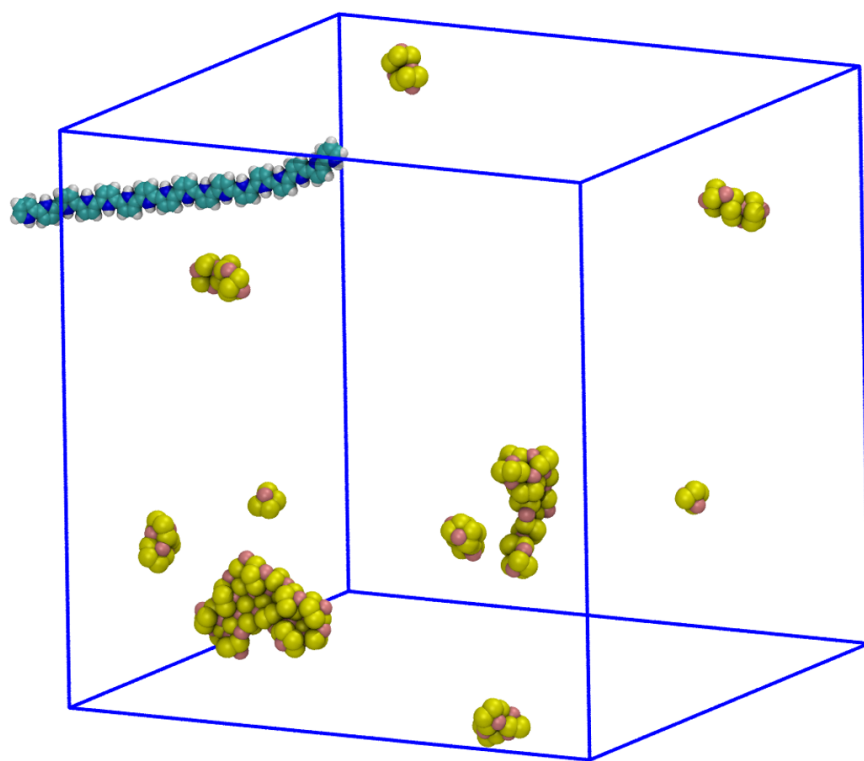


Figure 4.12: Structure of (a) PNB, (b) LEB, (c) PEDOT, and (d) PPY and cluster of Li_2S_4 with the effect of the solvent mixture after running the MD of 50 ns. For clarity, the solvent mixture is drawn as the blue background using QuickSurf method provided in VMD. (e)-(h) Interaction energies of polymer- Li_2S_4 over the last 30 ns of the MD simulations.



Cluster size (Number of atoms)	Number of clusters
6	2
12	1
18	5
60	1
84	1

Figure 4.13: Representative simulation snapshot of PPY and randomly distributed Li_2S_4 clusters in the DOL/DME solvent mixture. Solvents are not shown. The color scheme of atoms is the same as that in Figure 4.4.

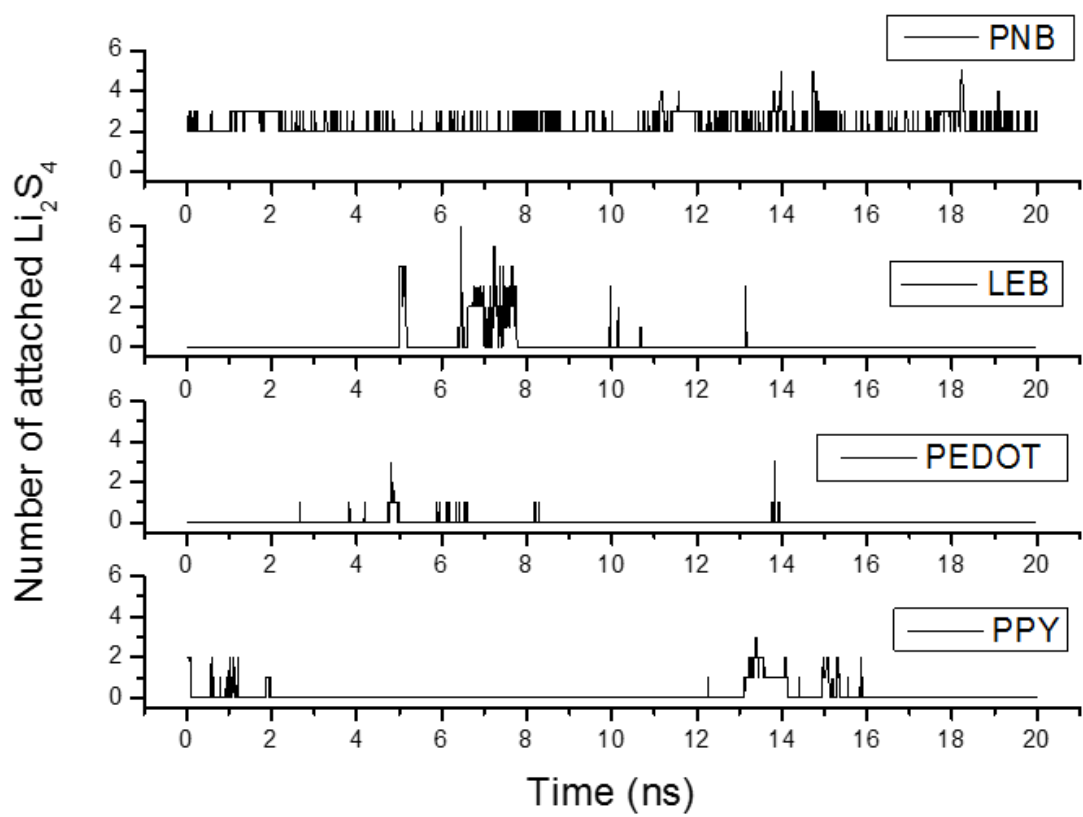


Figure 4.14: Numbers of Li_2S_4 within 5 \AA of binders at different time points during the last 20 ns of the MD simulations.

Chapter 5

Conclusion

Due to the current advances in computational resources and techniques, computational materials science is increasingly applied to predict the relationship between material structures, properties and performance. One of the challenges is how to properly build models using the available resources and approaches.

In one application, NaS batteries with large diameter are desired for commercialization. But the seals in the joint region and the BASE component of the cell are relatively vulnerable and serious thermo-mechanical stress accumulation can be induced by increasing the NaS cell diameter during the cell assembly, operation and maintenance, which may result in the fracture of the cell and the following serious safety issues. Different container materials with different CTEs and other thermo-mechanical properties have been selected and conceived for circumventing the problem of thermo-mechanical stress accumulation. In the present study, the thermo-mechanical stress concentrated region in different cells with different container materials have been estimated and the shear and normal stresses in these regions have been quantified using the FEA computation technique. It is demonstrated that the primary failure mechanism in the planar NaS system design considered in the current work would be the interfacial fracture between the insulating header (IH) and the upper insert metal (IM1) due to the normal stress in cell height direction, and the necessary treatments, including better

material selection or improved bonding technology between IH and IM1, must be involved to avoid the fractures of constituent components in the joint area.

In another application, a series of MD computations was conducted to evaluate the Flory-Huggins parameters (χ) between TC drugs and PLA/PGA polymers. By quantifying χ values between PLA and PGA blend systems, it is shown that the mixing of PLA and PGA polymers is not thermodynamically favorable throughout the entire composition range of 10/90 to 90/10 wt% PLA/PGA. Then the χ parameters between PLA and/or PGA polymers and TC drugs are estimated for the TC compositions of 15 and 45 wt%. Based on the thermodynamics considerations using the Flory-Huggins solution model, the free energy densities for these PLA/TC and PGA/TC systems are studied and they are correlated to the surface structural morphology of PLGA/TC films. The meso-scale modeling based on PFM method using the material properties obtained through MD computations was then conducted, and it is found that the overall size distributions of drug particles embedded in PLGA matrices with different PLA/PGA copolymer ratios are comparable to the experimental observations. It is thought that such variations of drug particle sizes can directly influence the drug release kinetics from PLGA-TC coatings.

Finally, full atomistic MD simulations have been performed on tetra-sulfides and undoped conjugated polymers PNB, LEB, PEDOT and PPY to investigate the binding effectiveness between polysulfides and polymer binders. The weight ratio between sulfur and binder in lithium-sulfur cells is considered in 1:1 v/v mixture of dioxolane/dimethoxyethane. The simulations reveal that the end group 2 of PNB can effectively bind a lithium tetra-sulfide (*i.e.* Li_2S_4) cluster or 2 out of 43 Li_2S_4 molecules with the effect of solvent. However, repeat units of PNB, LEB, PEDOT and PPY seem ineffective in binding solvated Li_2S_4 through non-bonded interaction, especially when the concentration of tetra-sulfide/binder in a local domain of the cathode is low. Therefore, polymers with this specific functional group (*i.e.* the end group 2 of PNB) are suggested to be further studied as potential effective binders to inhibit the shuttle effect of solvated lithium polysulfides. Also, since the solvent

has considerable impact on the binding effectiveness between tetra-sulfides and binder, it is suggested to take advantage of the explicit solvation models, such as those built in this work, to predict how other influencing factors affect binding between polysulfides and polymers.

The presented simulation models demonstrate the application of computational materials science in material system development in energy storage material and biological materials. The modeling methods can be employed and extended for solving similar practical problems, including material design and performance analysis.

Bibliography

- [1] Peter L Freddolino, Christopher B Harrison, Yanxin Liu, and Klaus Schulten. Challenges in protein-folding simulations. *Nature Physics*, 6(10):751, 2010.
- [2] Daan Frenkel and Berend Smit. *Understanding molecular simulation: from algorithms to applications*, volume 1. Elsevier, 2001.
- [3] Pierre Hohenberg and Walter Kohn. Inhomogeneous electron gas. *Physical Review*, 136(3B):B864, 1964.
- [4] Walter Kohn and Lu Jeu Sham. Self-consistent equations including exchange and correlation effects. *Physical Review*, 140(4A):A1133, 1965.
- [5] Arieh Warshel and Michael Levitt. Theoretical studies of enzymic reactions: dielectric, electrostatic and steric stabilization of the carbonium ion in the reaction of lysozyme. *Journal of Molecular Biology*, 103(2):227–249, 1976.
- [6] Thomas Heine. Grand challenges in computational materials science: from description to prediction at all scales. *Frontiers in Materials*, 1:7, 2014.
- [7] James Sudworth and AR Tiley. *Sodium Sulphur Battery*. Springer Science & Business Media, 1985.
- [8] Bruce Dunn, Haresh Kamath, and Jean-Marie Tarascon. Electrical energy storage for the grid: a battery of choices. *Science*, 334(6058):928–935, 2011.

- [9] Zhenguo Yang, Jianlu Zhang, Michael CW Kintner-Meyer, Xiaochuan Lu, Daiwon Choi, John P Lemmon, and Jun Liu. Electrochemical energy storage for green grid. *Chemical Reviews*, 111(5):3577–3613, 2011.
- [10] Brian L Ellis and Linda F Nazar. Sodium and sodium-ion energy storage batteries. *Current Opinion in Solid State and Materials Science*, 16(4):168–177, 2012.
- [11] Karina B Hueso, Michel Armand, and Teófilo Rojo. High temperature sodium batteries: status, challenges and future trends. *Energy & Environmental Science*, 6(3):734–749, 2013.
- [12] Xiaochuan Lu, Brent W Kirby, Wu Xu, Guosheng Li, Jin Y Kim, John P Lemmon, Vincent L Sprenkle, and Zhenguo Yang. Advanced intermediate-temperature Na–S battery. *Energy & Environmental Science*, 6(1):299–306, 2013.
- [13] Xiaochuan Lu, Guosheng Li, Jin Y Kim, Donghai Mei, John P Lemmon, Vincent L Sprenkle, and Jun Liu. Liquid-metal electrode to enable ultra-low temperature sodium–beta alumina batteries for renewable energy storage. *Nature Communications*, 5:4578, 2014.
- [14] Cheol-Wan Park, Jou-Hyeon Ahn, Ho-Suk Ryu, Ki-Won Kim, and Hyo-Jun Ahn. Room-temperature solid-state sodium/ sulfur battery. *Electrochemical and Solid-State Letters*, 9(3):A123–A125, 2006.
- [15] Tae Hoon Hwang, Dae Soo Jung, Joo-Seong Kim, Byung Gon Kim, and Jang Wook Choi. One-dimensional carbon–sulfur composite fibers for Na–S rechargeable batteries operating at room temperature. *Nano Letters*, 13(9):4532–4538, 2013.
- [16] Sen Xin, Ya-Xia Yin, Yu-Guo Guo, and Li-Jun Wan. A high-energy room-temperature sodium-sulfur battery. *Advanced Materials*, 26(8):1261–1265, 2014.

- [17] Icpyo Kim, Jin-Young Park, Chang Hyeon Kim, Jin-Woo Park, Jae-Pyoung Ahn, Jou-Hyeon Ahn, Ki-Won Kim, and Hyo-Jun Ahn. A room temperature Na/S battery using a β'' alumina solid electrolyte separator, tetraethylene glycol dimethyl ether electrolyte, and a S/C composite cathode. *Journal of Power Sources*, 301:332–337, 2016.
- [18] Xiaochuan Lu, John P Lemmon, Jin Y Kim, Vincent L Sprenkle, and Zhenguo Yang. High energy density Na–S/NiCl₂ hybrid battery. *Journal of Power Sources*, 224:312–316, 2013.
- [19] LTD NGK Insulators. The world’s largest NaS battery installation commences operation short installation period achieved through containerized, compact format. <http://www.ngk.co.jp/english/news/2016/0303.html>, 2016. [Online; accessed 26-Jan-2017].
- [20] Zhaoyin Wen, Zhonghua Gu, Xiaohe Xu, Jiadi Cao, Fuli Zhang, and Zuxiang Lin. Research activities in shanghai institute of ceramics, chinese academy of sciences on the solid electrolytes for sodium sulfur batteries. *Journal of Power Sources*, 184(2): 641–645, 2008.
- [21] Wei Shi, Jiuchun Jiang, Suoyu Li, Siqi Lin, Peifeng Lin, and Feng Wen. Applications of battery energy storage system (BESS) for energy conversion base in expo 2010. In *Power Electronics for Distributed Generation Systems (PEDG), 2010 2nd IEEE International Symposium*, pages 918–923. IEEE, 2010.
- [22] Zhaoyin Wen, Yingying Hu, Xiangwei Wu, Jinduo Han, and Zhonghua Gu. Main challenges for high performance NaS battery: materials and interfaces. *Advanced Functional Materials*, 23(8):1005–1018, 2013.
- [23] June Kee Min and Chang-Hui Lee. Numerical study on the thermal management system of a molten sodium–sulfur battery module. *Journal of Power Sources*, 210: 101–109, 2012.

- [24] Keeyoung Jung, Solki Lee, Yoon-Cheol Park, and Chang-Soo Kim. Finite element analysis study on the thermomechanical stability of thermal compression bonding (tcb) joints in tubular sodium sulfur cells. *Journal of Power Sources*, 250:1–14, 2014.
- [25] Keeyoung Jung, Solki Lee, Goun Kim, and Chang-Soo Kim. Stress analyses for the glass joints of contemporary sodium sulfur batteries. *Journal of Power Sources*, 269:773–782, 2014.
- [26] Keeyoung Jung, Hoe-Jun Heo, Ju-Hyeok Lee, Yoon-Cheol Park, and Chung-Yun Kang. Enhanced corrosion resistance of hypo-eutectic Al–1Mg–xSi alloys against molten sodium attack in high temperature sodium sulfur batteries. *Corrosion Science*, 98:748–757, 2015.
- [27] June Kee Min, Michael Stackpool, Cheol Ho Shin, and Chang-Hui Lee. Cell safety analysis of a molten sodium–sulfur battery under failure mode from a fracture in the solid electrolyte. *Journal of Power Sources*, 293:835–845, 2015.
- [28] I Wynn Jones. Recent advances in the development of sodium–sulphur batteries for load levelling and motive power applications. In *International Symposium on Solid Ionic and Ionic-Electronic Conductors*, pages 681–688. Elsevier, 1977.
- [29] Goun Kim, Yoon-Cheol Park, Younki Lee, Namung Cho, Chang-Soo Kim, and Keeyoung Jung. The effect of cathode felt geometries on electrochemical characteristics of sodium sulfur (NaS) cells: Planar vs. tubular. *Journal of Power Sources*, 325:238–245, 2016.
- [30] HP Silverman, LS Marcoux, and ET Seo. Development program for solid-electrolyte batteries. Final report. Technical report, TRW Defense and Space Systems Group, Redondo Beach, CA (USA), 1976.
- [31] Albert A Koenig and James R Rasmussen. Development of a high specific power

- sodium sulfur cell. In *Power Sources Symposium, 1990., Proceedings of the 34th International*, pages 30–33. IEEE, 1990.
- [32] Richard P Sernka and Robert K Taenaka. Planar sodium–sulfur electrical storage cell, October 1 1991. US Patent 5,053,294.
- [33] Jin Y Kim, Nathan L Canfield, Jeff F Bonnett, Vincent L Sprenkle, Keeyoung Jung, and Inchul Hong. A duplex β – Al_2O_3 solid electrolyte consisting of a thin dense layer and a porous substrate. *Solid State Ionics*, 278:192–197, 2015.
- [34] Keeyoung Jung, Jeffrey P Colker, Yuzhe Cao, Goun Kim, Yoon-Cheol Park, and Chang-Soo Kim. A thermo-mechanical stress prediction model for contemporary planar sodium sulfur (NaS) cells. *Journal of Power Sources*, 324:665–673, 2016.
- [35] Gege Tao, Neill Weber, and Anil V Virkar. Planar alkali metal-beta battery, January 15 2015. US Patent App. 13/938,165.
- [36] LLC EaglePicher Technologies. Planar sodium-beta batteries for renewable integration and grid applications. In *ARPA-E Energy Innovation Summit, Washington DC*, 2015.
- [37] Keeyoung Jung, Yoon-Cheol Park, Sun-Hong Park, Changhui Lee, Munkyu Cho, Goun Kim, Younki Lee, Ju Hyeok Lee, Sung Wun Cheon, Soon Cheol Hwang, et al. Development of a planar sodium sulfur cell. In *Meeting Abstracts*, number 9, pages 622–622. The Electrochemical Society, 2014.
- [38] Tsann-Shyi Chern and Hsien-Lung Tsai. Wetting and sealing of interface between 7056 Glass and Kovar alloy. *Materials Chemistry and Physics*, 104(2-3):472–478, 2007.
- [39] Morsy Amin Morsy, Kenji Ikeuchi, Masao Ushio, and Hideyuki Abe. Mechanism of enlargement of intimately contacted area in anodic bonding of Kovar alloy to borosilicate glass. *Materials Transactions, JIM*, 37(9):1511–1517, 1996.

- [40] C Chanmuang, M Naksata, T Chairuangri, H Jain, and CE Lyman. Microscopy and strength of borosilicate glass-to-Kovar alloy joints. *Materials Science and Engineering: A*, 474(1-2):218–224, 2008.
- [41] Katsuaki Sukanuma, Taira Okamoto, and K Kamachi. Influence of shape and size on residual stress in ceramic/metal joining. *Journal of Materials Science*, 22(8):2702–2706, 1987.
- [42] Armando Zanchetta, Pierre Lefort, and Emile Gabbay. Thermal expansion and adhesion of ceramic to metal sealings: case of porcelain-kovar junctions. *Journal of the European Ceramic Society*, 15(3):233–238, 1995.
- [43] GJ Qiao, CG Zhang, and ZH Jin. Thermal cyclic test of alumina/kovar joint brazed by Ni–Ti active filler. *Ceramics International*, 29(1):7–11, 2003.
- [44] C Moosbrugger. Atlas of stress-strain curves. *ASM International, Ohio*, 2002.
- [45] Il-Ho Kim, Ha-Geun Kim, Sang-Beom Shin, and Dong-Hwan Park. A study on welding distortion of GTA circular type lap joint in STS304L thin plate. *Journal of Welding and Joining*, 30(5):57–63, 2012.
- [46] RK Blandford, DK Morton, SD Snow, and TE Rahl. Tensile stress-strain results for 304L and 316L stainless steel plate at temperature. In *ASME 2007 Pressure Vessels and Piping Conference*, pages 617–628. American Society of Mechanical Engineers, 2007.
- [47] Kyo-Kook Jin, Byung-Taek Oh, Young-Kyun Kim, Ihn-Soo Yoon, and Young-Chul Yang. An assessment of structure safety for basic insulation panel of KC-1 LNG cargo containment system under sloshing load. *Journal of the Korean Institute of Gas*, 17(2):85–89, 2013.

- [48] Fatma Ben Saada, Zied Antar, Khaled Elleuch, and Pierre Ponthiaux. On the tribo-corrosion behavior of 304L stainless steel in olive pomace/tap water filtrate. *Wear*, 328:509–517, 2015.
- [49] DL Thornburg, ES Thall, and J Brous. A manual of materials for microwave tubes. Technical report, RADIO CORP OF AMERICA HARRISON NJ, 1961.
- [50] MA Salama, WM Rowe, and RK Yasui. Thermoelastic analysis of solar cell arrays and their material properties. Technical report, 1973.
- [51] Kwang Seok Lee, Dong Hyun Yoon, Joong Eun Jung, Young Won Chang, and Jung Hwan Lee. High-temperature deformation behavior and thermal properties of an Ni₃₀Co₁₇Fe₅₃ alloy. *International Journal of Materials Research*, 103(7):821–827, 2012.
- [52] MK Neilsen, SN Burchett, CM Stone, and JJ Stephens. A viscoplastic theory for braze alloys. Technical report, 1996.
- [53] Toshihiro Yamada, Motohiro Satoh, Akiomi Kohno, and Kazuaki Yokoi. Residual stress estimation of a silicon carbide-Kovar joint. *Journal of Materials Science*, 26(11):2887–2892, 1991.
- [54] Angelo Meduri, Tiziana Fuoco, Marina Lamberti, Claudio Pellecchia, and Daniela Pappalardo. Versatile copolymerization of glycolide and rac-lactide by dimethyl (sali-cylaldiminato) aluminum compounds. *Macromolecules*, 47(2):534–543, 2014.
- [55] Jian Li, Ryan M Stayshich, and Tara Y Meyer. Exploiting sequence to control the hydrolysis behavior of biodegradable plga copolymers. *Journal of the American Chemical Society*, 133(18):6910–6913, 2011.
- [56] Frank Alexis. Factors affecting the degradation and drug-release mechanism of poly

- (lactic acid) and poly [(lactic acid)-co-(glycolic acid)]. *Polymer International*, 54(1): 36–46, 2005.
- [57] Chhaya Engineer, Jigisha Parikh, and Ankur Raval. Review on hydrolytic degradation behavior of biodegradable polymers from controlled drug delivery system. *Trends in Biomaterials & Artificial Organs*, 25(2), 2011.
- [58] Hirenkumar K Makadia and Steven J Siegel. Poly lactic-co-glycolic acid (plga) as biodegradable controlled drug delivery carrier. *Polymers*, 3(3):1377–1397, 2011.
- [59] Sonam, Hema Chaudhary, Vimal Arora, Kanchan Kholi, and Vikash Kumar. Effect of physicochemical properties of biodegradable polymers on nano drug delivery. *Polymer Reviews*, 53(4):546–567, 2013.
- [60] ML Hans and AM Lowman. Biodegradable nanoparticles for drug delivery and targeting. *Current Opinion in Solid State and Materials Science*, 6(4):319–327, 2002.
- [61] Ghanashyam Acharya, Crystal S Shin, Kumar Vedantham, Matthew McDermott, Thomas Rish, Keith Hansen, Yourong Fu, and Kinam Park. A study of drug release from homogeneous plga microstructures. *Journal of Controlled Release*, 146(2): 201–206, 2010.
- [62] Juergen Siepmann, Khaled Elkharraz, Florence Siepmann, and Diana Klose. How autocatalysis accelerates drug release from plga-based microparticles: a quantitative treatment. *Biomacromolecules*, 6(4):2312–2319, 2005.
- [63] Juergen Siepmann, N Faisant, J Akiki, J Richard, and JP Benoit. Effect of the size of biodegradable microparticles on drug release: experiment and theory. *Journal of Controlled Release*, 96(1):123–134, 2004.
- [64] Jiyeon Choi, Bu Nam Jang, Bang Ju Park, Yoon Ki Joung, and Dong Keun Han.

- Effect of solvent on drug release and a spray-coated matrix of a sirolimus-eluting stent coated with poly (lactic-co-glycolic acid). *Langmuir*, 30(33):10098–10106, 2014.
- [65] Haitao Qian, Adam R Wohl, Jordan T Crow, Christopher W Macosko, and Thomas R Hoye. A strategy for control of “random” copolymerization of lactide and glycolide: application to synthesis of peg-b-plga block polymers having narrow dispersity. *Macromolecules*, 44(18):7132–7140, 2011.
- [66] Martin K McDermott, David M Saylor, Rachel Casas, Benita J Dair, Ji Guo, Chang-Soo Kim, Christine M Mahoney, Kokyee Ng, Steven K Pollack, Dinesh V Patwardhan, et al. Microstructure and elution of tetracycline from block copolymer coatings. *Journal of Pharmaceutical Sciences*, 99(6):2777–2785, 2010.
- [67] S Govender, D Lutchman, V Pillay, DJ Chetty, and T Govender. Enhancing drug incorporation into tetracycline-loaded chitosan microspheres for periodontal therapy. *Journal of Microencapsulation*, 23(7):750–761, 2006.
- [68] Rajesh K Agarwal, Dennis H Robinson, Glenn I Maze, and Richard A Reinhardt. Development and characterization of tetracycline-poly (lactide/glycolide) films for the treatment of periodontitis. *Journal of Controlled Release*, 23(2):137–146, 1993.
- [69] Priyadharsini Karuppuswamy, Jayarama Reddy Venugopal, Balchandar Navaneethan, Ashang Luwang Laiva, and Seeram Ramakrishna. Polycaprolactone nanofibers for the controlled release of tetracycline hydrochloride. *Materials Letters*, 141:180–186, 2015.
- [70] David M Saylor, Christopher Forrey, Chang-Soo Kim, and James A Warren. Diffuse interface methods for modeling drug-eluting stent coatings. *Annals of Biomedical Engineering*, 44(2):548–559, 2016.
- [71] Mingzong Zhang, Phillip Choi, and Uttandaraman Sundararaj. Molecular dynamics and thermal analysis study of anomalous thermodynamic behavior of poly (ether imide)/polycarbonate blends. *Polymer*, 44(6):1979–1986, 2003.

- [72] Sheetal S Jawalkar and Tejraj M Aminabhavi. Molecular modeling simulations and thermodynamic approaches to investigate compatibility/incompatibility of poly (l-lactide) and poly (vinyl alcohol) blends. *Polymer*, 47(23):8061–8071, 2006.
- [73] Amar K Mohanty, Manjusri Misra, Lawrence Thaddeus Drzal, et al. Natural fibers, biopolymers, and biocomposites. 2005.
- [74] Arfan Subhani. *Influence of the processes parameters on the properties of the polylactides based bio and eco-biomaterials*. PhD thesis, INPT, 2011.
- [75] Sigma-Aldrich. Polyglycolide. <http://www.sigmaaldrich.com/catalog/product/aldrich/457620?lang=en®ion=US>. [Online; accessed 23-Dec-2015].
- [76] Fatima Varanda, Maria J Pratas de Melo, Ana I Caco, Ralf Dohrn, Foteini A Makrydaki, Epaminondas Voutsas, Dimitrios Tassios, and Isabel M Marrucho. Solubility of antibiotics in different solvents. 1. hydrochloride forms of tetracycline, moxifloxacin, and ciprofloxacin. *Industrial & Engineering Chemistry Research*, 45(18):6368–6374, 2006.
- [77] Huai Sun. COMPASS: an ab initio force-field optimized for condensed-phase applications overview with details on alkane and benzene compounds. *The Journal of Physical Chemistry B*, 102(38):7338–7364, 1998.
- [78] Michael J McQuaid, Huai Sun, and David Rigby. Development and validation of COMPASS force field parameters for molecules with aliphatic azide chains. *Journal of Computational Chemistry*, 25(1):61–71, 2004.
- [79] Long-Qing Chen. Phase-field models for microstructure evolution. *Annual Review of Materials Research*, 32(1):113–140, 2002.
- [80] Paul J Flory. Thermodynamics of high polymer solutions. *Journal of Chemical Physics*, 10(1):51–61, 1942.

- [81] Maurice L Huggins. Solutions of long chain compounds. *Journal of Chemical Physics*, 9(5):440–440, 1941.
- [82] John W Cahn and John E Hilliard. Free energy of a nonuniform system. i. interfacial free energy. *Journal of Chemical Physics*, 28(2):258–267, 1958.
- [83] David M Saylor, Chang-Soo Kim, Dinesh V Patwardhan, and James A Warren. Diffuse-interface theory for structure formation and release behavior in controlled drug release systems. *Acta Biomaterialia*, 3(6):851–864, 2007.
- [84] Zhonglin Luo and Jianwen Jiang. Molecular dynamics and dissipative particle dynamics simulations for the miscibility of poly (ethylene oxide)/poly (vinyl chloride) blends. *Polymer*, 51(1):291–299, 2010.
- [85] Inger Martinez de Arenaza, Emilio Meaurio, Borja Coto, and Jose-Ramon Sarasua. Molecular dynamics modelling for the analysis and prediction of miscibility in polylactide/polyvinylphenol blends. *Polymer*, 51(19):4431–4438, 2010.
- [86] Abhishek Agrawal, Amit D Saran, Swagat S Rath, and Ashok Khanna. Constrained nonlinear optimization for solubility parameters of poly (lactic acid) and poly (glycolic acid)—validation and comparison. *Polymer*, 45(25):8603–8612, 2004.
- [87] Michael Hacker. *Functional cell carriers for tissue engineering-fabrication & characterization*. PhD thesis, 2005.
- [88] Tarek M Madkour, Sarah A Salem, and Stephen A Miller. The role of the deformational entropy in the miscibility of polymer blends investigated using a hybrid statistical mechanics and molecular dynamics model. *Physical Chemistry Chemical Physics*, 15(16):5982–5991, 2013.
- [89] John Burke. Solubility parameters: theory and application. 1984.

- [90] Jin Gu and Jeffrey M Catchmark. Polylactic acid composites incorporating casein functionalized cellulose nanowhiskers. *Journal of Biological Engineering*, 7(1):31, 2013.
- [91] Patrick J Marsac, Sheri L Shamblin, and Lynne S Taylor. Theoretical and practical approaches for prediction of drug–polymer miscibility and solubility. *Pharmaceutical Research*, 23(10):2417, 2006.
- [92] Michael Rubinstein and Ralph H Colby. *Polymer physics*, volume 23. Oxford University Press New York, 2003.
- [93] Paul C Painter, John F Graf, and Michael M Coleman. Effect of hydrogen bonding on the enthalpy of mixing and the composition dependence of the glass transition temperature in polymer blends. *Macromolecules*, 24(20):5630–5638, 1991.
- [94] Loan Huynh, Justin Grant, Jean-Christophe Leroux, Pascal Delmas, and Christine Allen. Predicting the solubility of the anti-cancer agent docetaxel in small molecule excipients using computational methods. *Pharmaceutical Research*, 25(1):147–157, 2008.
- [95] Sungwon Kim, Yunzhou Shi, Ji Young Kim, Kinam Park, and Ji-Xin Cheng. Overcoming the barriers in micellar drug delivery: loading efficiency, in vivo stability, and micelle–cell interaction. *Expert Opinion on Drug Delivery*, 7(1):49–62, 2010.
- [96] Sheetal S Jawalkar, Kothapalli VSN Raju, Shivaraj B Halligudi, Malladi Sairam, and Tejraj M Aminabhavi. Molecular modeling simulations to predict compatibility of poly (vinyl alcohol) and chitosan blends: a comparison with experiments. *The Journal of Physical Chemistry B*, 111(10):2431–2439, 2007.
- [97] Michael Lysaght and Thomas J Webster. *Biomaterials for artificial organs*. Elsevier, 2010.
- [98] Chang-Soo Kim, David M Saylor, Martin K McDermott, Dinesh V Patwardhan, and James A Warren. Modeling solvent evaporation during the manufacture of controlled

- drug-release coatings and the impact on release kinetics. *Journal of Biomedical Materials Research Part B: Applied Biomaterials*, 90(2):688–699, 2009.
- [99] Alanna Petroff. These countries want to ban gas and diesel cars. <http://money.cnn.com/2017/09/11/autos/countries-banning-diesel-gas-cars/index.html>, September 2017. [Online; accessed 26-Oct-2018].
- [100] Oxis Energy. <https://oxisenergy.com/>. [Online; accessed 26-Oct-2018].
- [101] J-M Tarascon and Michel Armand. Issues and challenges facing rechargeable lithium batteries. In *Materials For Sustainable Energy: a Collection of Peer-Reviewed Research and Review Articles from Nature Publishing Group*, pages 171–179. World Scientific, 2011.
- [102] Tesla. <https://www.tesla.com/models>, . [Online; accessed 21-June-2020].
- [103] Tesla. <https://www.tesla.com/modelx>, . [Online; accessed 21-June-2020].
- [104] Nissan USA. <https://www.nissanusa.com/vehicles/electric-cars/leaf/features/range-charging-battery.html>. [Online; accessed 21-June-2020].
- [105] Arumugam Manthiram, Yongzhu Fu, and Yu-Sheng Su. Challenges and prospects of lithium–sulfur batteries. *Accounts of Chemical Research*, 46(5):1125–1134, 2012.
- [106] Sylwia Walus. *Lithium/Sulfur batteries: development and understanding of the working mechanisms*. PhD thesis, Université Grenoble Alpes, 2015.
- [107] Xiulei Ji and Linda F Nazar. Advances in Li–S batteries. *Journal of Materials Chemistry*, 20(44):9821–9826, 2010.
- [108] Yuriy Mikhaylik, Igor Kovalev, Jason Xu, and Riley Schock. Rechargeable Li–S battery with specific energy 350 wh/kg and specific power 3000 w/kg. *ECS Transactions*, 13(19):53–59, 2008.

- [109] Donae Lerwill. Oxis energy is close to achieving 500wh/kg and is targeting 600wh/kg with solid state lithium sulfur technology. <https://oxisenergy.com/https-oxisenergy-com-wp-content-uploads-2020-01-500-and-600-whkg-pressor-pdf/>, January 2020. [Online; accessed 1-Mar-2020].
- [110] Donae Lerwill. Oxis energy to develop proof-of-concept advanced, lightweight lithium sulfur cells for by aerospace. <http://sustainableskies.org/oxis-energy-by-aerospace-collaborate-lithium-sulfur-cells/>, July 2019. [Online; accessed 15-Aug-2019].
- [111] OxisEnergy. Ultra light cell specification. <http://oxisenergy.com/wp-content/uploads/2016/10/OXIS-Li-S-Ultra-Light-Cell-v4.01.pdf>, October 2016. [Online; accessed 1-Mar-2020].
- [112] Peter G Bruce, Stefan A Freunberger, Laurence J Hardwick, and Jean-Marie Tarascon. Li-O₂ and Li-S batteries with high energy storage. *Nature Materials*, 11(1):19, 2012.
- [113] Arumugam Manthiram, Yongzhu Fu, Sheng-Heng Chung, Chenxi Zu, and Yu-Sheng Su. Rechargeable lithium-sulfur batteries. *Chemical Reviews*, 114(23):11751–11787, 2014.
- [114] Yuriy V Mikhaylik and James R Akridge. Polysulfide shuttle study in the Li/S battery system. *Journal of The Electrochemical Society*, 151(11):A1969–A1976, 2004.
- [115] Dong Zheng, Xiao-Qing Yang, and Deyang Qu. Reaction between lithium anode and polysulfide ions in a lithium-sulfur battery. *ChemSusChem*, 9(17):2348–2350, 2016.
- [116] Gaoran Li, Min Ling, Yifan Ye, Zhoupeng Li, Jinghua Guo, Yingfang Yao, Junfa Zhu, Zhan Lin, and Shanqing Zhang. Acacia senegal-inspired bifunctional binder for longevity of lithium-sulfur batteries. *Advanced Energy Materials*, 5:1500878, 2015.

- [117] Yoon Hwa, Peter D. Frischmann, Brett A. Helms, and Elton J. Cairns. Aqueous-processable redox-active supramolecular polymer binders for advanced lithium/sulfur cells. *Chemistry of Materials*, 30:685–691, 2018.
- [118] Hongqiang Wang, Vitor Sencadas, Guoping Gao, Hong Gao, Aijun Du, Huakun Liu, and Zaiping Guo. Strong affinity of polysulfide intermediates to multi-functional binder for practical application in lithium–sulfur batteries. *Nano Energy*, 26:722–728, 2016.
- [119] Guangmin Zhou, Kai Liu, Yanchen Fan, Mengqi Yuan, Bofei Liu, Wei Liu, Feifei Shi, Yayuan Liu, Wei Chen, Jeffrey Lopez, et al. An aqueous inorganic polymer binder for high performance lithium–sulfur batteries with flame-retardant properties. *ACS Central Science*, 4(2):260–267, 2018.
- [120] Guo Ai, Yiling Dai, Yifan Ye, Wenfeng Mao, Zhihui Wang, Hui Zhao, Yulin Chen, Junfa Zhu, Yanbao Fu, Vincent Battaglia, et al. Investigation of surface effects through the application of the functional binders in lithium sulfur batteries. *Nano Energy*, 16: 28–37, 2015.
- [121] Gao Liu, Shidi Xun, Nenad Vukmirovic, Xiangyun Song, Paul Olalde-Velasco, Honghe Zheng, Vince S Battaglia, Linwang Wang, and Wanli Yang. Polymers with tailored electronic structure for high capacity lithium battery electrodes. *Advanced Materials*, 23(40):4679–4683, 2011.
- [122] Mingyan Wu, Xingcheng Xiao, Nenad Vukmirovic, Shidi Xun, Prodip K Das, Xiangyun Song, Paul Olalde-Velasco, Dongdong Wang, Adam Z Weber, Lin-Wang Wang, et al. Toward an ideal polymer binder design for high-capacity battery anodes. *Journal of the American Chemical Society*, 135(32):12048–12056, 2013.
- [123] Jing Sun, Yaqin Huang, Weikun Wang, Zhongbao Yu, Anbang Wang, and Keguo Yuan. Application of gelatin as a binder for the sulfur cathode in lithium–sulfur batteries. *Electrochimica Acta*, 53(24):7084–7088, 2008.

- [124] Zhi Wei Seh, Qianfan Zhang, Weiyang Li, Guangyuan Zheng, Hongbin Yao, and Yi Cui. Stable cycling of lithium sulfide cathodes through strong affinity with a bifunctional binder. *Chemical Science*, 4(9):3673–3677, 2013.
- [125] Hao Chen, Min Ling, Luke Hencz, Han Yeu Ling, Gaoran Li, Zhan Lin, Gao Liu, and Shanqing Zhang. Exploring chemical, mechanical, and electrical functionalities of binders for advanced energy-storage devices. *Chemical Reviews*, 118(18):8936–8982, 2018.
- [126] Kyusung Park, Joon Hee Cho, Ji-Hoon Jang, Byeong-Chul Yu, T Andreea, Kevin M Miller, Christopher J Ellison, and John B Goodenough. Trapping lithium polysulfides of a Li–S battery by forming lithium bonds in a polymer matrix. *Energy & Environmental Science*, 8(8):2389–2395, 2015.
- [127] Weiyang Li, Qianfan Zhang, Guangyuan Zheng, Zhi Wei Seh, Hongbin Yao, and Yi Cui. Understanding the role of different conductive polymers in improving the nanostructured sulfur cathode performance. *Nano Letters*, 13(11):5534–5540, 2013.
- [128] Lifan Xiao, Yuliang Cao, Jie Xiao, Birgit Schwenzer, Mark H Engelhard, Laxmikant V Saraf, Zimin Nie, Gregory J Exarhos, and Jun Liu. A soft approach to encapsulate sulfur: polyaniline nanotubes for lithium–sulfur batteries with long cycle life. *Advanced Materials*, 24(9):1176–1181, 2012.
- [129] San Moon, Jung-Keun Yoo, Young Hwa Jung, Joo-Hyung Kim, Yeon Sik Jung, and Do Kyung Kim. Effective suppression of polysulfide dissolution by uniformly transfer-printed conducting polymer on sulfur cathode for Li–S batteries. *Journal of The Electrochemical Society*, 164(1):A6417–A6421, 2017.
- [130] Guiyin Xu, Qing-bo Yan, Akihiro Kushima, Xiaogang Zhang, Jin Pan, and Ju Li. Conductive graphene oxide-polyacrylic acid (GOPAA) binder for lithium–sulfur battery. *Nano Energy*, 31:568–574, 2017.

- [131] Zhuan Ji, Bo Han, Qiyang Li, Chenggang Zhou, Qiang Gao, Kaisheng Xia, and Jinping Wu. Anchoring lithium polysulfides via affinitive interactions: electrostatic attraction, hydrogen bonding, or in parallel? *The Journal of Physical Chemistry C*, 119(35):20495–20502, 2015.
- [132] Yuanfu Deng, Hui Xu, Zhaowen Bai, Baoling Huang, Jingyang Su, and Guohua Chen. Durable polydopamine-coated porous sulfur core-shell cathode for high performance lithium–sulfur batteries. *Journal of Power Sources*, 300:386–394, 2015.
- [133] Qianfan Zhang, Yapeng Wang, Zhi Wei Seh, Zhongheng Fu, Ruifeng Zhang, and Yi Cui. Understanding the anchoring effect of two-dimensional layered materials for lithium–sulfur batteries. *Nano Letters*, 15(6):3780–3786, 2015.
- [134] Peter E Blöchl. Projector augmented-wave method. *Physical Review B*, 50(24):17953–17979, 1994.
- [135] John P Perdew, Kieron Burke, and Matthias Ernzerhof. Generalized gradient approximation made simple. *Physical Review Letters*, 77(18):3865–3868, 1996.
- [136] G. Kresse and J. Hafner. *Ab initio* molecular dynamics for open-shell transition metals. *Physical Review B*, 48(17):13115–13118, 1993.
- [137] G. Kresse and J. Furthmüller. Efficient iterative schemes for *ab initio* total-energy calculations using a plane–wave basis set. *Physical Review B*, 54(16):11169–11186, 1996.
- [138] Zhi Wei Seh, Jung Ho Yu, Weiyang Li, Po-Chun Hsu, Haotian Wang, Yongming Sun, Hongbin Yao, Qianfan Zhang, and Yi Cui. Two-dimensional layered transition metal disulphides for effective encapsulation of high-capacity lithium sulphide cathodes. *Nature Communications*, 5:5017, 2014.

- [139] Jiří Klimeš, David R Bowler, and Angelos Michaelides. Chemical accuracy for the van der Waals density functional. *Journal of Physics: Condensed Matter*, 22(2):022201, 2009.
- [140] Kyuho Lee, Éamonn D Murray, Lingzhu Kong, Bengt I Lundqvist, and David C Langreth. Higher-accuracy van der Waals density functional. *Physical Review B*, 82(8):081101, 2010.
- [141] M Hagen, P Schiffels, M Hammer, S Dörfler, J Tübke, MJ Hoffmann, H Althues, and S Kaskel. In-situ raman investigation of polysulfide formation in Li-S cells. *Journal of The Electrochemical Society*, 160(8):A1205–A1214, 2013.
- [142] Bernard Delley. From molecules to solids with the DMol³ approach. *Journal of Chemical Physics*, 113(18):7756–7764, 2000.
- [143] Li-Chang Yin, Ji Liang, Guang-Min Zhou, Feng Li, Riichiro Saito, and Hui-Ming Cheng. Understanding the interactions between lithium polysulfides and N-doped graphene using density functional theory calculations. *Nano Energy*, 25:203–210, 2016.
- [144] Jiří Klimeš, David R Bowler, and Angelos Michaelides. Van der Waals density functionals applied to solids. *Physical Review B*, 83(19):195131, 2011.
- [145] Jiří Klimeš, David R Bowler, and Angelos Michaelides. Chemical accuracy for the van der Waals density functional. *Journal of Physics: Condensed Matter*, 22(2):022201, 2010.
- [146] Ting-Zheng Hou, Wen-Tao Xu, Xiang Chen, Hong-Jie Peng, Jia-Qi Huang, and Qiang Zhang. Lithium bond chemistry in lithium-sulfur batteries. *Angewandte Chemie International Edition*, 56(28):8178–8182, 2017.
- [147] Axel D Becke. Density-functional thermochemistry. iii. the role of exact exchange. *Journal of Chemical Physics*, 98(7):5648–5652, 1993.

- [148] MJ Frisch, GW Trucks, HB Schlegel, GE Scuseria, MA Robb, JR Cheeseman, G Scalmani, V Barone, B Mennucci, GA Petersson, et al. Gaussian 09, Revision B. 01. *Gaussian Inc. Wallingford CT*, 2010.
- [149] Zhenhua Sun, Jingqi Zhang, Lichang Yin, Guangjian Hu, Ruopian Fang, Hui-Ming Cheng, and Feng Li. Conductive porous vanadium nitride/graphene composite as chemical anchor of polysulfides for lithium–sulfur batteries. *Nature Communications*, 8:14627, 2017.
- [150] Dong Zheng, Deyu Qu, Xiao-Qing Yang, Xiqian Yu, Hung-Sui Lee, and Deyang Qu. Quantitative and qualitative determination of polysulfide species in the electrolyte of a lithium–sulfur battery using HPLC ESI/MS with one-step derivatization. *Advanced Energy Materials*, 5(16):1401888, 2015.
- [151] Q. Wang, J. Zheng, E. Walter, H. Pan, D. Lv, P. Zuo, H. Chen, Z. D. Deng, B. Y. Liaw, X. Yu, X. Yang, J.-G. Zhang, J. Liu, and J Xiao. Direct observation of sulfur radicals as reaction media in lithium sulfur batteries. *Journal of The Electrochemical Society*, 162(3):A474–A478, 2015.
- [152] T. A. Pascal, C. D. Pemmaraju, and D Prendergast. X-ray spectroscopy as a probe for lithium polysulfide radicals. *Physical Chemistry Chemical Physics*, 17(12):7743–7753, 2015.
- [153] K. H. Wujcik, T. A. Pascal, C. Pemmaraju, D. Devaux, W. C. Stolte, N. P. Balsara, and D Prendergast. Characterization of polysulfide radicals present in an ether-based electrolyte of a lithium–sulfur battery during initial discharge using in situ x-ray absorption spectroscopy experiments and first-principles calculations. *Advanced Energy Materials*, 5(16):1500285, 2015.
- [154] Tao Wang, Jian Zhu, Zengxi Wei, Hongguan Yang, Zhaolin Ma, Ruifang Ma, Jian

- Zhou, Yuhua Yang, Lele Peng, Huilong Fei, et al. Bacteria-derived biological carbon building robust Li–S batteries. *Nano Letters*, 19(7):4384–4390, 2019.
- [155] Yongzhu Fu and Arumugam Manthiram. Enhanced cyclability of lithium–sulfur batteries by a polymer acid-doped polypyrrole mixed ionic–electronic conductor. *Chemistry of Materials*, 24(15):3081–3087, 2012.
- [156] Baoe Li, Zhenghao Sun, Yan Zhao, and Zhumabay Bakenov. A novel hierarchically porous polypyrrole sphere modified separator for lithium–sulfur batteries. *Polymers*, 11(8):1344, 2019.
- [157] Z. Wang, Y. Chen, V. Battaglia, and G Liu. Improving the performance of lithium–sulfur batteries using conductive polymer and micrometric sulfur powder. *Journal of Materials Research*, 29(9):1027–1033, 2014.
- [158] Borui Liu, Renheng Bo, Mahdiar Taheri, I Bernardo Di, Nunzio Motta, Hongjun Chen, Takuya Tsuzuki, Guihua Yu, and Antonio Tricoli. Metal–organic frameworks/conducting polymer hydrogel integrated three-dimensional free-standing monoliths as ultrahigh loading Li–S battery electrodes. *Nano Letters*, 19(7):4391–4399, 2019.
- [159] E Cances, Benedetta Mennucci, and J Tomasi. A new integral equation formalism for the polarizable continuum model: theoretical background and applications to isotropic and anisotropic dielectrics. *Journal of Chemical Physics*, 107(8):3032–3041, 1997.
- [160] Maurizio Cossi, Giovanni Scalmani, Nadia Rega, and Vincenzo Barone. New developments in the polarizable continuum model for quantum mechanical and classical calculations on molecules in solution. *Journal of Chemical Physics*, 117(1):43–54, 2002.
- [161] Benedetta Mennucci, E Cances, and J Tomasi. Evaluation of solvent effects in isotropic and anisotropic dielectrics and in ionic solutions with a unified integral equation

- method: theoretical bases, computational implementation, and numerical applications. *Journal of Physical Chemistry B*, 101(49):10506–10517, 1997.
- [162] Nav Nidhi Rajput, Vijayakumar Murugesan, Yongwoo Shin, Kee Sung Han, Kah Chun Lau, Junzheng Chen, Jun Liu, Larry A. Curtiss, Karl T. Mueller, and Kristin A. Persson. Elucidating the solvation structure and dynamics of lithium polysulfides resulting from competitive salt and solvent interactions. *Chemistry of Materials*, 29: 3375–3379, 2017.
- [163] Stefan Grimme, Jens Antony, Stephan Ehrlich, and Helge Krieg. A consistent and accurate ab initio parametrization of density functional dispersion correction (DFT-D) for the 94 elements H-Pu. *Journal of Chemical Physics*, 132(15):154104, 2010.
- [164] Stefan Grimme, Stephan Ehrlich, and Lars Goerigk. Effect of the damping function in dispersion corrected density functional theory. *Journal of Computational Chemistry*, 32(7):1456–1465, 2011.
- [165] def2 TZVP. <https://bse.pnl.gov/bse/portal>. [Online; accessed 10-April-2019].
- [166] M. J. Frisch, G. W. Trucks, H. B. Schlegel, G. E. Scuseria, M. A. Robb, J. R. Cheeseman, G. Scalmani, V. Barone, G. A. Petersson, H. Nakatsuji, X. Li, M. Caricato, A. V. Marenich, J. Bloino, B. G. Janesko, R. Gomperts, B. Mennucci, H. P. Hratchian, J. V. Ortiz, A. F. Izmaylov, J. L. Sonnenberg, D. Williams-Young, F. Ding, F. Lipparini, F. Egidi, J. Goings, B. Peng, A. Petrone, T. Henderson, D. Ranasinghe, V. G. Zakrzewski, J. Gao, N. Rega, G. Zheng, W. Liang, M. Hada, M. Ehara, K. Toyota, R. Fukuda, J. Hasegawa, M. Ishida, T. Nakajima, Y. Honda, O. Kitao, H. Nakai, T. Vreven, K. Throssell, J. A. Montgomery, J. E. Peralta Jr., F. Ogliaro, M. J. Bearpark, J. J. Heyd, E. N. Brothers, K. N. Kudin, V. N. Staroverov, T. A. Keith, R. Kobayashi, J. Normand, K. Raghavachari, A. P. Rendell, J. C. Burant, S. S. Iyengar, J. Tomasi, M. Cossi, J. M. Millam, M. Klene, C. Adamo, R. Cammi, J. W. Ochterski,

- R. L. Martin, K. Morokuma, O. Farkas, J. B. Foresman, and D. J. Fox. *Gaussian 16, Revision B.01*. Gaussian, Inc., Wallingford, CT, 2016.
- [167] Christopher I Bayly, Piotr Cieplak, Wendy Cornell, and Peter A Kollman. A well-behaved electrostatic potential based method using charge restraints for deriving atomic charges: the resp model. *Journal of Physical Chemistry*, 97(40):10269–10280, 1993.
- [168] Tian Lu and Feiwu Chen. Multiwfn: a multifunctional wavefunction analyzer. *Journal of Computational Chemistry*, 33(5):580–592, 2012.
- [169] Willis E Moore. The use of an approximate dielectric constant to blend solvent systems. *Journal of the American Pharmaceutical Association*, 47(12):855–857, 1958.
- [170] Roy Dennington, Todd Keith, and John Millam. *GaussView 6.0*. Gaussian, Inc., Wallingford, CT, 2016.
- [171] Liang Zhang, Min Ling, Jun Feng, Liqiang Mai, Gao Liu, and Jinghua Guo. The synergetic interaction between LiNO_3 and lithium polysulfides for suppressing shuttle effect of lithium–sulfur batteries. *Energy Storage Materials*, 11:24–29, 2018.
- [172] Guo Ai, Yiling Dai, Wenfeng Mao, Hui Zhao, Yanbao Fu, Xiangyun Song, Yunfei En, Vincent S. Battaglia, Venkat Srinivasan, and Gao Liu. Biomimetic ant-nest electrode structures for high sulfur ratio lithium–sulfur batteries. *Nano Letters*, 16(9):5365–5372, 2016.
- [173] L. Martínez, R. Andrade, E. G. Birgin, and J. M. Martínez. Packmol: a package for building initial configurations for molecular dynamics simulations. *Journal of Computational Chemistry*, 30(13):2157–2164, 2009.
- [174] Bhoj Bahadur Gurung and Mahendra Nath Roy. Study of densities, viscosities and

- ultrasonic speeds of binary mixtures containing 1,2-dimethoxyethane and an alkan-1-ol at 298.15 K. *Journal of Solution Chemistry*, 35(12):1587–1606, 2006.
- [175] B. Giner, H. Artigas, M. Haro, C. Lafuente, and M. C. López. Viscosities of binary mixtures of 1, 3-dioxolane or 1, 4-dioxane with isomeric chlorobutanes. *Journal of Molecular Liquids*, 129(3):176–180, 2006.
- [176] M. J. Abraham, T. Murtola, R. Schulz, S. Páll, J. C. Smith, B. Hess, and E. Lindahl. GROMACS: high performance molecular simulations through multi-level parallelism from laptops to supercomputers. *SoftwareX*, 1:19–25, 2015.
- [177] S. Páll, M. J. Abraham, C. Kutzner, B. Hess, and E. Lindahl. Tackling exascale software challenges in molecular dynamics simulations with GROMACS. In S. Markidis and E. Laure, editors, *Solving Software Challenges for Exascale*, volume 8759, pages 3–27. Springer International Publishing: Cham, 2015.
- [178] S. Pronk, S. Páll, R. Schulz, P. Larsson, P. Bjelkmar, R. Apostolov, M. R. Shirts, J. C. Smith, P. M. Kasson, D. van der Spoel, B. Hess, and E. Lindahl. GROMACS 4.5: a high-throughput and highly parallel open source molecular simulation toolkit. *Bioinformatics*, 29:845–854, 2013.
- [179] B. Hess, C. Kutzner, D. van der Spoel, and E. Lindahl. GROMACS 4: algorithms for highly efficient, load-balanced, and scalable molecular simulation. *Journal of Chemical Theory and Computation*, 4:435–447, 2008.
- [180] D. van der Spoel, E. Lindahl, B. Hess, G. Groenhof, A. E. Mark, and H. J. C. Berendsen. GROMACS: fast, flexible and free. *Journal of Computational Chemistry*, 26: 1701–1719, 2005.
- [181] E. Lindahl, B. Hess, and D. van der Spoel. GROMACS 3.0: a package for molecular simulation and trajectory analysis. *Journal of Molecular Modeling*, 7(8):306–317, 2001.

- [182] H. J. C. Berendsen, D. van der Spoel, and R. van Drunen. GROMACS: a message-passing parallel molecular dynamics implementation. *Computer Physics Communications*, 91:43–56, 1995.
- [183] Junmei Wang, Romain M Wolf, James W Caldwell, Peter A Kollman, and David A Case. Development and testing of a general amber force field. *Journal of Computational Chemistry*, 25(9):1157–1174, 2004.
- [184] Dmitry Bedrov, Jean-Philip Piquemal, Oleg Borodin, Alexander D MacKerell Jr, Benoît Roux, and Christian Schröder. Molecular dynamics simulations of ionic liquids and electrolytes using polarizable force fields. *Chemical Reviews*, 119(13):7940–7995, 2019.
- [185] Junmei Wang, Piotr Cieplak, and Peter A. Kollman. How well does a restrained electrostatic potential (RESP) model perform in calculating conformational energies of organic and biological molecules? *Journal of Computational Chemistry*, 21(12):1049–1074, 2000.
- [186] A. W. Sousa da Silva and W. F. Vranken. Acpype - antechamber python parser interface. *BMC Research Notes*, 5:367, 2012.
- [187] acpype. <http://svn.code.sf.net/p/ccpn/code/branches/stable/ccpn/python/acpype/>. [Online; accessed 02-July-2019].
- [188] J. Wang, W. Wang, P. A. Kollman, and D. A. Case. Automatic atom type and bond type perception in molecular mechanical calculations. *Journal of Molecular Graphics and Modelling*, 25(2):247–260, 2006.
- [189] D.A. Case, I.Y. Ben-Shalom, S.R. Brozell, D.S. Cerutti, T.E. Cheatham, V.W.D. Cruzeiro III, T.A. Darden, R.E. Duke, D. Ghoreishi, M.K. Gilson, H. Gohlke, A.W. Goetz, D. Greene, R Harris, N. Homeyer, S. Izadi, A. Kovalenko, T. Kurtzman,

- T.S. Lee, S. LeGrand, P. Li, C. Lin, J. Liu, T. Luchko, R. Luo, D.J. Mermelstein, K.M. Merz, Y. Miao, G. Monard, C. Nguyen, H. Nguyen, I. Omelyan, A. Onufriev, F. Pan, R. Qi, D.R. Roe, A. Roitberg, C. Sagui, S. Schott-Verdugo, J. Shen, C.L. Simmerling, J. Smith, R. Salomon-Ferrer, J. Swails, R.C. Walker, J. Wang, H. Wei, R.M. Wolf, X. Wu, L. Xiao, D.M. York, and P.A. Kollman. *AMBER 2018*. University of California, San Francisco, 2018.
- [190] W. Humphrey, A. Dalke, and K. Schulten. VMD: visual molecular dynamics. *Journal of Molecular Graphics*, 14:33–38, 1996.
- [191] B. Hess, H. Bekker, H. J. C. Berendsen, and J. G. E. M. Fraaije. LINCS: a linear constraint solver for molecular simulations. *Journal of Computational Chemistry*, 18(12):1463–1472, 1997.
- [192] G. Bussi, D. Donadio, and M. Parrinello. Canonical sampling through velocity rescaling. *Journal of Chemical Physics*, 126:014101, 2007.
- [193] H. J. C. Berendsen, J. P. M. Postma, W. F. van Gunsteren, A. DiNola, and J. R. Haak. Molecular dynamics with coupling to an external bath. *Journal of Chemical Physics*, 81(8):3684–3690, 1984.
- [194] M. Parrinello and A. Rahman. Polymorphic transitions in single crystals: a new molecular dynamics method. *Journal of Applied Physics*, 52(12):7182, 1981.
- [195] U. Essmann, L. Perera, M. L. Berkowitz, T. Darden, H. Lee, and L. G. Pedersen. A smooth particle mesh Ewald method. *Journal of Chemical Physics*, 103:8577–8592, 1995.
- [196] Carl Caleman, Paul J van Maaren, Minyan Hong, Jochen S Hub, Luciano T Costa, and David van der Spoel. Force field benchmark of organic liquids: density, enthalpy of vaporization, heat capacities, surface tension, isothermal compressibility, volumet-

- ric expansion coefficient, and dielectric constant. *Journal of Chemical Theory and Computation*, 8(1):61–74, 2012.
- [197] Shuang-fei Zhu, Qiang Gan, and Changgen Feng. Multimolecular complexes of cl-20 with nitropyrazole derivatives: geometric, electronic structure, and stability. *ACS Omega*, 4(8):13408–13417, 2019.
- [198] Tao Chen, Qin Zhang, Zhi Li, and Fangrong Hu. Intermolecular weak interactions of crystalline purine and uric acid investigated by terahertz spectroscopy and theoretical calculation. *Journal of Luminescence*, page 117198, 2020.

YIHAN XU

Place of Birth: China

EDUCATION

2014-2020: Ph.D., Materials Science and Engineering, UW-Milwaukee, Milwaukee, Wisconsin, USA

2011-2014: M.S., (honor), Polymer Materials Engineering, Shandong University, Jinan, Shandong, China

2007-2011: B.S., (honor), Polymer Materials Engineering, Harbin University of Science and Technology, Harbin, Heilongjiang, China

RESEARCH EXPERIENCE

- Molecular dynamics study on polymer binders for inhibiting the shuttle effect of lithium-sulfur (Li-S) batteries
- Finite element analysis on the kinetic process of planar ZEBRA (Na-NiCl₂) batteries
- Finite element analysis on the thermo-mechanical stability of planar sodium-sulfur batteries
- Molecular dynamics research on biodegradable PLGA polymers for controlled delivery
- pH-sensitive hydrogels for controlled delivery
- Effect of ionic concentration in external solution on drug release from polyelectrolyte hydrogels
- Neutral hydrogel for controlled delivery
- Effects of blend methods on MgO/LDPE nanocomposites

SOFTWARE COMPETENCIES

GROMACS: Molecular dynamics simulation

Gaussian: Quantum chemistry computation

Materials Studio: Molecular dynamics simulation

COMSOL Multiphysics: Finite element simulation; Mathematical modeling

ABAQUS CAE: Finite element simulation for thermo-mechanical properties

WORK EXPERIENCE

Jan 2019-current: TA Grader, Sheldon B. Lubar School of Business, UW-Milwaukee

May 2015-Aug 2018: Research Assistant, Department of Materials Engineering, UW-Milwaukee

Sep 2014-May 2015: Teaching Assistant, Department of Materials Engineering, UW-Milwaukee

CONFERENCES

Yihan Xu, Keeyoung Jung, Yoon-Cheol Park, Chang-Soo Kim. Computational Assessment of the Thermo-mechanical Stress Concentration in Contemporary Planar-type NaS Batteries, 2016 MRS Fall meeting, Boston, MA

- Yihan Xu, Keeyoung Jung, Chang-Soo Kim.** Mesoscopic Modeling of Structural Changes and Na-ion Diffusion in Planar Na-NiCl₂ Batteries, 2016 MRS Fall meeting, Boston, MA
- Chang-Soo Kim, Yihan Xu, Guosheng Li, Yoon-Cheol Park, Keeyoung Jung.** Modeling the Thermodynamics and Kinetic Effects on the Electrochemical Performance of Na-NiCl₂ Batteries. ECS 2016 meeting, Honolulu, HI
- Yabo Liu, Yihan Xu, Pang Zhu, Yuxi Jia.** Effects of water/polymer friction coefficient and polymer moduli on drug release from polyelectrolyte hydrogel carriers. The Third Symposium on Innovative Polymers for Controlled Delivery, Suzhou, China (Sep 2014)
- Yihan Xu, Yanyan Zhang, Yuxi Jia, Lijia An.** Finite element simulation of slow release of drugs using hydrogels as carriers with various drug concentration distributions. The Second Symposium on Innovative Polymers for Controlled Delivery, Suzhou, China (Sep 2012)
- Yanyan Zhang, Yuxi Jia, Yihan Xu, Lijia An.** Numerical simulation of enzyme-controlled drug release using hydrogels as carriers. The Second Symposium on Innovative Polymers for Controlled Delivery, Suzhou, China (Sep 2012)

PUBLICATIONS

- 1 **Yihan Xu, Dong Zheng, Weixiao Ji, Nidal Abu-Zahra, Deyang Qu.** A molecular dynamics study of the binding effectiveness between undoped conjugated polymer binders and tetra-sulfides in Li-S batteries. Submitted.
- 2 **Huan Yang, Jiyun Park, Chang-Soo Kim, Yihan Xu, Huiling Zhu, Yongxin Qi, Longwei Yin, Hui Li, Ning Lun, Yujun Bai.** Boosted electrochemical performance of Li₂ZnTi₃O₈ enabled by ion-conductive Li₂ZrO₃ concomitant with superficial Zr-doping. *Journal of Power Sources*, 379 (2018) 270-277.
- 3 **Huan Yang, Jiyun Park, Chang-Soo Kim, Yihan Xu, Huiling Zhu, Yongxin Qi, Longwei Yin, Hui Li, Ning Lun, Yujun Bai.** Uniform surface modification of Li₂ZnTi₃O₈ by liquated Na₂MoO₄ to boost the electrochemical performance. *ACS Applied Materials & Interfaces*, 9 (2017) 43603-43613.
- 4 **Yihan Xu, Keeyoung Jung, Yoon-Cheol Park, Chang-Soo Kim.** Selection of container materials for modern planar sodium sulfur (NaS) energy storage cells towards higher thermo-mechanical stability. *Journal of Energy Storage*, 12 (2017) 215-225.
- 5 **Yihan Xu, Chang-Soo Kim, David M. Saylor, Donghun Koo.** Polymer degradation and drug delivery in PLGA-based drug-polymer applications: A review of experiments and theories. *Journal of Biomedical Materials Research Part B: Applied Biomaterials*, 105B (2017) 1692-1716.
- 6 **Yihan Xu, Donghun Koo, Emily A. Gerstein, Chang-Soo Kim.** Multi-scale modeling of polymer-drug interactions and their impact on the structural evolutions in PLGA-tetracycline films. *Polymer*, 84 (2016) 121-131.
- 7 **Yabo Liu, Yihan Xu, Yaru Zhao, Yuxi Jia.** Effect of ionic concentration on drug release from polyelectrolyte hydrogel carriers analyzed via triphasic mechanism model. *Chemical Research in Chinese Universities*, 32 (2016) 302-310.

- 8 Yanyu Ding, Yuxi Jia, Shuhua Dong, **Yihan Xu**. Non-isothermal simulation of resin transfer molding process with edge effect. *Polymers & Polymer Composites*, 22 (2014) 355-360.
- 9 **Yihan Xu**, Yuxi Jia, Zhao Wang, Zhaojing Wang. Mathematical modeling and finite element simulation of slow release of drugs using hydrogels as carriers with various drug concentration distributions. *Journal of Pharmaceutical Sciences*, 102 (2013) 1532-1543.
- 10 Zhao Wang, **Yihan Xu**, Yuxi Jia, Tongfei Shi. DSPM-Type mass transfer model and its development for charged nanofiltration membranes. *Journal of Functional Materials*, 22 (2013) 3230-3234+3238.
- 11 Zhao Wang, Yuxi Jia, **Yihan Xu**, Tongfei Shi, Lijia An. Finite element analysis on multi-field coupling of cross-flow nanofiltration of polymeric membrane. *Acta Chimica Sinica*. 11 (2013) 1511-1515.

AWARDS

- Distinguished Dissertation Fellowship, UW-Milwaukee (2019)
- Distinguished Graduate Student Fellowship, UW-Milwaukee (2018)
- Honorable Mention in Student Research Poster Competition, UW-Milwaukee (2017)
- Chancellor's Award/Dean's Fellowship, UW-Milwaukee
- National Scholarship for Distinguished Graduate Student, China
- Outstanding Student Leader and Merit Student, Harbin University of Science and Technology
- Second Prize in China Undergraduate Mathematical Contest in Modeling
- First/Second Prize Scholarship (five times), Harbin University of Science and Technology